# Best Practice: RANS Turbulence Modeling in Ansys CFD

*Version 1.0*

F.R. Menter / R. Sechner,  Ansys Germany GmbH
A. Matyushenko, NTS, St. Petersburg, Russia
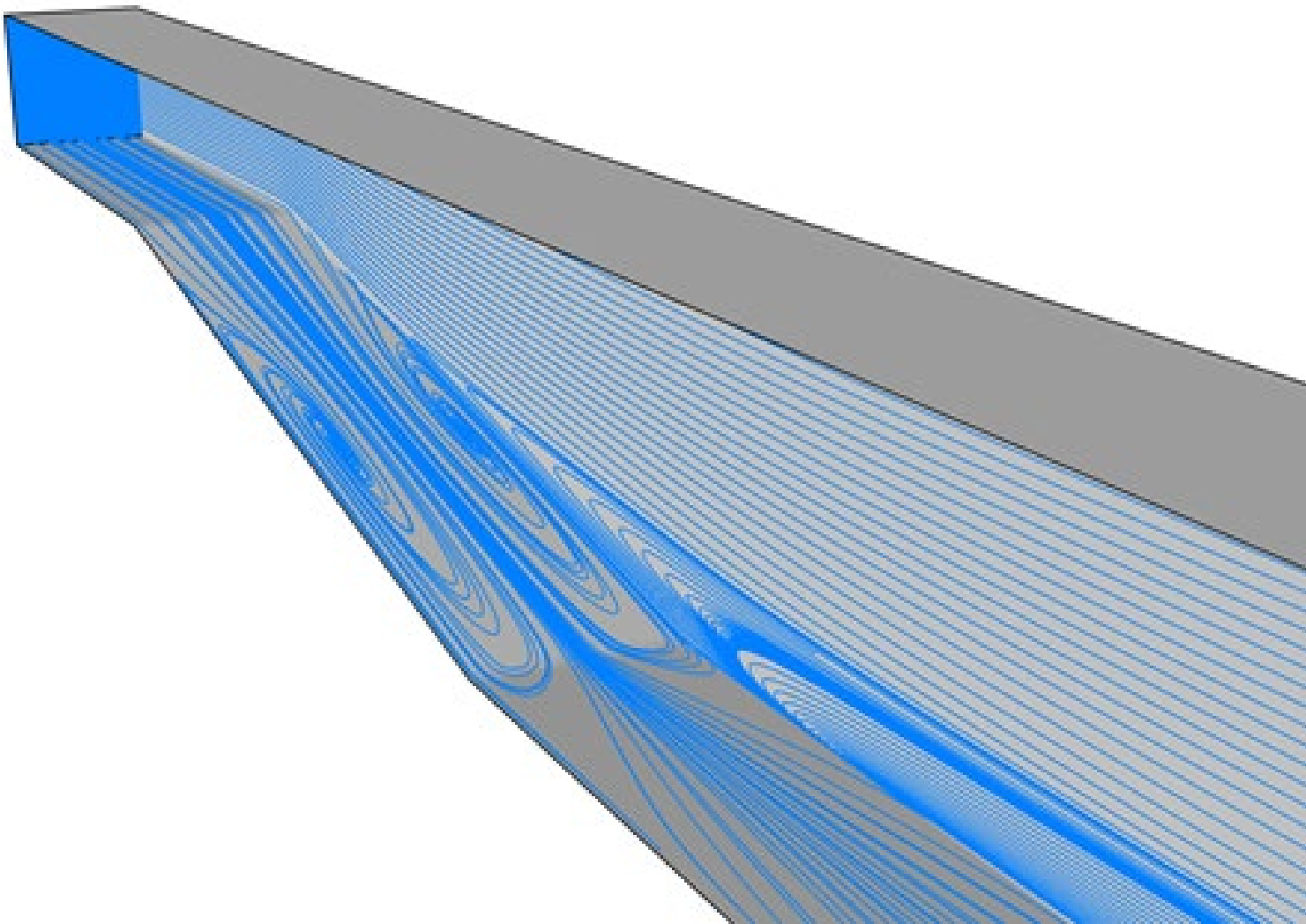
# Table of Contents

# 1. Introduction

Turbulence modeling is one of the main sources of uncertainty in CFD simulations of technical flows. This is not surprising, as turbulence is the most complex phenomenon in classical physics. Turbulent flows pose a multi-scale problem, where the dimension of the technical device is often of the order of meters (or even $10^2$ meters in case of airplanes and ships), whereas the smallest turbulence vortices are of the order of $10^{-5}$-$10^{-6}$ meters for high Reynolds number flows. Direct Numerical Simulation (DNS) of turbulence is therefore restricted to very small flow domains and low Reynolds numbers. Even the reduction in scales through Large Eddy Simulation (LES), does not lead to acceptable turn-around times for most technical flow simulations, especially in cases where wall boundary layers are important, as is most often the case (see Ansys "*Best Practice: Scale Resolving Simulations in Ansys CFD*" [1]).

A practical solution to this dilemma is offered through the concept of the Reynolds-Averaged Navier-Stokes (RANS) equations. Instead of resolving the turbulence structures in time and space and then averaging the solution to obtain the desired engineering mean flow quantities, one first averages the equations and solves directly for the time-mean (or ensemble mean) variables. While this is much more economical, it eliminates the turbulence-related physics from the equations. Turbulence models are then required to feed back that information to allow physically correct simulations. When using RANS turbulence models, one should not forget that these models are tasked to bridge many orders of magnitude in computing power relative to DNS. From this perspective, it is not surprising that RANS computations are prone to modeling errors of significant size. Unfortunately, the RANS-related uncertainty cannot be quantified reliably, as there are not only quantitative errors, but there is also the potential for qualitative failure, when predicting incorrect flow topologies. Still, properly selected RANS models work very well for many technical applications, and it is therefore essential to understand the strength and weaknesses of different models to achieve optimal solution accuracy.

The current document is not intended as a textbook on turbulence modeling. The reader is referred to the available textbooks [2]–[7], the ERCOFTAC best Practice Guidelines [8], as well as the Ansys Fluent® and the Ansys CFX® Theory and User documentation for deeper studies and for more details. The goal here is to guide the user through the process of optimal RANS model selection within the Ansys CFD codes, especially Ansys Fluent® and Ansys CFX®. Nevertheless, some of the equations required for the discussion are provided in Appendix A (Section 9) so that the reader does not have to continuously revert to the Ansys Manuals. Another document of relevance is: Ansys "*Best Practice: Generalized k-ω Two-Equation Model in Ansys*" [9]) which describes how to best use the GEKO turbulence model, recently developed at Ansys [10].

# 2. General Considerations

For CFD users, it is important to understand that turbulence modeling is an advancing technology and that Best Practice advice given some years ago might not be the Best Practice advice for today. When reading the current document, one will find that there is a consolidation in one of the most important subjects in RANS modeling – namely the choice of scale-equation. While in Ansys CFX®, there has historically been a strong emphasis on the $\omega$-equation, this is not the case in the Ansys Fluent® community, which still has a significant use of $k$-$\varepsilon$ models. To simplify turbulence model selection on the user side, as well as turbulence model development on the Ansys side, it is desirable to unite most users behind a single model family. The model family of choice in Ansys CFD is based on the $\omega$-equation. This does not mean that $\varepsilon$-equation based models will be discontinued from the codes, but it does mean that the majority of Ansys turbulence modeling efforts will focus on the $\omega$-equation family. Making such a choice requires good arguments, and one of the intentions of this document is to provide that rationale and to convince the Ansys CFD user base of its merits.

One of the historic reasons for having a multitude of turbulence models in a CFD code is the ability to select the most accurate model for a given application. When focusing on a single model family, it is necessary to address this issue and to provide the same flexibility within that given formulation. This is achieved by a concept called Generalized $k$-$\omega$ (GEKO) model [9], [10]. GEKO is a $\omega$-equation based turbulence model framework, which introduces free parameters into the equations, which can be selected and tuned by the user within given ranges, without negative impact on the basic model calibration. Instead of switching between different turbulence models to optimize accuracy, it is anticipated that the user stays within the GEKO model and optimizes its free parameters. The parameter range of the GEKO model is designed to cover a wider solution space than the one historically available through different model families. Furthermore, specific parameter choices for GEKO constitute an exact transformation of the standard $k$-$\varepsilon$ model (albeit with a superior $k$-$\omega$ wall treatment), whereas another parameter setting mimics the SST model. The need to use historic models is thereby drastically reduced. There is also a detailed Best Practice Report on how to apply the GEKO model [9].

Consistent with the above reasoning, the current document will not go through all historic model choices available in both CFD codes but will provide a guide as to the optimal selection and usage of the preferred models. This will make for a much easier read, which is already a significant benefit of the proposed strategy. However, the rationale of selecting the $\omega$-equation will be provided, and the pros-and-and-cons of different modeling concepts will be discussed.

One-equation models are also part of the current Best Practice discussion but will be treated only briefly. The reason is that these models are not suitable for a building-block approach, where different elements of physics need to be combined seamlessly to form a complete modeling framework. This does not mean that the use of such models cannot be suitable in the specific application area for which they have been developed, but they do not form the main track of turbulence models in Ansys CFD codes.

# 3. Best Practice RANS

## 3.1. Managing Uncertainty

If confronted with a new application, it is prudent to ensure that the turbulence model intended to be used is validated for this type of flows – or at least for the underlying flow features observed. Ideally, one would start with a validation study of a similar case for which experimental data are available and optimize the CFD set-up:

- Geometry
  - Represent geometry as closely as possible – small simplifications in geometry can sometimes have large effects on the solution.
  - Avoid overly tight domains – try to place inlets in regions of well-defined flow and avoid outlets in regions of strong non-equilibrium flow dynamics, especially separation/backflow zones.
- Conditions
  - Select correct physical properties for density, viscosity, …
  - Ensure correct representation of flow physics (rotating systems, porous media, …).
- Optimal grid (see 4.9)
  - Select an optimal grid topology for given flows.
  - Ensure fine resolution of wall boundary layers (see section 4.9.3).
  - Perform simulations on successively refined grids until the solution no longer changes.
- Boundary conditions
  - Match experimental/application boundary conditions closely.

- o Avoid inflow at outlets. Often the outlet flow can be accelerated through contraction of the domain in this region to avoid backflow.
- Numerics
  - o Decide on steady versus unsteady settings (3.2).
  - o Use 2nd order numerics if possible, also for the turbulence equations.
  - o Do not use small under-relaxation factors (URF). Small values can slow down convergence. The selection of optimal URF is a balance between convergence speed and robustness. Default values tend to be on the conservative side towards robustness.
- Turbulence model
  - o Compare different models or modify GEKO coefficients and establish if the flow is sensitive to model changes.
  - o Select models/coefficients which are best calibrated for the given application – or which matches best the validation case at hand.
  - o Optimize GEKO coefficients if indicated by experimental data.
  - o Decide if additional terms need to be activated
    - ▪ Curvature Correction.
    - ▪ Corner Correction.
    - ▪ Rough walls.
    - ▪ Buoyancy.
    - ▪ …
- Run case in automated/scripted way to avoid user errors during set-up and post-processing.
- Test solution sensitivity to any arbitrary assumptions made above by variation of such parameters.

The process outlined cannot be followed in all industrial CFD projects. However, it is helpful to recall what an optimal process would look like and be aware of any shortcuts taken. Experience shows that many CFD errors result from non-optimal set-ups and meshes, not from deficiencies of the turbulence model. The most common source of error being under-resolved meshes or non-converged solutions.

## 3.2. **Steady versus Unsteady Convergence**

The first question to consider before starting a RANS simulation is if the flow is steady or unsteady. As all turbulent flows are inherently unsteady in a physical sense, the question more precisely is if the flow is steady in the framework of RANS modeling. This might be one of the most difficult questions to answer a priori. In addition, the answer to this question can depend on the RANS model selected. RANS models which predict large zones of flow separation will be more likely to develop unsteady solutions than models which predict small or no separation zones. Often the models which predict larger separation zones are closer to the experimental data.

For cases where unsteadiness is imposed by the set-up, like flows with moving geometries, or unsteady boundary conditions, the situation is clear. However, there are also many flow scenarios, where the set-up is 'steady', but the flow still exhibits unsteady characteristics:

- Vortex shedding behind bluff bodies.
- Meandering/precessing vortex (e.g., combustion chamber).
- Rotating stall in axial turbomachines.
- …

If a steady state solution is expected, the usual strategy is to set numerics to 'steady conditions' and run the case. If residuals converge 'deeply' a steady solution is achieved. Unfortunately, the question 'how deep is enough' cannot easily be answered. While in some cases, three orders of magnitude are sufficient, other cases might require 4-6 orders. It is therefore recommended to plot

quantities which are sensitive to solution convergence at monitor points. One can also display distributions (e.g., xy-plots, contour plots) of quantities during the simulation. A case in point would be to display the wall shear-stress to judge if the solution has settled down. This is particularly important in cases where a transition model is employed as laminar-turbulent fronts tend to settle down slowly.

Unfortunately, in many complex applications, 'deep' convergence cannot be achieved, as there will invariably be small regions, where the solution might not fully settle down, partly due to physical and partly due to numerical reasons or mesh quality.

To judge the steadiness of the simulation in such scenarios, it is again recommended to set monitor points and plot them during the solution. This can be global parameters, like lift or drag forces, pressure drop between inlet and outlet, mass flow etc. and/or local quantities like primary solution variables (u,p,T…) at specific locations. These locations should be placed in regions of high flow complexity and the highest likelihood of local convergence problems. In cases where either the residuals, or the monitor points do not settle down to an acceptable level, it is recommended to switch to unsteady mode and continue the simulation. There are cases, where switching to unsteady mode helps to converge to steady state. If this is not the case, users must decide if the unsteadiness is of relevance, or just a small local disturbance without impact on the simulation outcome. If the unsteadiness is important, then time-mean values can only be obtained by running the simulation unsteady and averaging during run-time. It can also help to create animations to understand the cause and nature of unsteady behavior.

In a worst-case scenario, a steady state set-up can force the solution into an incorrect flow topology from which it cannot 'escape'. This is accompanied by non-convergence of the residuals which is not easy to distinguish from non-convergence due to small local oscillations. Such situations are more likely if small under-relaxation coefficients are used, as they tend to 'freeze' non-physical solutions. In such cases, switching to unsteady settings can overcome the problem and will typically lead to a strong change in the flow characteristics (as indicated by local monitor points and global forces).

## 3.3. Turbulence Model Selection

For most industrial applications, eddy-viscosity models provide the optimal balance between accuracy and robustness. Reynolds Stress Models (RSM) are not recommended for general use, as they often result in robustness problems without a reliable increase in accuracy. The additional physical effects accounted for in RSM can in most cases also be added to eddy-viscosity models, through Curvature Correction, Corner Correction and Buoyancy extensions and finally the use of Explicit Reynolds Stress Models (EARSM).

### 3.3.1. Spalart-Allmaras (SA) One Equation Model

The one-equation model of Spalart-Allmaras [11] is widely used for external aerodynamical applications in the aeronautical industry and is well suited for such applications. It provides an improved performance relative to $k$-$\varepsilon$ models for flows with adverse pressure gradients and separation. Overall, the accuracy to predict separation is lower than for optimal two-equation models like SST and GEKO. On the other hand, the model requires the solution of only one transport equation instead of two. The SA model is not recommended for general use, as it is not well calibrated for free shear flows. It does predict accurate spreading rates for mixing layers but fails for plane and round jet flows, which are strongly dissipated (overly large spreading rate) by the model. In addition, the model does not predict decay of freestream turbulence which is of importance for some types of laminar-turbulent transition predictions.

The SA model in Ansys Fluent® is also not extended to include:
- Laminar-turbulent transition
- Buoyancy
- Stress-Blended Eddy Simulation (SBES)

### 3.3.2. Two-Equation Models

Two-equation models are the main model family for industrial flow simulations. They form the foundation of a building block system which can include all elements of RANS modeling.

Within the two-equation model family, the $k$-$\omega$ based models are recommended. They offer a superior wall treatment compared with $k$-$\varepsilon$ based models and are therefore much more flexible and accurate, especially for non-equilibrium flows. This can be seen in Figure 1 for the Vogel and Eaton backward facing step [12]. This flow provides experimental data for the wall shear stress coefficient, $C_f$, and the heat transfer coefficient, $St$, on the wall downstream of the step. The mesh for this study had a fine near wall resolution of $y^+ < 1$.

Figure 1 shows a model comparison for this flow. All model variants shown are based on the same standard $k$-$\varepsilon$ model. The $k$-$\varepsilon$ ML model is a representative of a $k$-$\varepsilon$ low-Re model and inhibits the known $k$-$\varepsilon$ model deficiency of substantial over-prediction of $C_f$ and $St$ near the reattachment point [5]. The same $k$-$\varepsilon$ model combined with the 2-Layer based Enhanced Wall Treatment (EWT) shows an entirely different behavior, with a very flat distribution of the heat transfer coefficient (but a better match of $C_f$). The $k$-$\varepsilon$ model in combination with the V2F approach [13] gives an over-prediction of the separation bubble size and an overly high heat transfer coefficient distribution. The V2F model is only included for comparison and is not offered in any of the Ansys CFD codes. The $k$-$\omega$ based GEKO model with $C_{SEP} = 1.0$ (written in short as GEKO-1.0) shows the best agreement of both $C_f$ and $St$. The GEKO-1.0 model is an exact transformation of the $k$-$\varepsilon$ to a $k$-$\omega$ formulation, except for the sublayer model. Note that other $k$-$\omega$ models like BSL/SST models produce very similar results to GEKO. This example shows the superior behavior of $\omega$-equation based turbulence model for predicting wall shear-stress and heat transfer distributions compared with other approaches.
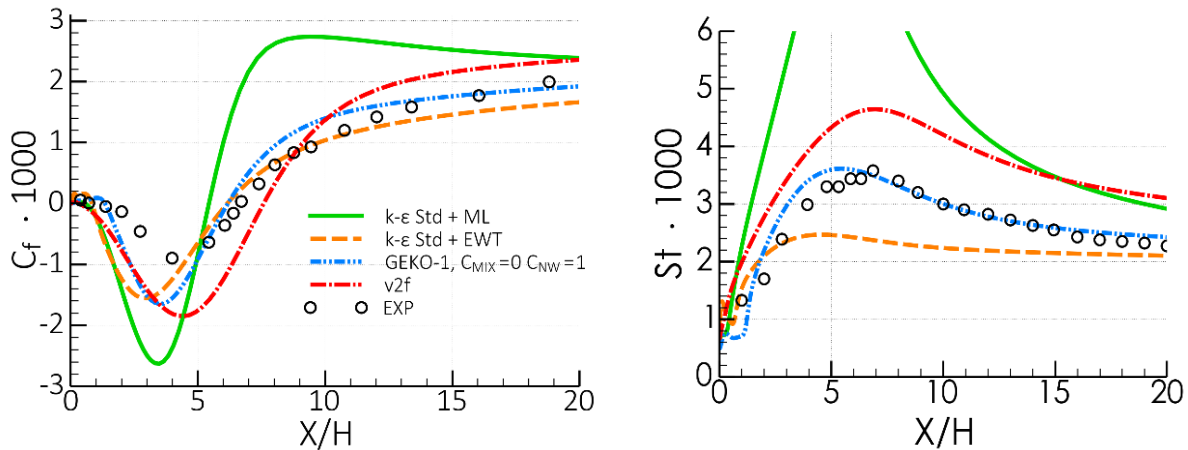


**Figure 1: Wall shear stress coefficient, $C_f$ (left) and wall heat transfer coefficient, $St$, (right) for backward-facing step flow [12].**

Turbulence models from the $k$-$\omega$ family offer additional benefits when predicting adverse pressure gradient flows and separation onset as will be shown in section 4.2. Finally, $k$-$\omega$ models are compatible with models for laminar-turbulent transition and rough wall treatments. All $k$-$\omega$ models in Ansys CFD are implemented with a $y^+$-insensitive wall treatment, avoiding the discussion concerning the optimal selection of wall formulations in $k$-$\varepsilon$ models (see 9.3). It is important to note that the grid resolution requirements between $k$-$\varepsilon$ and $k$-$\omega$ models are the same. In case of coarse grids (large $y^+$) the $y^+$-insensitive wall treatment will switch automatically to a wall function – so that there is no advantage in explicitly selecting a wall function (a choice required in some $k$-$\varepsilon$ models).

## Standard k-ε Model [14]

- Select only for cases where backwards compatibility is required (e.g., to compare with previous simulations using this model).
- Be aware that for this model no limiter (see 3.3.5) is activated by default so that excessive turbulence production can affect the simulations. Note that the lack of a limiter can lead to improved convergence (for the wrong reasons).
- It is recommended to activate the 'Production Limiter'.
- Note that the GEKO model with $C_{SEP} = 1.0$ and $C_{NW} = 1.0$ (an example is shown in section 4.2.1 for the model comparison) is an exact transformation of the standard $k$-$\varepsilon$ model – albeit with a superior wall treatment and an automatically activated realizability limiter.
- On coarse meshes, use scalable wall functions, for finer meshes use the EWT based on the 2-layer formulation.

## Realizable k-ε Model (RKE) [15]

- Select only for cases where backwards compatibility is required (e.g., to compare with previous simulations using this model).
- Be aware that the Realizability limiter of this model is only partially effective – it allows for large turbulence production in non-shear regions (see 4.7). The model can be combined with the 'Production Limiter'.
- On coarse meshes, use scalable wall functions, for finer meshes use the EWT based on the 2-layer formulation (9.3).

## RNG k-ε Model (RNGKE) [16]

- Select only for cases where backwards compatibility is required (e.g., to compare with previous simulations using this model).

## Standard k-ω Model [7]

- Do not use the standard $k$-$\omega$ model – it has a strong dependency of the solution on freestream values of $\omega$ outside of shear layers (see Figure 98). The model is available mostly for historic reasons.

## BSL/SST Model [17], [18]

- The SST model is recommended for most industrial applications. It has a high accuracy for flows with adverse pressure gradients and separation. Outside the boundary layer it reverts back to a $k$-$\varepsilon$ model setting.
- The SST model's ability to predict separation accurately is based on the SST-limiter (Equation (9.27)) which reduces the eddy-viscosity in such flows. In some scenarios, larger separation zones which might indicate unsteady behavior or be unphysical (due to either insufficient mesh resolution or complex 3d geometry-flow interactions) can lead to undesirable results or poor convergence. In such cases the $a_1$ coefficient (default $a_1 = 0.31$) can be increased to values in the range of $a_1 = 0.31\text{-}1.0$ to reduce separation. Note that the $a_1$ coefficient cannot be reduced below its default value of $a_1 = 0.31$ without violating the basic calibration of the model for boundary layers.
- Alternatively, one can switch to the BSL model, which de-activates the SST limiter entirely.
- BSL and SST models automatically activate the 'Production Limiter'.
- BSL and SST models automatically activate $y^+$-insensitive wall-treatment.

- Do not use the 'low-Reynolds number correction' with any of the $k$-$\omega$ models. It is a historic feature. It is not required to integrate the equations to the wall but can lead to pseudo-transition – meaning a non-calibrated laminar-turbulent transition effect.

*GEKO Model [10]*

- The model is intended to replace eventually all other two-equation models.
- The model can and should be used for all industrial applications.
- The model has the flexibility to allow users to tune the model against experimental data.
- The model has a realizability limiter automatically activated.
- The model activates the $y^+$-insensitive wall-treatment.
- The model can be tuned to mimic existing models like standard $k$-$\varepsilon$ or SST.
  - The SST is mimicked by default settings. Note that this does not mean an exact transformation of SST to GEKO.
  - The $k$-$\varepsilon$ model is recovered for $C_{SEP} = 1$, $C_{NW} = 1.0$. (An example is shown in section 4.2.1 for the model comparison.).
- The GEKO model has an adjoint formulation in Ansys Fluent® which can be used as a basis for machine learning.
- Note that the GEKO model is not fully published – this could lead to issues in case users want to publish their results in a scientific journal.
- There is an extensive Best Practice Guide for this model available [9].

### 3.3.3. Wallin-Johansson Explicit Algebraic Reynolds Stress Models (WJ-EARSM)

- The WJ-EARSM [19] can be used in case secondary flows are of importance (an example of the corner flows is shown is section 4.3). Note however, that similar effects can be achieved by activating the simpler Corner Flow Correction (CFC) available with GEKO (and in Ansys Fluent® with all other $k$-$\omega$ models) [20].
- Use in combination with BSL (WJ-BSL-EARSM) or better with GEKO model (a β-feature in Ansys Fluent®).
- EARSM models will not provide the same sensitivity to streamline curvature and system rotation as full RSM and additional curvature correction terms might need to be added.

### 3.3.4. Reynolds Stress Models (RSM)

- These models are prone to numerical problems on complex applications and non-optimal grids. They are therefore only recommended for applications, where they have shown superior performance over eddy-viscosity models.
- Examples of such applications are flows with strong curvature and or system rotation. Note however, that similar effects can be achieved when activating the Curvature Correction model in eddy-viscosity models.
- In case RSM are used, it is recommended to combine them with the $\omega$-equation (BSL or GEKO). The GEKO-RSM model formulation is based on the stress-omega model [7]. The model solves the Reynolds stress equations in combination with the $\omega$-equation from the GEKO model instead of the original Wilcox model.

### 3.3.5. Limiters

The eddy-viscosity assumption alters the production term, $P_k$, in the $k$-equation from a term linear in the velocity gradients to a quadratic term ($P_k = \mu_t S^2$). This can cause problems in regions with non-shear layer related strain rate, $S$, like in inviscid stagnation or in acceleration zones. When using two-equation eddy-viscosity models, limiters must therefore be employed. Limiters are not required when running the WJ-EARSM as it restricts the level of production over dissipation automatically. Examples for the use of limiters are given in section 9.2.3.

For $k$-$\varepsilon$ models, the user needs to activate a limiter. For the standard $k$-$\varepsilon$ model no limiter is active by default (representing the published version of the model) and the production limiter should be activated. For the RKE model a realizability limiter is built-in, but experience shows that it does not work effectively, due to the specifics of its formulation. Also, for this model the production limiter is recommended. Note that when writing a report/publication the activation of limiters should be clearly indicated to allow a proper interpretation and reproduction of the results.

All $\omega$-equation based models in Ansys Fluent[®] and Ansys CFX[®] have the production limiter automatically activated. The GEKO model features in addition a proper realizability limiter.

When models for laminar-turbulent transition are activated, it was found that in some cases the production limiter was not sufficient to prevent a minor build-up of turbulence in the stagnation zone of airfoils. This is usually unnoticeable in fully turbulent mode but can slightly affect the transition location. For this reason, the Kato-Launder limiter [21] is additionally activated for such flows. This limiter can affect other parts of the flow, especially flows with swirl and curvature. In case this is not acceptable, this limiter can be deactivated.

- For $k$-$\varepsilon$ models activate the production limiter by hand.
- For $k$-$\omega$ models no action required.
- For transition models – no action required unless the Kato-Launder limiter is not desired.

## 3.4. Additional Physics

The following sections describe model additions which can be used in combination with two-equation models. Particularly, Corner Correction [20] and Curvature Corrections [22], [23] are meant to eliminate some deficiencies of eddy-viscosity models relative to full Reynolds-Stress Models (RSM). Other additions, like rough walls and laminar-turbulent transition, are required for all RANS models if the effects are important for the intended application.

### 3.4.1. Laminar-turbulent transition

All models discussed in this section have been developed and calibrated for predicting laminar-turbulent transition in wall boundary layers. They are not suitable for predicting transition in free shear flows. Note that free-shear flow transition is typically not of technical relevance as it takes place at very small Reynolds numbers. As a result, most of such flows can be computed as 'fully turbulent'.

The models are also not calibrated for fully developed channel and pipe flow transition prediction. Transition phenomena in such devices can be modeled with the existing calibration if the flows are not fully developed. Under such conditions these flows still have essential boundary layer characteristics. For 'fully developed' channel and pipe flows, no freestream region exists anymore, which certainly excludes the $\gamma$-$Re_\theta$ model which requires such a region. The algebraic and one-equation intermittency models could still be viable but have not been calibrated and tested for such scenarios.

There are three recommended models for laminar-turbulent transition in Ansys Fluent[®] and Ansys CFX[®]:

- The algebraic intermittency model (Ansys Fluent[®])
- The one-equation intermittency model (Ansys Fluent[®], Ansys CFX[®])
- The two equation $\gamma$-$Re_\theta$ model (Ansys Fluent[®], Ansys CFX[®])

These models are based on the concept of 'Local-Correlation based Transition Modeling – LCTM'. They form a series of models as developed over time starting with the $\gamma$-$Re_\theta$ model [24]–[26] which was then simplified to a one-equation model and finally to an algebraic model. The models are calibrated in a similar fashion but offer differences in their predictions. Users are therefore advised to test which model best suits their test cases. Obviously, the CPU cost increases

with the number of transport equations being solved. The algebraic model might therefore serve as a good starting point.

Including the effect of transition into the CFD simulation requires finer mesh resolution (see section 4.9.4) and should therefore be employed with caution.

- Transition prediction is important for aerodynamic and turbomachinery flows, as transition can strongly affect overall performance. It is also important to include in some heat transfer cases like impinging jets, as laminar flows have a much lower heat transfer coefficient than turbulent flow.
- In case transition is important, it has strong implications on the set-up from a modeling, numerical and mesh resolution standpoint.
  o Select a suitable transition model
  o The mesh resolution requirements for predicting transition are much higher than for fully turbulent flow simulations. This is discussed in section 4.9.4.
  o Numerical settings might need to be adjusted.
  o Monitor points/charts on transition location motion should be included to check convergence. Plotting charts of wall shear stress of $C_f$ during iterations is recommended to determine visually if the transition locations are settling down.

### 3.4.2. Curvature Correction

Streamline curvature and swirl can have a significant effect on turbulence. This is illustrated in Figure 2 which shows on the left a boundary layer on a concave wall and on the right for a convex wall. In the concave case, turbulence is enhanced and for the convex case it is damped. Standard eddy-viscosity models do not account for this effect and need augmentation to sensitize them. The effect of curvature is even stronger for swirling flows, where turbulence is typically strongly suppressed (see section 4.4).
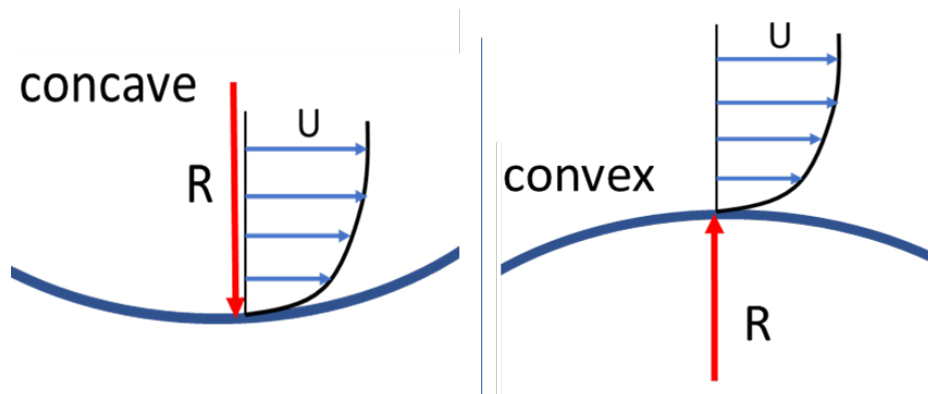


**Figure 2: Schematic of the boundary layer on the curved surfaces.**

The Curvature Correction [22] used in Ansys CFD is based on the so-called Spalart-Shur correction [23]. The details of the formulation can be found in the theory documentation and are not reported here. This correction detects changes in streamline direction due to changes in the orientation of the strain rate tensor along a streamline. This then results in a correction factor which multiplies the production terms of both the $k$- and the $\omega$-equations. For stabilizing curvature, the factor is smaller and, for de-stabilizing flows, larger than one.

The CC is most relevant not for boundary layers but for free vortex flows, where the effect of curvature results in strong damping of turbulence inside the vortex. Models without CC provisions produce much too high eddy-viscosities in such scenarios and strongly damp the vortex.

- Turbulence can be dampened or enhanced based on streamline curvature (see section 4.4). The Correction should be activated if curvature effects are strong and important. This is typically the case if the radius of curvature is of the same order or

smaller than the boundary/shear-layer thickness. Note that for most boundary layer flows this is not the case.

- This correction is most beneficial for swirling flows (tip vortex of a wing, vortex inside a hydro-cyclone). Eddy-viscosity models without this correction create excessive eddy-viscosity levels in such flows and reduce vortex strength too strongly. In addition, they enforce a solid body-like rotation, whereas a real vortex often has significant regions following inviscid laws.
- In principle, the correction does not hurt flows without or with only weak curvature but increases computational costs.

### 3.4.3. Corner Correction

Another physical effect which cannot be represented by eddy-viscosity models is the secondary flow caused by turbulence through anisotropy of the normal stresses (meaning that the normal stresses in the wall-parallel and wall-normal directions are different, driving a secondary flow). This effect appears typically in corner flows (like rectangular channels). One strategy to enable eddy-viscosity models to account for this effect is to extend them through a non-linear stress-strain relationship (see EARSM models in section 4.3). The simplest formulation is however the Quadratic Closure Relation (QCR) proposed by Spalart [20]. It consists of extending the linear part of the eddy-viscosity formulation by a quadratic term:

$$
\begin{aligned}
\tau_{ij} = -\rho \overline{u_i' u_j'} = \mu_t 2 S_{ij} - \frac{2}{3} \rho k \delta_{ij} \\
- C_{CORNER} \frac{1.2\, \mu_t}{max\left(0.3\omega, \sqrt{(S^2 + W^2)/2}\right)} \left(S_{ik} W_{kj} - W_{ik} S_{kj}\right)
\end{aligned}
\tag{3.1}
$$

with
$$
S_{i,j} = \frac{1}{2}\left(\frac{\partial U_i}{\partial x_j} + \frac{\partial U_j}{\partial x_i}\right); \quad W_{i,j} = \frac{1}{2}\left(\frac{\partial U_i}{\partial x_j} - \frac{\partial U_j}{\partial x_i}\right)
$$

The effect is important for:

- Flows parallel to corners, like those observed in wing-body junctions or rectangular channels, which develop secondary flow directed into the corner. This effect (Prandtl's secondary flows of the 2nd kind, [27]) cannot be captured by eddy-viscosity models, as the effect is driven by the anisotropy of the normal stresses of the Reynolds Stress tensor.
- Without this correction, the flow in such corners can show premature separation if encountering an adverse pressure gradient. This can have a significant effect on the overall flow and can potentially lead to incorrect flow topologies in the CFD simulation. The resulting errors can be very large, as a change in flow topology (e.g., separation induced from a corner instead of from the smooth part of the wing/blade) can affect most other flow parameters.
- Simulations will only benefit from this correction if there is a sufficiently fine grid resolution in the corner region. Hexahedral meshes are optimal for such flows, as they allow for an easy adaptation of the surface grid lines into the corner.
- This correction should not produce negative side-effects in terms of accuracy if activated in cases where it is not required. However, it can potentially affect robustness and CPU cost.

### 3.4.4. Buoyancy Correction

Flows with gradients in density in a gravity field can exhibit similar effects as flows with curvature. Flows where the force vector due to gravity and the density gradient point in the same direction are stabilized (decrease in turbulence) whereas the opposite is true for flows where the

two vectors point in opposite directions. Buoyancy terms have been developed originally for the $k$-$\varepsilon$ model. The source term in the $k$-equation reads ($g_i$ – gravity vector):

$$G_b = -g_i \frac{\mu_t}{Pr_t} \frac{1}{\rho} \frac{\partial \rho}{\partial x_i} \qquad (3.2)$$

To judge if such effects are important, this term must be set in relation to the production of turbulence kinetic energy. For shear layers one gets (with $\Delta U, \Delta\rho$ – velocity, density differences across shear layer, $\delta$ thickness of layer, $Pr_t{\sim}1$):

$$R = \left(-g_i \frac{\mu_t}{Pr_t} \frac{1}{\rho} \frac{\partial \rho}{\partial x_i}\right) \bigg/ (\mu_t S^2) \approx g \frac{\Delta\rho}{\rho} \frac{\delta}{\Delta U^2} \qquad (3.3)$$

In case where this ratio is larger than a threshold (of the order of R > 0.1) the term $G_b$ should be included. As outlined in the theory documentation, the term can additionally be included into the scale-equation ($\varepsilon/\omega$-equation). Since the benefit of doing so is not consistent, the default is to include the term only into the k-equation.

- The effect of buoyancy is similar to the effect of curvature – it can stabilize or destabilize turbulence.
- Turbulence is enhanced/damped if the density gradient and gravity vector point in opposite/same directions.

### 3.4.5. Wall Roughness Correction

Rough walls can have a significant effect on the performance of technical devices. Roughness has two essential effects. The first is that it increases wall shear stress levels (and thereby also heat transfer) and the second is that it forces laminar-turbulent transition to more upstream locations.

There are several roughness options in Ansys CFD:

- The standard method is a simple shift of the logarithmic layer based on wall roughness. In addition, the cell center of the wall cell is virtually shifted as: $y^+ \rightarrow y^+ + h_s^+/2$, where $h_s$ is the roughness height. This option is used as default in Ansys Fluent® for the Spalart-Allmaras and all $\omega$-equation based models.
- The second method is a blend of the Wilcox wall roughness model [7] and the log-layer shift, based on $y^+$. This option is the default for all $\omega$-equation based models in Ansys CFX®.
- The last option is proposed by Aupoix [28] and modifies the near wall boundary values of the turbulence quantities to achieve the desired increase in wall-shear. It can be applied to the Spalart-Allmaras model and all $\omega$-based two-equation models.

The first two options are compatible with all $y^+$ values if $y^+$ lies in the inner region (~0.1 of the boundary layer thickness).

The Aupoix formulation requires a fine near wall mesh ($y^+{\sim}1$) but can cover roughness heights which are a significant fraction of the boundary layer height.

Roughness effects on transition location can also be included into the SST $\gamma$-Re$_{\theta t}$ transition model (4-eqn model). The effect of roughness is to push the transition location upstream. While the effect of fully turbulent flow is described by the sand-grain roughness, the effect on transition is determined by the height of the roughness elements (geometric roughness), as even a single roughness element can trigger transition.

# 4. Model Evaluation

The key consideration for selecting a turbulence model is the accuracy with which the model can provide for a given flow, or a class of flows. As all turbulence models are more-or-less calibrated

for the same base-flows (e.g., flat plate boundary layer, basic free shear flows and decaying turbulence), the model accuracy outside this narrow 'calibration box' can only be determined by further validation studies. Such studies are based on 'building block' test cases, which typically add one more element of complexity to the calibration cases, like adverse pressure gradients, separation, swirl, etc. As such cases do not include the complex interactions seen in industrial flows, they do not provide the full picture, but they can give a much better idea on the suitability of a model for a certain type of flows. Such tests are also the limit to which models are tested during model development and calibration, as more complex industrial flows typically lack detailed experimental data to draw meaningful conclusions on specific model deficiencies. In the following sections, model performance will be discussed for such building-block test cases, with each section focusing on a different physical effect. It is important for CFD users to understand the differences in model performance to make an educated decision during model selection.

Since this is a Best Practice Document, only the most necessary information on the test cases and their numerical set-up is provided. All solutions have been ensured to be mesh independent and, in all cases, the boundary conditions match the experiment as closely as possible.

## 4.1. Flat Plate Flow

The setup of the zero pressure gradient flat plate boundary layer flow (see Figure 3) is based on the experiment of Wieghardt & Tillmann, [29]. The Reynolds number based on inlet velocity and the length of the flat plate is Re = $10^7$, and the wall is maintained at a constant temperature. No heat transfer measurements have been carried out. Therefore, in order to assess the capability of turbulence models to predict heat transfer to the wall, an empirical correlation is used to compute the Stanton number at the wall from the measured distribution of skin friction coefficient.
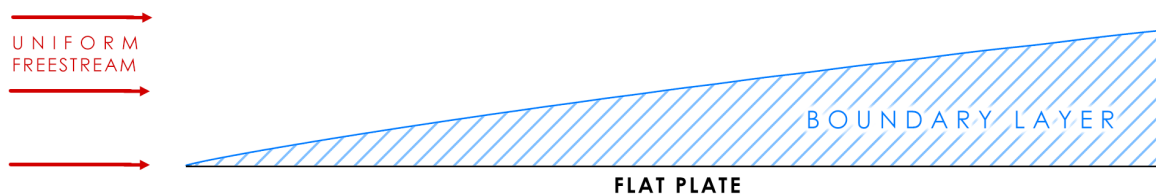


**Figure 3: Schematic of the flow over a flat plate.**

The computational domain with boundary conditions is shown in Figure 4. Constant velocity and temperature values are assigned at the inlet plane. The difference between inlet and wall temperatures is 10 K. Turbulence characteristics at the inlet are also assumed constant with values corresponding to a free-stream turbulence intensity of Tu=1%, and an eddy-viscosity ratio equal to TVR=0.2. Computational meshes (see Table 1) cover three near-wall scenarios: viscous sublayer, logarithmic region and a "buffer layer" resolution.
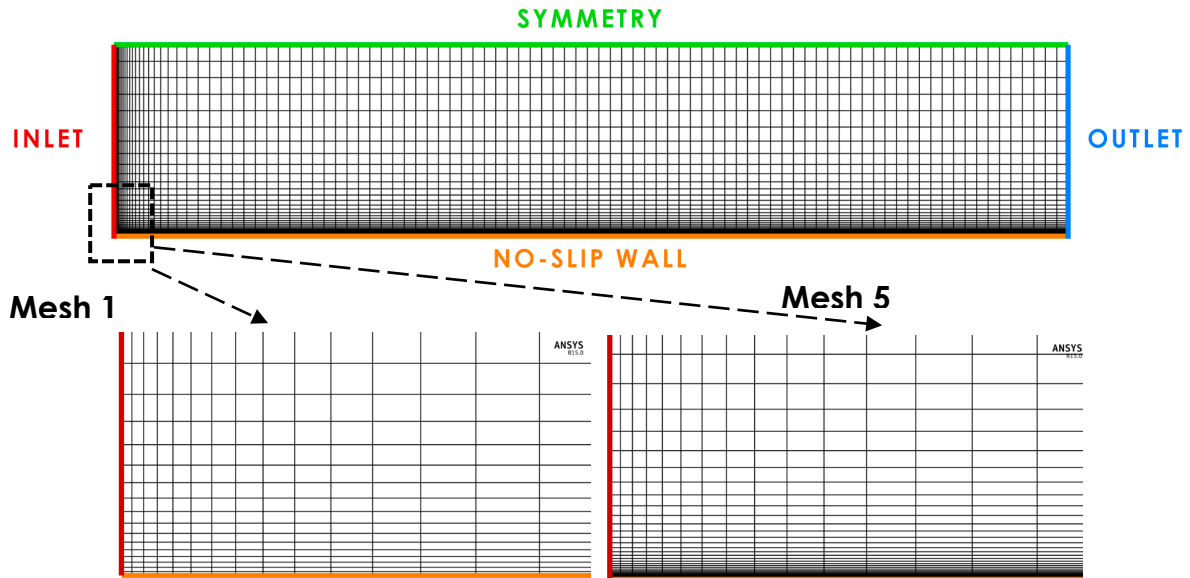
**Figure 4: Computational domain with boundary conditions and mesh for the flow over a flat plate.**

**Table 1: Parameters of the computational meshes**

|  | Mesh 1 | Mesh 2 | Mesh 3 | Mesh 4 | Mesh 5 |
|---|---|---|---|---|---|
| $y^+_{max}$ | 56.9 | 22.6 | 14.4 | 3.1 | 0.3 |
| $y^+_{mean}$ | 33.6 | 10.9 | 6.1 | 1.1 | 0.1 |
| Number of cells | 3800 | 4600 | 5000 | 6000 | 8000 |

*Model Comparison*

Figure 5 show the comparison of the results of different turbulence models (SST, GEKO, SA and RKE) on the fine mesh: Mesh-5. As expected, all the considered models perform well for the flat plate simulations, both in terms of wall shear stress, $C_f$, and wall heat transfer coefficient, St, as shown in Figure 5. Also, the velocity profiles are in good agreement with the logarithmic profile, as can be seen in Figure 6.
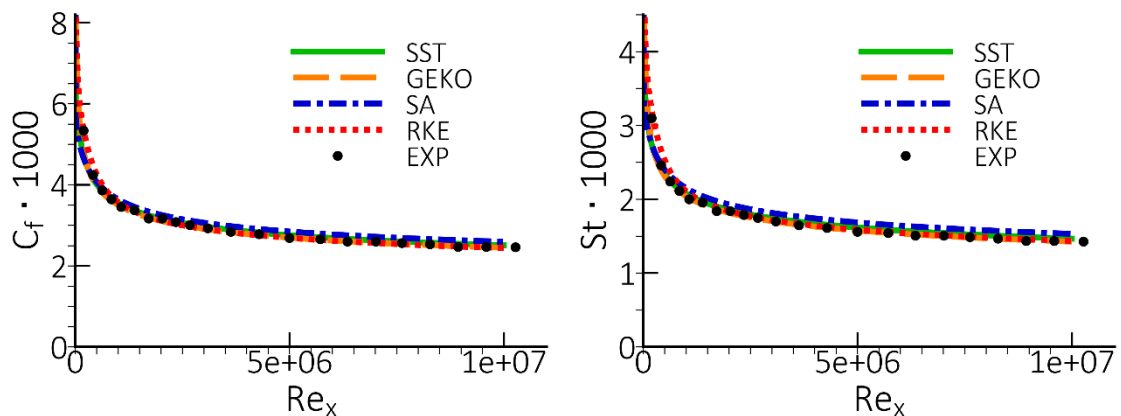


**Figure 5: Comparison of wall shear stress coefficient, $C_f$ (Left) and wall heat transfer coefficient, *St.* (Right) for flat plate boundary layer [29] and *$y^+$~1.***
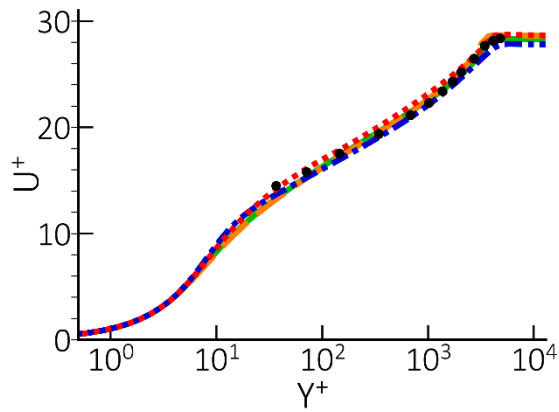
**Figure 6: Comparison of velocity profiles in wall-law for flat plate boundary layer at $Re_x = 8.7 \cdot 10^6$.**

## Non-linear effects

For the simple wall-bounded flows the non-linear effects of the EARSM or even RSM models do not affect the main flow. Figure 7 shows the prediction of the skin friction coefficient and wall-law velocity profile for the GEKO model without and with EARSM/RSM options.
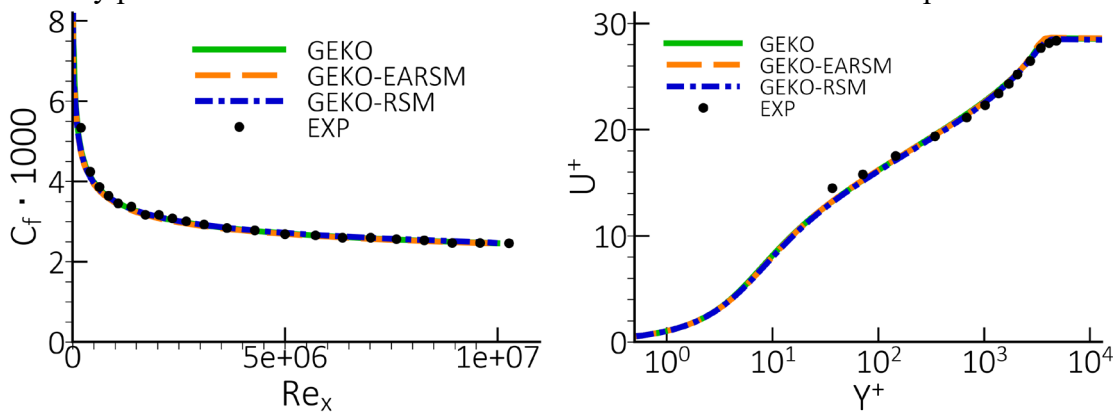


**Figure 7. Comparison of wall shear stress coefficient (Left) and velocity profile at $Re_x = 8.7 \cdot 10^6$ (Right) predicted with the GEKO model without and with EARSM/RSM options for the flat plate boundary layer [29].**

## Mesh Sensitivity

For the coarser meshes, the computational accuracy depends on the wall treatment. The use of the automatic $y^+$-insensitive wall treatment for the $k$-$\omega$ turbulence models provides virtually independence of the solution to the near wall resolution. The example of the SST model solution is shown in Figure 8. On the other hand, the accuracy of prediction of wall shear stress for high-Re $k$-$\varepsilon$ turbulence models depends on the choice of the wall treatment. The standard wall functions (SWF) designed for the high-Re $k$-$\varepsilon$ computational grids is not adequate for the low-Re fine $y^+$~1 grids which is shown in Figure 9 (Left). The use of the scalable wall functions (ScWF) improves the situation considerably (Figure 9 and Figure 10 - Right). Thus, for the remainder of the test cases the ScWF wall functions is used for the $k$-$\varepsilon$ models. For the mathematical formulation of the different wall treatments see Section 9.3.
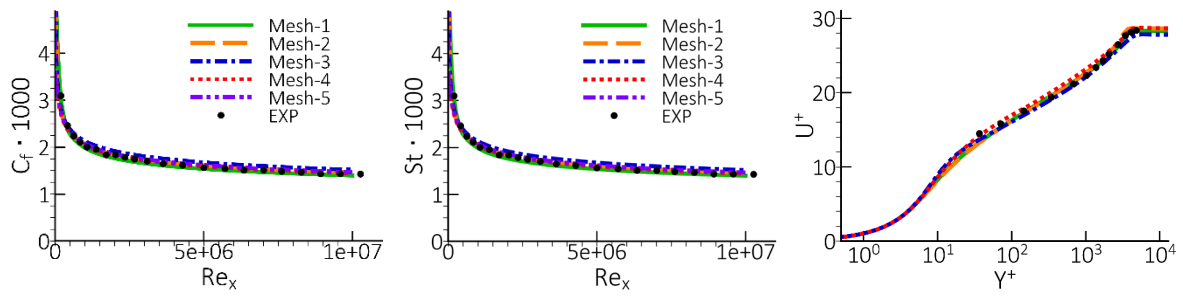
**Figure 8: Comparison of wall shear stress coefficient, $C_f$ (left), wall heat transfer coefficient, St. (middle) and log-low velocity profile at $Re_x = 8.7 \cdot 10^6$ (right) for the flat plate boundary layer using the SST model [29].**
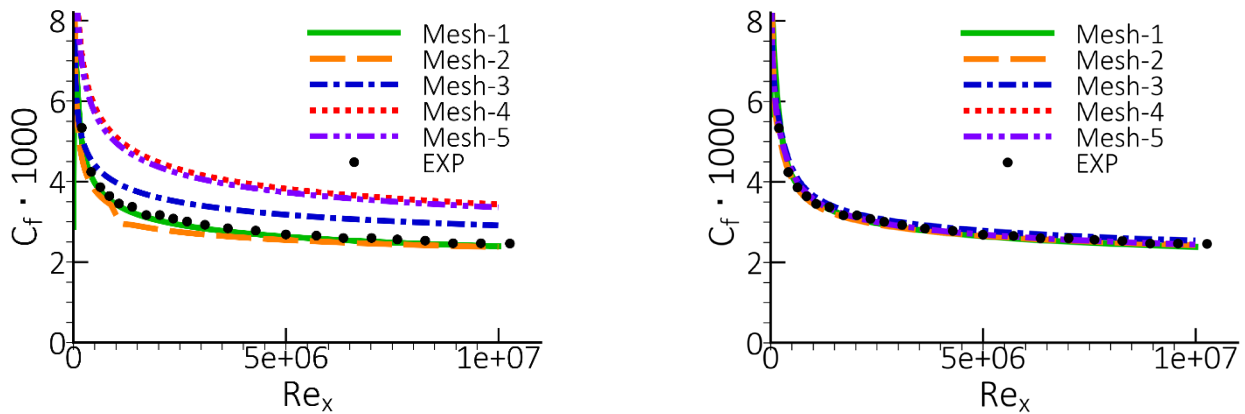


**Figure 9: Distribution of the skin friction coefficient over the flat plate computed with RKE model with SWF (left) and ScWF (right) for the flat plate boundary layer [29].**
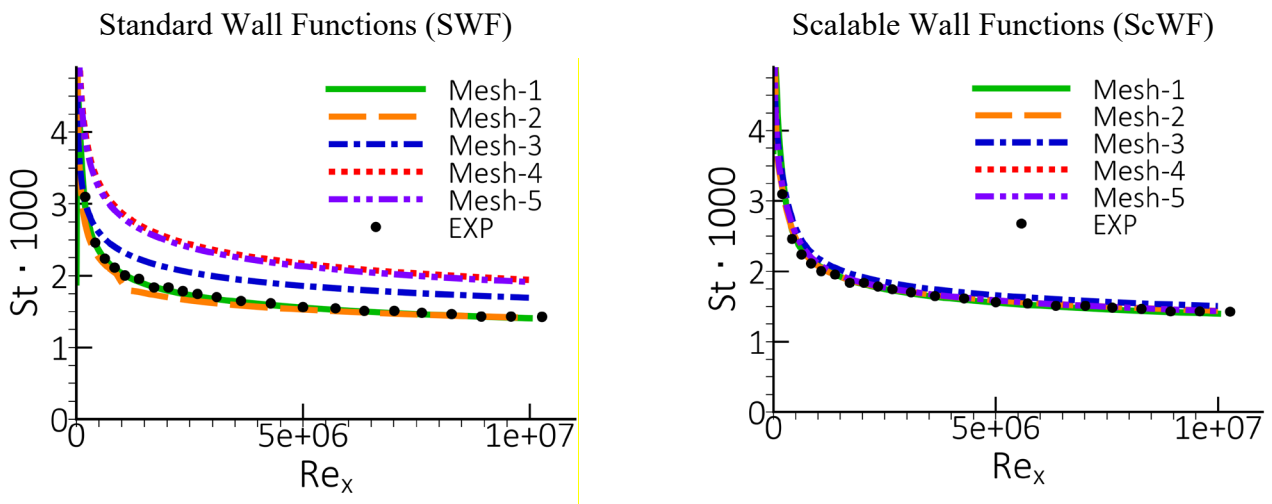
Standard Wall Functions (SWF)                    Scalable Wall Functions (ScWF)



**Figure 10: Distribution of the Stanton number over the flat plate computed with RKE model with SWF (left) and ScWF (right) for the flat plate boundary layer [29].**

## 4.2. **Adverse Pressure Gradients and Flow Separation**

Arguably the most important additional physical effect when developing turbulence models beyond equilibrium boundary layer flows, concerns their ability to accurately predict flows with pressure gradients and separation from smooth surfaces. This is of major importance in any external aerodynamic flow, especially airfoil and wing flows, where flow separation and stall are the defining factors of the performance envelope. However, separation from smooth surfaces is also relevant for internal flows, like diffusers and blades/vanes etc. For this reason, and because many turbulence models originate from the aeronautical community, separation prediction has always been a major focus in turbulence modeling. In more 'industrial' type flows, separation is often not

caused by a pressure gradient, but by a shape change in the geometry, like a step or a corner. In such cases, the separation point/line is fixed and there is much reduced turbulence model sensitivity. This needs to be considered during the discussion of model differences for smooth wall separation. In this section, 'separation' refers to separation from a smooth wall.

It is accepted knowledge in the turbulence modeling community that $k$-$\omega$ models are more suitable for predicting separation than $k$-$\varepsilon$ models [7]. This will be demonstrated for several flows in the following discussions. Since the Spalart-Allmaras 1-equation model is also a popular turbulence model in aeronautics, it is included in some of the comparisons.

### 4.2.1. NASA CS0 Diffuser

One of the most widely used test cases for evaluation of flow separation is the NASA CS0 diffuser of Driver [30], where a relatively shallow separation region has been created in the experiment. The test case geometry (partly shown in Figure 11 near the separation zone) consists of an axisymmetric diffuser with an internally mounted cylinder along the centerline. The boundary layer develops along the axis of the cylinder. The expansion of the diffuser wall causes an adverse pressure gradient. The Reynolds number based on the freestream velocity, $U_\infty$ and the cylinder diameter, $D$, is equal to $\mathrm{Re} = 2.8 \cdot 10^5$.
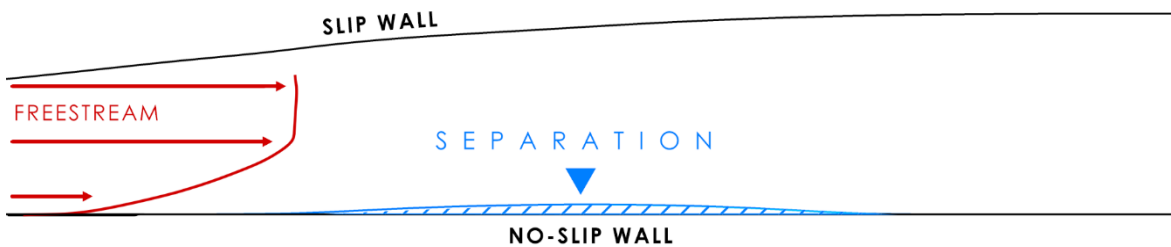


**Figure 11: Schematic of the flow in CS0 diffuser.**

The computational domain with boundary conditions is shown in Figure 12. At the inlet section, uniform streamwise velocity and turbulent quantities were specified. The outer radial boundary of the domain represents a streamline of the inviscid flow defined in the experiment, and so a free slip condition is imposed at this boundary. A no-slip condition is used on the internal cylinder wall everywhere except for the initial part where a symmetry condition is imposed (the length of the non-slip wall is adjusted to provide the correct boundary layer thickness at the first experimental section). Finally, a constant pressure condition is used at the outlet boundary.



**Figure 12: Computational domain with boundary conditions and mesh for CS0 diffuser.**

*Model Comparison*

Figure 13 shows a comparison of velocity profiles for different turbulence models at different locations in the diffuser compared with experimental data. The curves clearly indicate that the $k$-$\varepsilon$ model family shows a strong tendency to under-predict the effect of the adverse pressure gradient and the onset/amount of separation ($0 < X/D < 2$). The SA model does reproduce negative wall shear stresses in the separation zone, however the model underpredicts the height of the separation bubble.

Note that the tuned GEKO model ($C_{SEP} = 1$, $C_{NW} = 1$) is an exact transformation of the standard $k$-$\varepsilon$ models and therefore reproduces the $k$-$\varepsilon$ model behavior which is shown in Figure 14. It is also interesting to note that even when activating RSM (Reynolds Stress Model) model in combination with the $\varepsilon$-equation, the separation is still not predicted properly. Figure 15 shows the wall shear-stress and the wall-pressure coefficients $C_f$ and $C_p$ for the same models. The results confirm the conclusions reached from the velocity profiles.

It is interesting to note that $k$-$\varepsilon$ family models predict firmly attached velocity profiles, even though the wall shear stress approaches zero at around $X/D = 0$. This is the result of the two-layer formulation (detailed described in section 9.3.4) which allows for a very thin backflow region near the wall, even though the overall profile is attached. This is also consistent with the $C_p$ distribution, which shows a lack of flow displacement for the $k$-$\varepsilon$ models. Figure 16 shows the difference of the flow structure for the $k$-$\omega$ based and $k$-$\varepsilon$ based models.
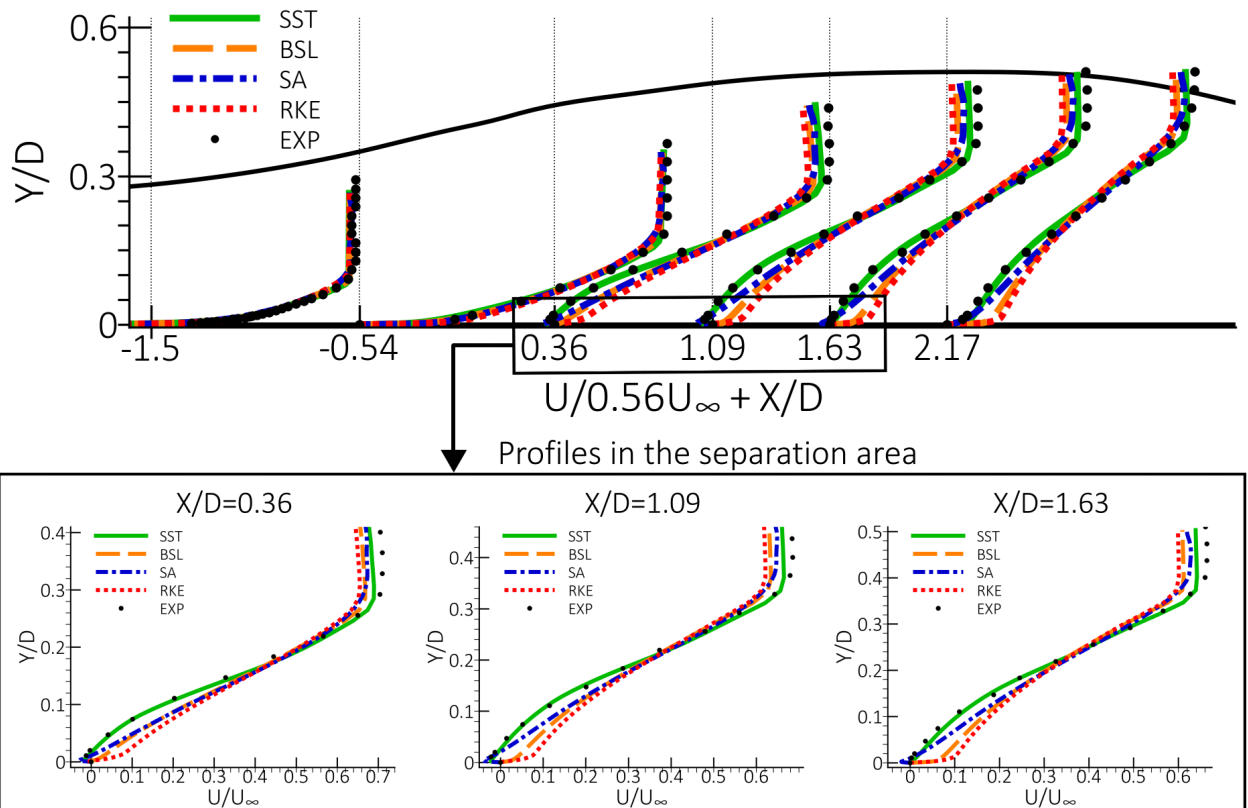


Figure 13: Comparison of velocity profiles predicted with different turbulence models for CS0 diffuser [30].
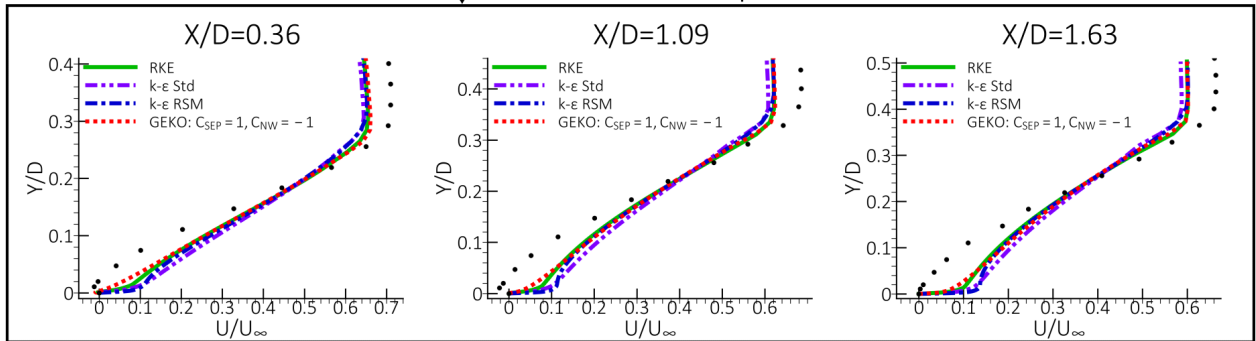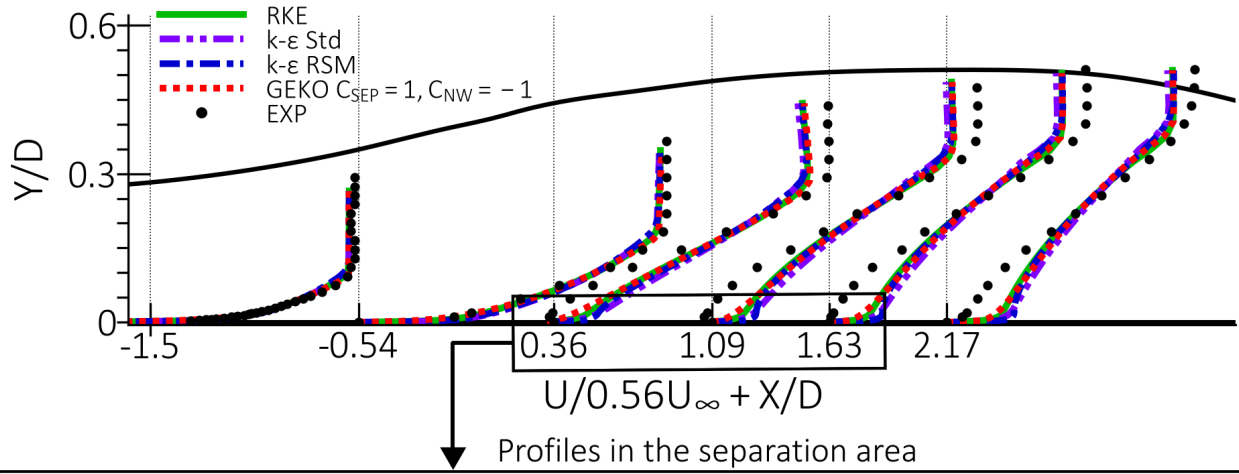
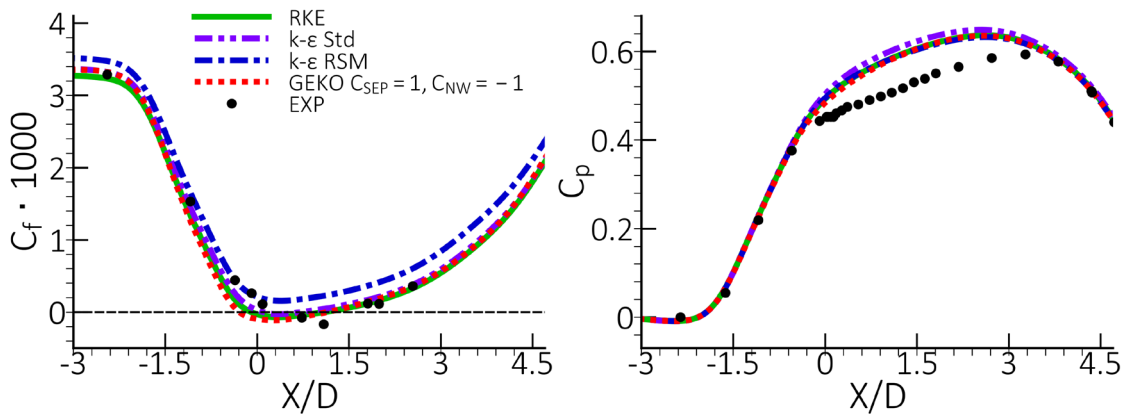**Figure 14: Comparison of velocity profiles for *k-ε* model family and GEKO models for CS0 diffuser [30].**



**Figure 15: Prediction of wall characteristics for *k-ε* family and GEKO models for CS0 diffuser [30]. Left: wall shear stress coefficient, $C_f$. Right: Wall pressure coefficient $C_p$.**
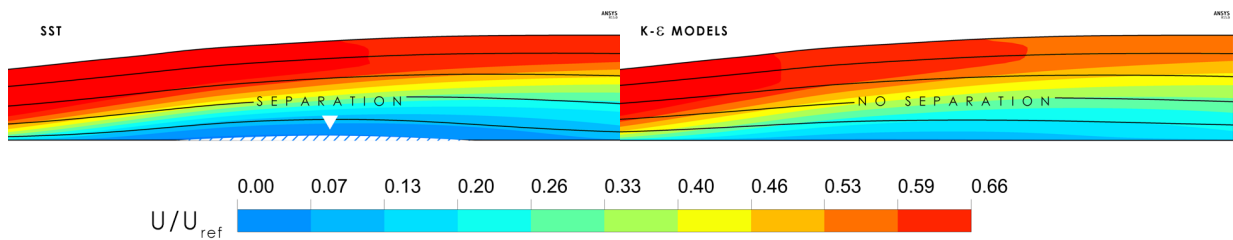


**Figure 16: Flow structured visualized with the streamwise velocity field and streamlines (black lines) for CS0 diffuser [30].**

## *GEKO Model Versatility*

Variations in the $C_{SEP}$ coefficient for the GEKO turbulence model are shown in Figure 17-Figure 20. As expected, with increasing of $C_{SEP}$, the model becomes more sensitive to the adverse pressure gradient in the diffuser and improves its separation predict up to a value of $C_{SEP} = 2.0$. Higher values

of $C_{SEP}$ lead to over-separation. It is the desired behavior of the GEKO model to allow for a wide range of calibration engulfing the experimental solution.
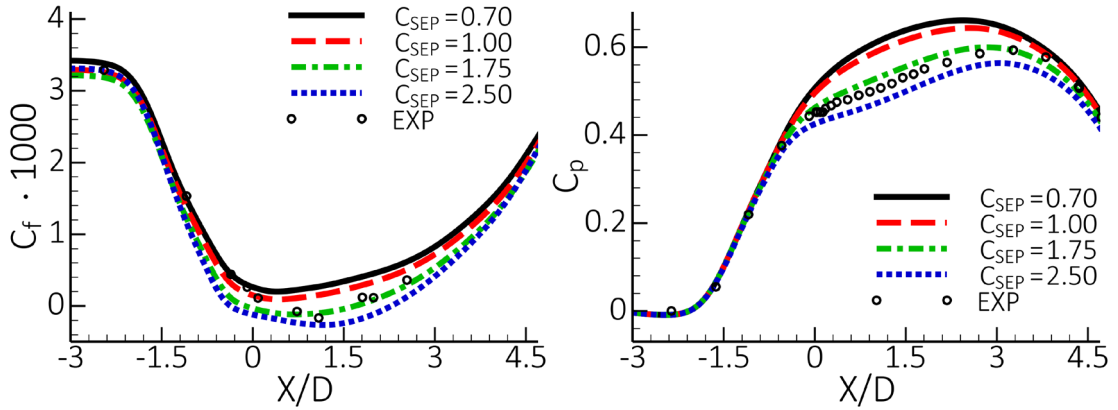


**Figure 17: Impact of variation in $C_{SEP}$ coefficient of the GEKO model for CS0 diffuser flow [30]. Left: wall shear stress coefficient, $C_f$. Right: Wall pressure coefficient $C_p$.**
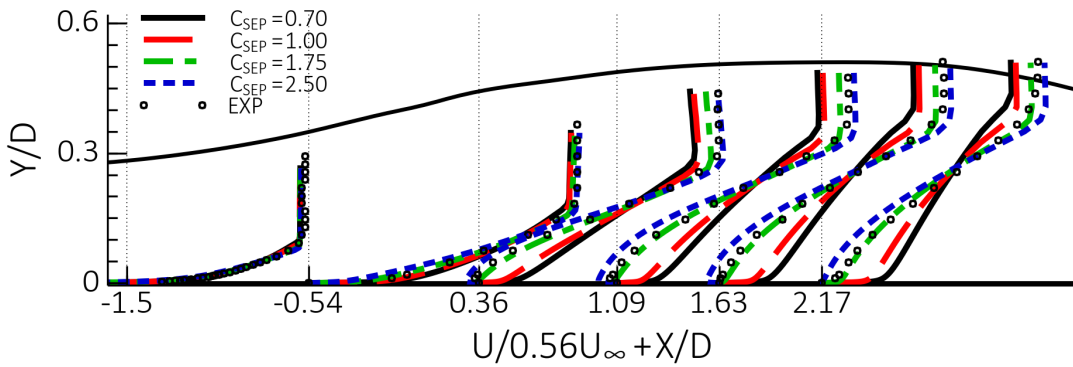


**Figure 18: Impact of variation in $C_{SEP}$ coefficient of the GEKO model on velocity profiles for CS0 diffuser flow [30].**
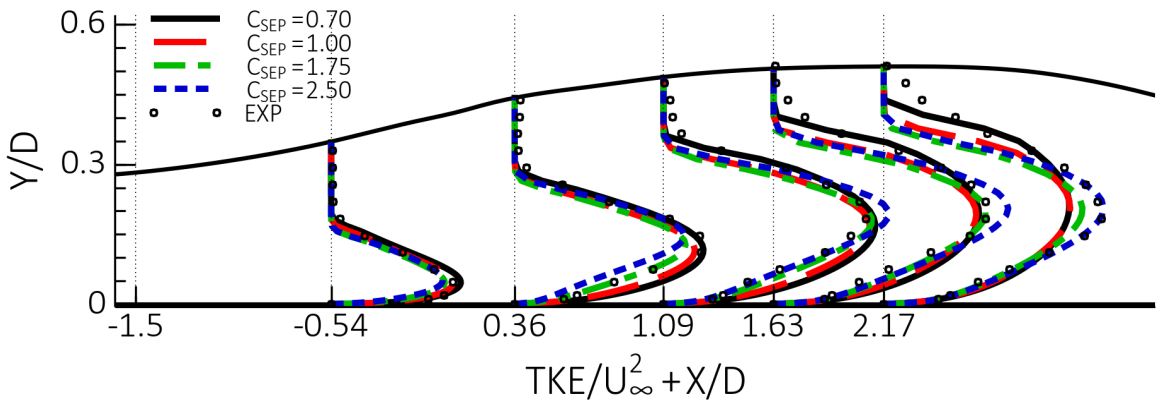


**Figure 19: Impact of variation in $C_{SEP}$ coefficient of the GEKO model on turbulence kinetic energy profiles for CS0 diffuser flow [30].**
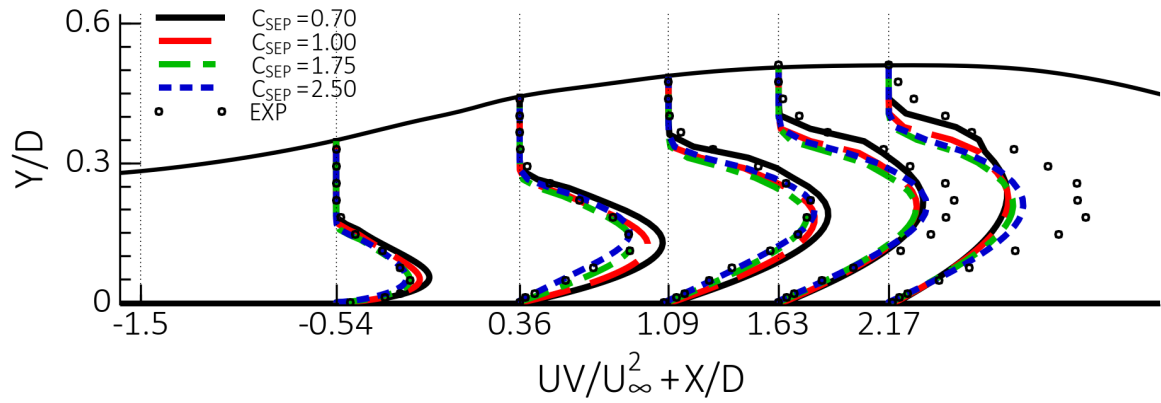
**Figure 20: Impact of variation in $C_{SEP}$ coefficient of the GEKO model on turbulence shear stress profiles for CS0 diffuser flow [30].**

*Non-linear effects*

Figure 21 shows the results of the GEKO model with (EARSM) and without non-linear terms. Here GEKO-1.00/1.75 corresponds to different values of $C_{SEP}$ = 1.00/1.75. Considering turbulence anisotropy of the Reynolds stress tensor has negligible effect on the prediction of the skin friction coefficient, however the prediction of the pressure distribution is very sensitive. The flattening of the $C_p$-distribution indicates that the flow is more separated when including the EARSM terms. This is expected as the EARSM model has a similar effect as the SST limiter, by accounting for the transport of the principal shear stress and thereby reducing the increase in the shear stress level as separation is approached. The effect of including the EARSM formulation is therefore like an increase in $C_{SEP}$ for the standard GEKO model.
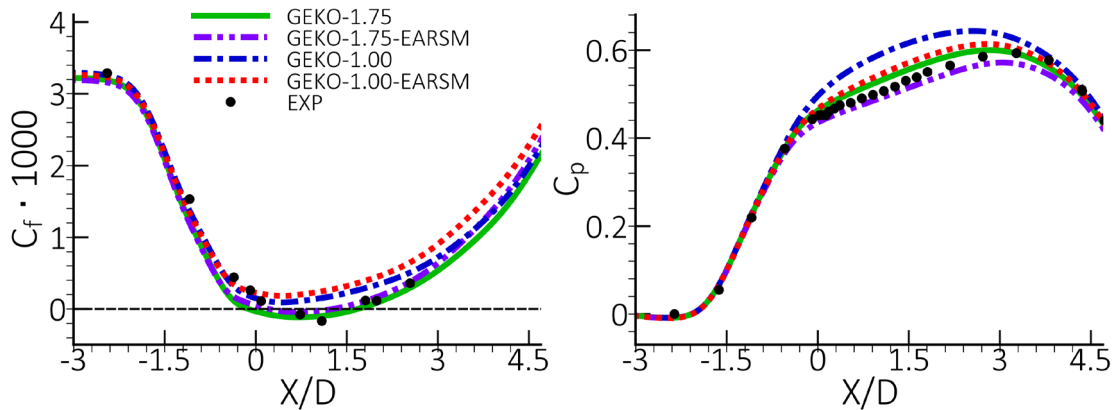


**Figure 21: Impact of non-linear terms for the GEKO model for CS0 diffuser flow [30]. Left: wall shear stress coefficient, $C_f$. Right: Wall pressure coefficient $C_p$.**

## 4.2.2. Airfoil Flows

The accurate prediction of airfoil characteristics especially in regimes near stall where the flow is separated and maximal lift is achieved, is an important task for aviation and wind power, as well as for turbomachinery flows. Figure 22 shows the schematic for such a situation, where the separation zone on the suction side is significant and plays a key role in the prediction of the airfoil characteristics.
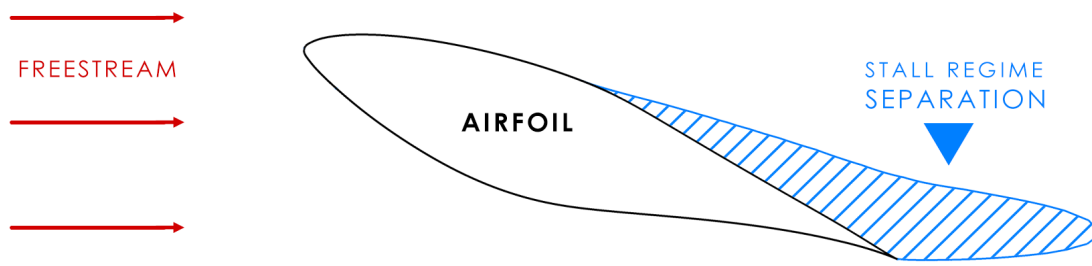
**Figure 22: Schematic of the flow around an airfoil for stall regime.**

Six aerodynamic airfoils with different shapes and thicknesses (from 13% to 30%) are considered [31]–[35]. Experimental investigations were carried out in low turbulence rectangular wind tunnels (Tu < 1%) at relatively high Reynolds numbers (Re > $10^6$) based on airfoil chord $C$ and freestream velocity. The airfoil shapes and more detailed information about the experiments are shown in the Table 2. For all the airfoils, except DU-97-W-300, the boundary layer was tripped with the use of a short rough tape placed at the leading edge. It is therefore assumed that the flow around these airfoils is fully turbulent and that only for the «clean» DU-97-300 airfoil a model for laminar turbulent transition should be considered. For this airfoil, the additional intermittency equation [36] is therefore solved together with the $k$ and $\omega$-equations. Since the experimental Mach number did not exceed 0.15, incompressible flow is assumed in all cases.

The computations are carried out with inclusion of the wind tunnel walls. Inlet and outlet boundaries are located 10$C$ upstream of the leading edge and downstream of the trailing edge airfoil, respectively. A constant velocity is specified at the inlet section of the computational domain. No-slip conditions are used on the airfoil boundary and constant pressure is specified at the outlet. Symmetry boundary condition are specified on the wind tunnel upper and lower walls for imitation of slip-walls. The inlet turbulence kinetic energy matches the experimental turbulence intensity, and the specific dissipation rate is specified as $\omega = 10 \cdot U_\infty/C$.

**Table 2: Considered airfoils and parameters of wind tunnel and flow in the experiments**

| Airfoil | Thickness | Surface | Wind Tunnel Height | Re/$10^6$ |
|---------|-----------|---------|--------------------|-----------|
| S805 | 13.50% | Tripped | 3.60$C$ | 1.00 |
| S825 | 17.10% | Tripped | 5.00$C$ | 2.00 |
| S809 | 21.00% | Tripped | 3.00$C$ | 2.00 |
| S814 | 24.00% | Tripped | 2.76$C$ | 1.50 |
| DU-97-W-180 | 18.00% | Tripped | 3.00$C$ | 3.00 |
| DU-97-W-300 | 30.00% | Clean | 3.00$C$ | 3.00 |
| NACA-4412 | 12.00% | Tripped | 2.73$C$ | 1.64 |

*Model Comparison*

For flows around airfoils, the maximum lift coefficient and corresponding angle of attack are systematically overpredicted by the Reynolds Averaged Navier-Stokes (RANS) approach in

combination with standard RANS turbulence models. For example, the predicted lift coefficient for the different turbulence models for the S809 airfoil is shown in Figure 23 (left). The disagreement between computations and experimental data is caused by delay of turbulent boundary layer separation under adverse pressure gradient on the suction side of the airfoils which is shown in Figure 23 (right). Even the most aggressive SST and GEKO (default conditions) models predict separation too late (at $X/C \approx 0.95$) while in the experiment the separation on the suction side occurs near the mid-chord (at $X/C \approx 0.5$). Since the separation position is controlled by the turbulence model, one of the ways to improve the accuracy of the airfoil characteristics prediction is a special tuning of the models for this class of flows.
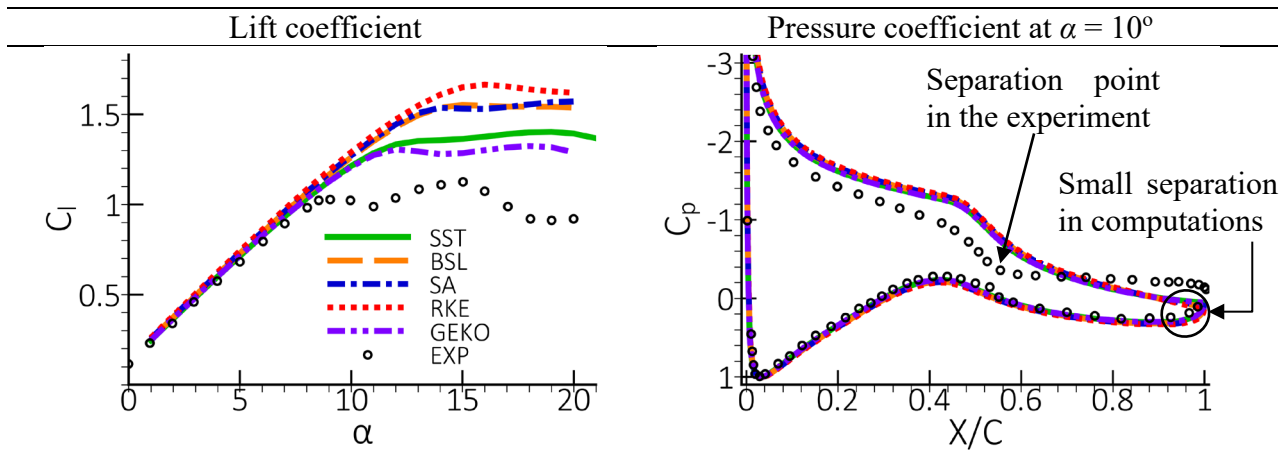


**Figure 23: Prediction of lift coefficient in wide range of angle of attacks for different turbulence models for S809 airfoil at Re=2·10⁶ [33].**

*GEKO Model Tuning*

The simplest way of model turning without violating the basic flows calibration is to increase the $C_{SEP}$ coefficient of the GEKO model. This coefficient (default value is $C_{SEP}$=1.75) affects the size of separation bubble: for higher $C_{SEP}$ values the separation is larger. Figures 24-28 compare lift curves for $1.75 \leq C_{SEP} \leq 2.5$ for all the considered airfoils. In these comparisons, it should be kept in mind that 2D simulations are not correct in the post-stall region, due to the formation of 3D structures in the experiments [37]. Despite this, it is possible to adjust the GEKO model for the prediction of such flows for angles of attack up to stall using 2D simulations. The GEKO-2.50 (GEKO with $C_{SEP}$ = 2.5) model predicts earlier separation on the suction side of the airfoils than other model variants, which improves agreement of the predicted both integral (lift coefficient) and local (pressure coefficient) airfoil characteristics with the experimental data near stall. However, the GEKO-2.50 model underpredicts the lift coefficient for low angles of attack for the thickest DU-97-W-300 and S814 airfoils (30% thickness) which is undesirable. The optimal $C_{SEP}$ value is therefore between $C_{SEP}$=2.00-2.50.
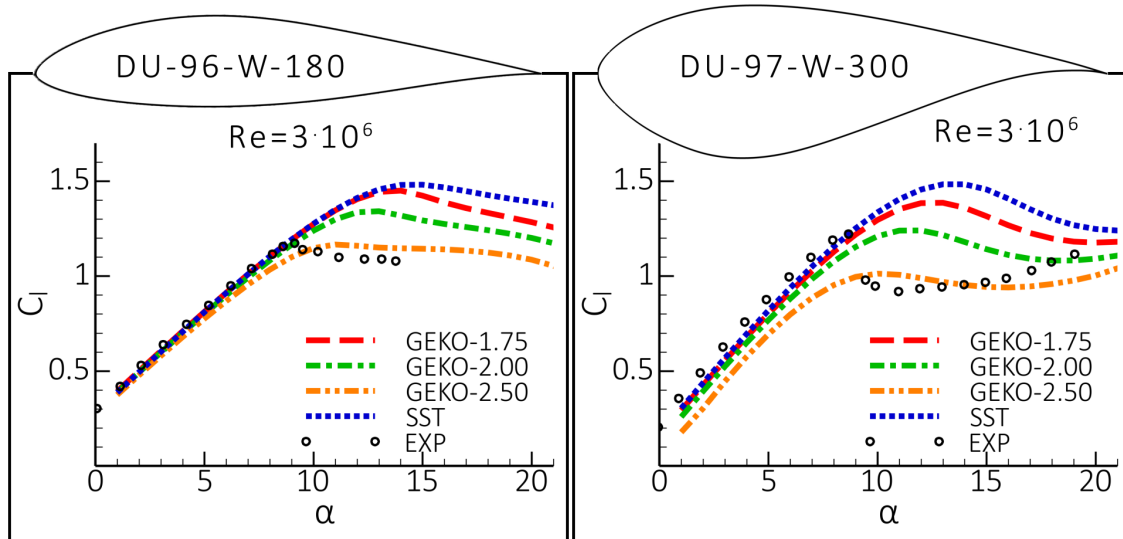
**Figure 24: Prediction of lift and pressure coefficients with GEKO model for DU-96-W-180 [35] (Left) and DU-97-W-300 [35] (Right) airfoil at Re=3·10$^6$**
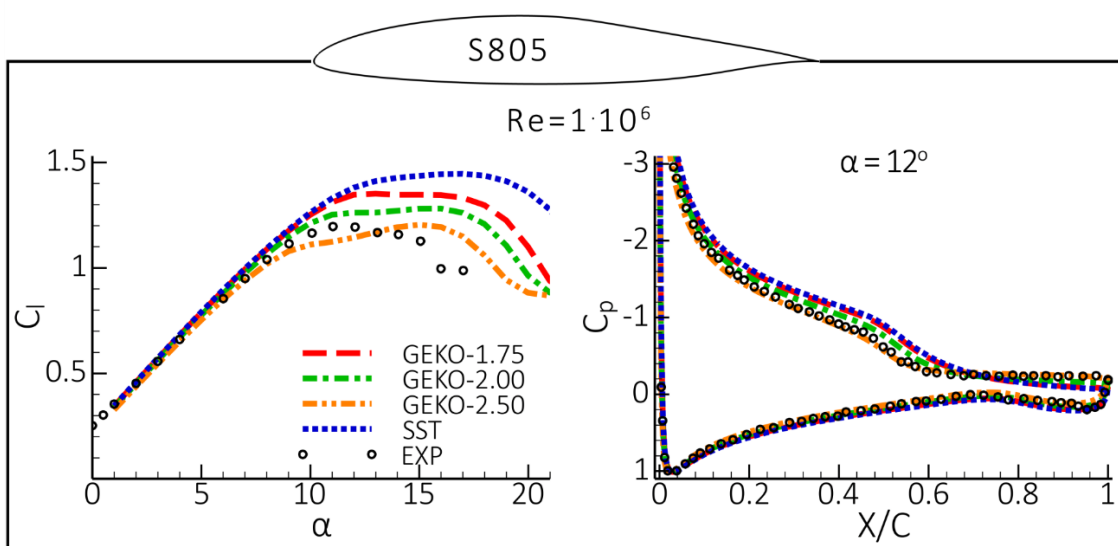


**Figure 25: Prediction of lift coefficient in wide range of angle of attacks (Left) and pressure coefficient for α = 12º (Right) with GEKO model for S805 airfoil at Re=1·10$^6$ [31]**



**Figure 26: Prediction of lift coefficient in wide range of angle of attacks (Left) and pressure coefficient for α = 17º (Right) with GEKO model for S825 airfoil at Re=2·10$^6$ [32]**

**Figure 27: Prediction of lift coefficient in wide range of angle of attacks (Left) and pressure coefficient for α = 10º (Right) with GEKO model for S809 airfoil at Re=2·10⁶ [33]**
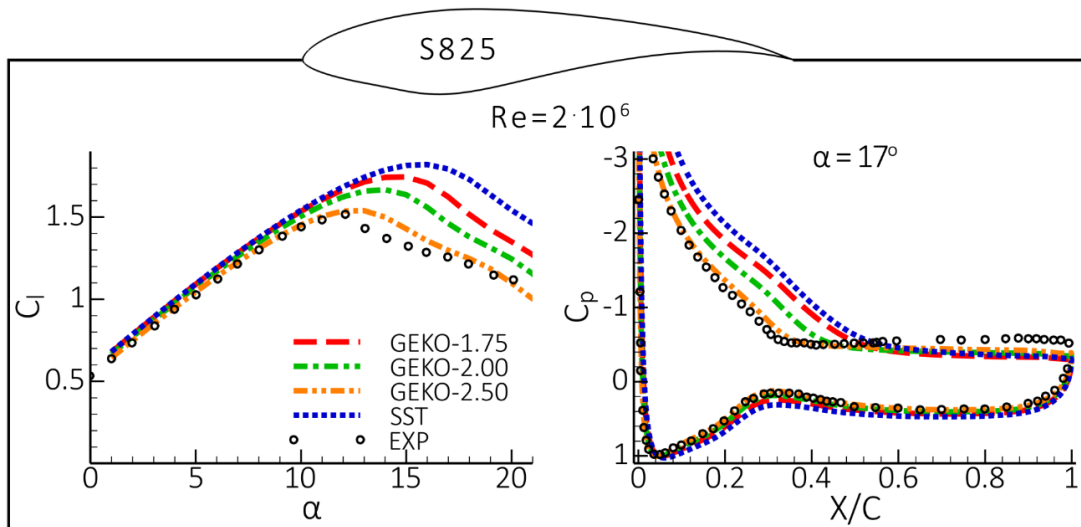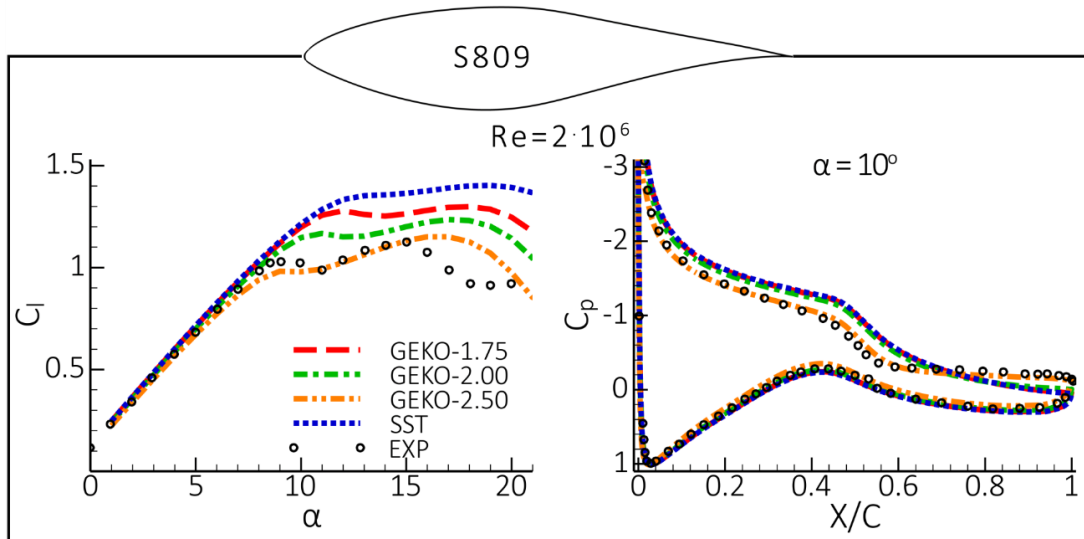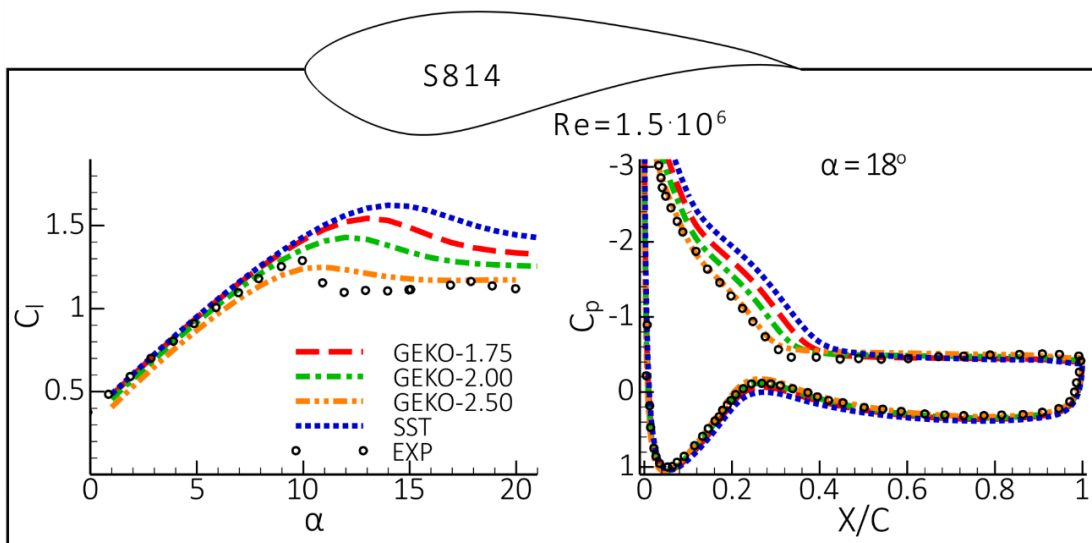


**Figure 28: Prediction of lift coefficient in wide range of angle of attacks (Left) and pressure coefficient for α = 18º (Right) with GEKO model for S814 airfoil at Re=1.5·10⁶ [34]**

*Non-linear effects*

An example of considering non-linear effects for the GEKO model using an EARSM model is presented next. Figure 29 shows the effect of the non-linear WJ-EARSM terms for the NACA-4412 airfoil for the GEKO-1.75 ($C_{SEP}$ = 1.75) model. The use of the non-linear terms slightly increases separation on the suction side of the airfoils. However, the effect is much weaker than the model tuning with the $C_{SEP}$ coefficient shown above.

**Figure 29: NACA-4412 airfoil near the trailing edge with streamwise velocity profiles at measurement locations predicted with linear and non-linear GEKO-1.75 model compared with the experimental data [38].**
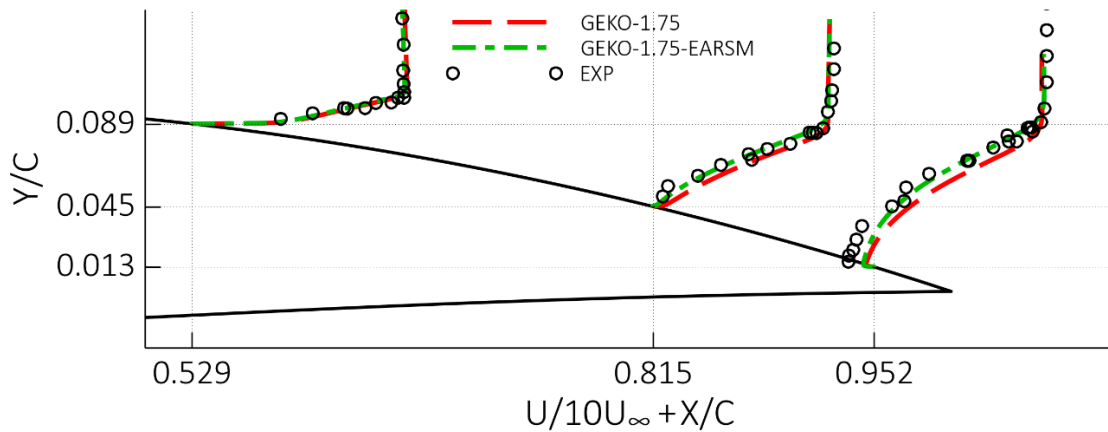
### 4.2.3. Transonic Bump Flow

Transonic compressible flow past an axisymmetric bump was simulated at conditions corresponding to the experiments of Bachalo & Johnson [39]. The bump was placed over a cylindrical pipe, and the entire geometry is axisymmetric. The incoming Reynolds number based on the bump chord length was Re = $2.763 \cdot 10^6$. The dynamic viscosity was set to Sutherland's law and the Prandtl number was set to Pr = 0.71.

The NASA Bump flow features a subsonic inflow with Ma=0.875. The flow is then accelerated to supersonic speed over the bump and then reverts to subsonic speed through a shock wave. The shock causes the boundary layer behind the shock to separate, which in turn interacts with the shock by pushing it forward. The ability to predict the shock location is therefore directly linked to a model's ability to predict boundary layer separation.
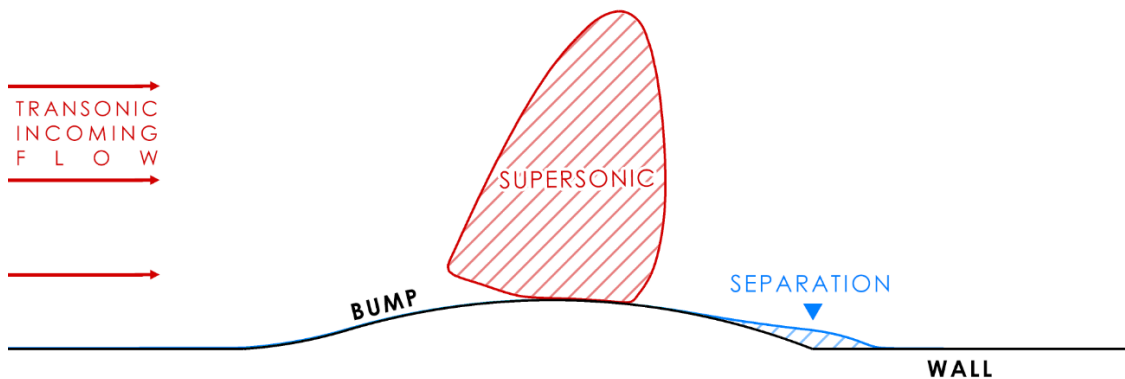


**Figure 30: Scheme of the transonic bump flow**

The size of the computational domain as illustrated in Figure 31 was about 12$C$×4$C$ ($C$ is the bump length). The inlet boundary is located 6.89$C$ upstream of the bump. Constant total pressure of $P_{tot}$ = 106595 Pa and total temperature of $T_{tot}$= 322 K are assigned at the inlet section of the computational domain. Turbulence characteristics over the inlet are also assumed constant with values corresponding to a free-stream turbulence intensity of Tu=0.1%, and an eddy-viscosity ratio of TVR=1. A no-slip condition is used on the wall and a constant pressure is specified at the outlet boundary. The computational mesh shown in Figure 31 is refined in streamwise direction over the bump for proper resolution of the shock wave.
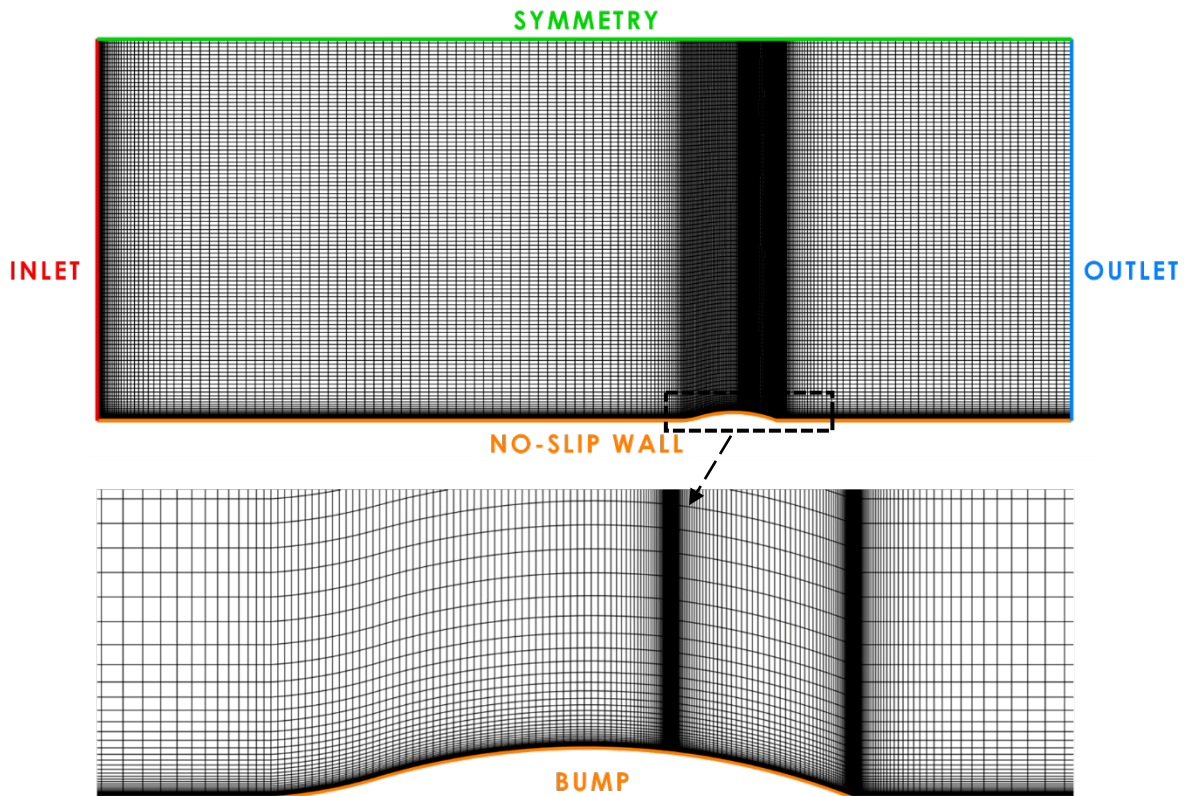
**Figure 31: Computational domain with boundary conditions and mesh for the NASA Transonic Bump [39]**

As expected, again, the models form two groups with GEKO-1.75/SST and GEKO-1.00/RKE as seen from Figure 32. Only the GEKO-1.75/SST model can predict the shock location and the post-shock separation zone properly. The GEKO-1.00/RKE models fail due to their lack of separation sensitivity. Like for the other described cases, the non-linear terms show less influence on the size of separation zone than the choice of the turbulence model, Figure 33.



**Figure 32: Comparison of wall pressure coefficient, $C_p$ for the transonic bump flow [39]. The bump starts at X/C=0 location. Left: comparison of the different turbulence models, right: versatility of the GEKO model with the $C_{SEP}$ variation (GEKO-1.75: $C_{SEP}$=1.75).**

**Figure 33: Comparison of different $C_{SEP}$ settings and ERSM inclusion for the transonic bump flow [39]. Left: wall shear stress coefficient, $C_f$, right: wall pressure stress coefficient $C_p$**
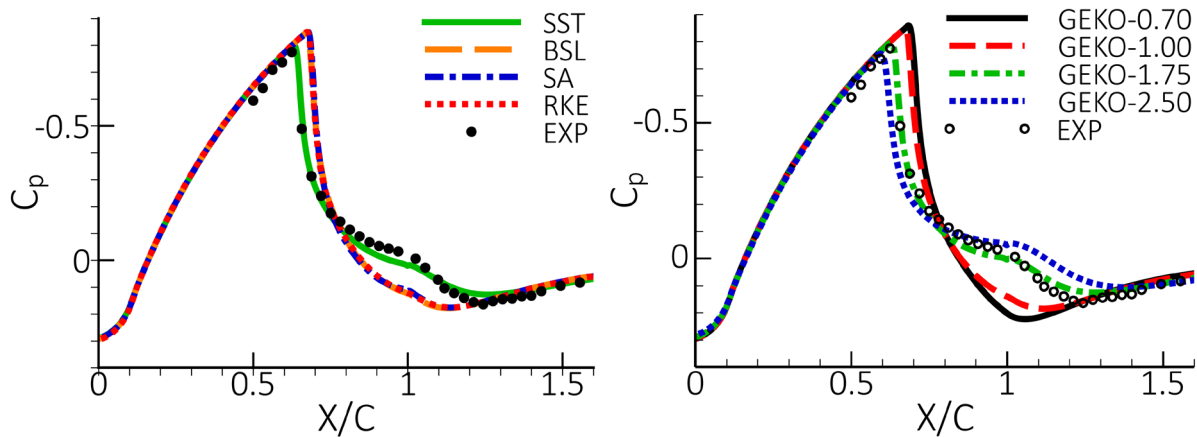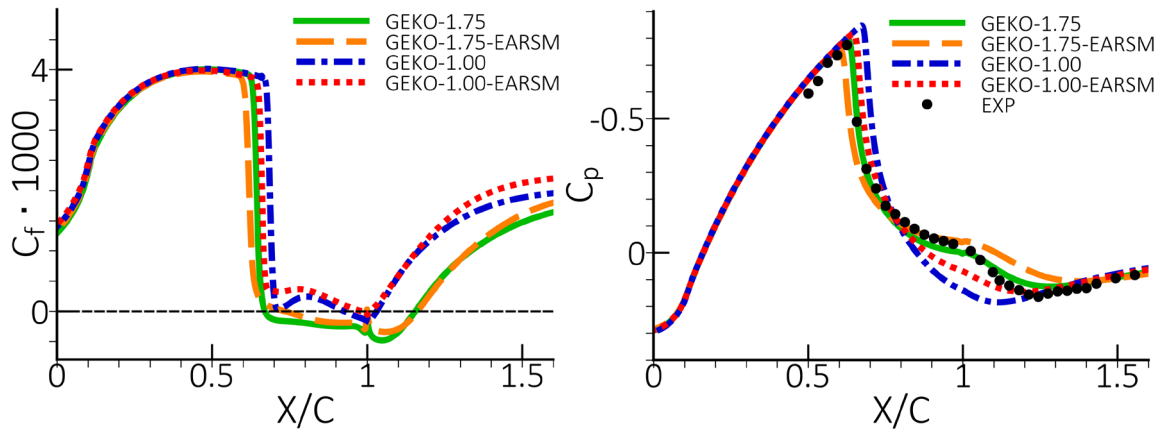
## 4.3. Corner Flows

As described in section 3.4.3, eddy-viscosity models need special corrections for the prediction of the secondary flows in corners. In this section, the effect of the use of CFC (Corner flow Correction) [22], [23] and EARSM terms from the Wallin-Johansson [19] model (see section 3.3.3) in combination with different $k$-$\omega$ models is shown for flows in rectangular channels and diffusers. For these flows, only the inclusion of the non-linear terms allows the prediction of the secondary flows in the corners.

Thus, the main goal of this section is to demonstrate the improvement in the prediction of the secondary motion in corners with the use of the non-linear turbulence models. The non-linear effects are shown for the GEKO model in combination with the Corner Flow Correction (CFC) and EARSM. The effect of these terms on other models like the SST model would be similar.

### 4.3.1. Developed Flow in Square Duct

The simplest case demonstrating the impact of the secondary motion on the main flow is the developed flow in square duct. For this flow, the linear eddy-viscosity models are not capable to predict secondary motion into the corners. This effect is shown in Figure 34.
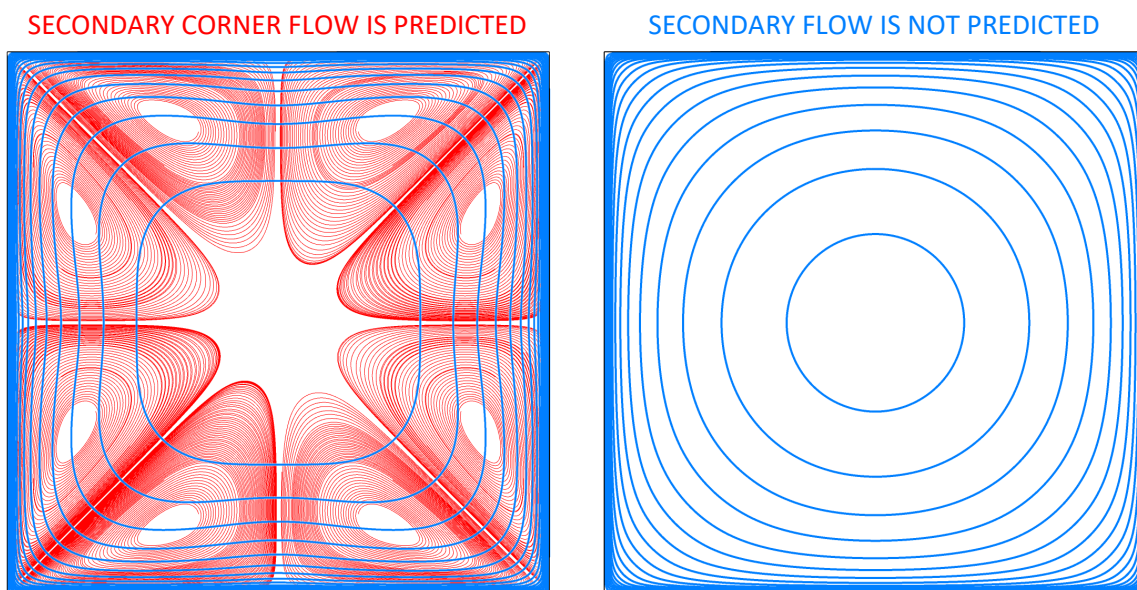


**Figure 34: Flow topology in the square duct case predicted using the GEKO model with CFC (left) and without CFC (right). Blue lines: iso-surfaces of the streamwise velocity, red lines in the corners: streamlines of the secondary motion.**

The computations are performed with the linear and non-linear GEKO-CFC model under the conditions of the reference DNS data [40], namely at a Reynolds number based on the averaged friction velocity $u_\tau$ and the channel width, $H$, equal to $Re_\tau=1200$. The computations were carried out in a "2.5D mode", which include momentum equations for all the 3 velocity components but assumed that their streamwise derivatives are zero. A constant streamwise pressure gradient is specified to achieve the DNS Reynolds number. At solid walls, no-slip boundary conditions are imposed.

The streamlines in the cross-section show that the non-linear GEKO model can predict secondary flow, while the linear GEKO model cannot (see Figure 34). The flow structure of GEKO-1.00, GEKO-1.75 and WJ-BSL-EARSM model is virtually the same (not shown). Streamwise and lateral velocity profiles along a diagonal line (X=Y) predicted by the GEKO-EARSM models are in reasonable agreement with the DNS data (see Figure 35).
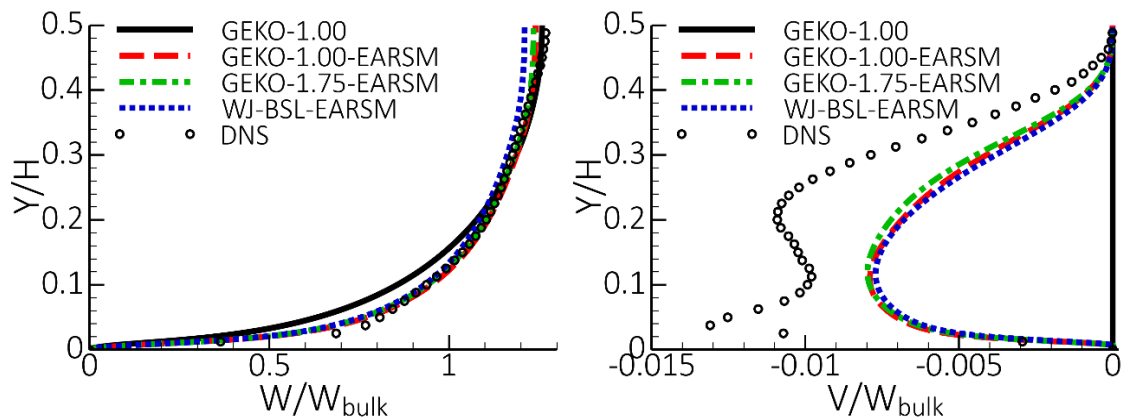


**Figure 35: Streamwise (Left) and lateral (Right) velocity profiles on the diagonal of the square duct case [40].**

### 4.3.2. Flow in Rectangular Diffusers

Flow in rectangular diffusers is a much more challenging test case than the fully developed channel flow, since it involves the effect of turbulence anisotropy combined with an adverse pressure gradient causing separation of the flow. Two diffusers are considered: the symmetric DLR diffuser [41] and the asymmetric Stanford diffuser [42], [43] where the flow is highly sensitive to the secondary flow prediction.

*DLR-Diffuser*

Flow is modeled based on the experimental study in the framework of DLR project *VicToria* to investigate 3D separated flow, which occur at end wall junctions. The diffuser configuration with the expansion ratio of ER = 2.0 was considered in the CFD study is shown in Figure 36. Computational domain together with boundary conditions is shown in Figure 37. The inlet condition is unform flow with U=10 m/s Tu=1% and TVR=1. A no-slip condition is used at the wall and a constant pressure is specified at the outlet boundary. The origin the of coordinate system is located on the centerline of the flat wall coincident with the start of the ramp. The X-axis is aligned with the streamwise direction, the Y-axis defines the spanwise direction while the Z-axis coincides with the expansion direction of the channel. Reynolds number based on the inlet bulk velocity and cross-section of internal width $h$ is Re = $5.1\cdot10^4$.

For this case, the linear models predict two recirculation zones starting from the inclined-side wall corner as shown in Figures 38-39. In contrast, the secondary flow predicted with non-linear model prevents corner separation and pushes the recirculation zone to the inclined wall, while flow on the side wall is virtually attached. The dramatic difference in flow topology, visualized by the wall-streamlines on the inclined wall with the linear and non-linear GEKO model is shown in Figures 38- 39.
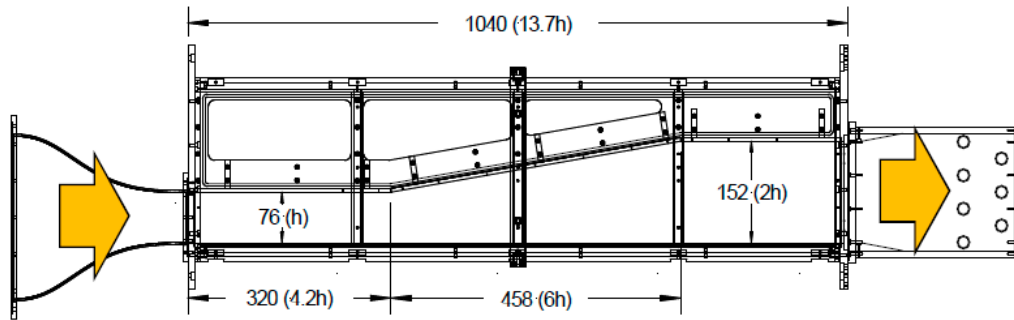
**Figure 36. DLR diffuser configuration [41].**
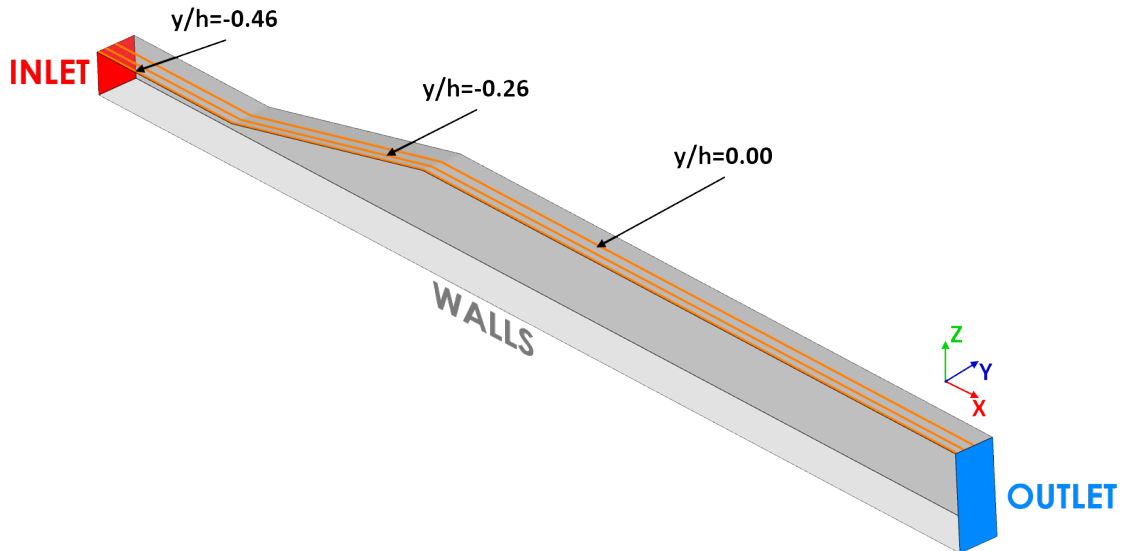


**Figure 37: Computational domain with the boundary conditions for the DLR diffuser [41].**

A comparison of the predicted skin friction coefficient with the experimental data (Figure 40) shows that the use of the non-linear models improves the prediction of the flow near the corner (y/h=0.46) where the linear models predict large corner separations. In contrast, the flow near the midsection (y/h=0) of the diffuser in not so sensitive to the non-linear effects. However, all the models predict an attached boundary layer at the midsection, while in the experiment the flow separates. Despite the different flow topologies for linear and non-linear models, the pressure distribution at the midsection (Figure 41) agrees with the experimental data for all the models.
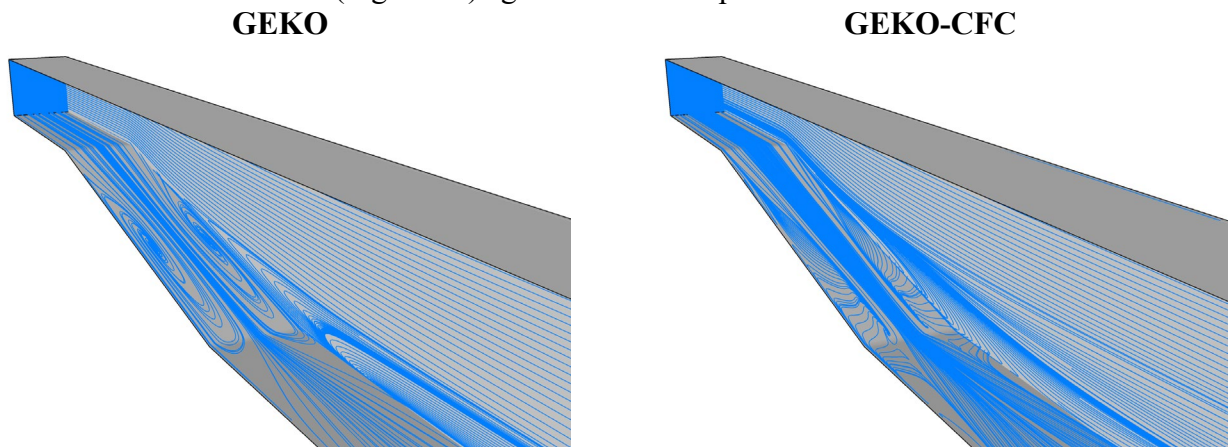
GEKO                                                    GEKO-CFC



**Figure 38. The surface streamlines near the inclined and side walls plotted for the for the linear (left) and non-linear GEKO model with corner flow correction (right) for the DLR diffuser [41].**

GEKO                                                    GEKO-CFC
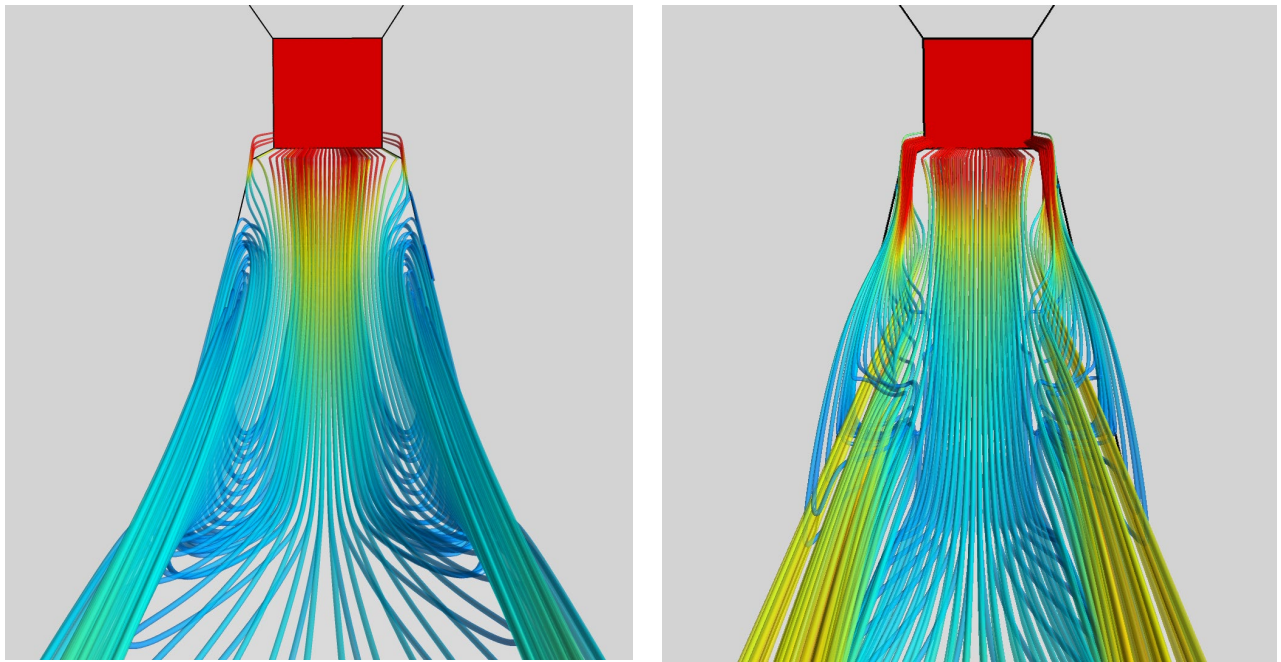
**Figure 39: Flow topology for the linear (left) and non-linear GEKO model with corner flow correction (right) for the DLR diffuser [41].**
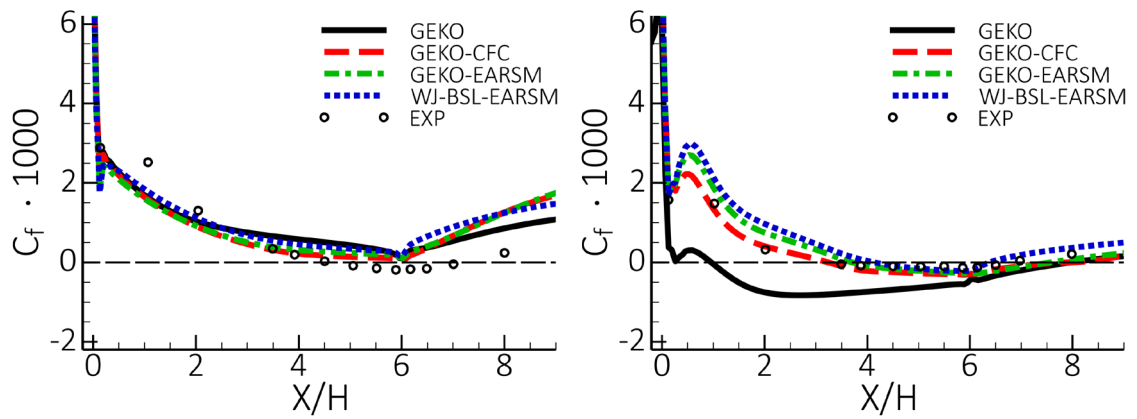


**Figure 40: Distribution of the skin friction along the diffuser at midsection (left) and near the corner (right) for turbulence models with and without non-linear terms for the DLR diffuser [41].**
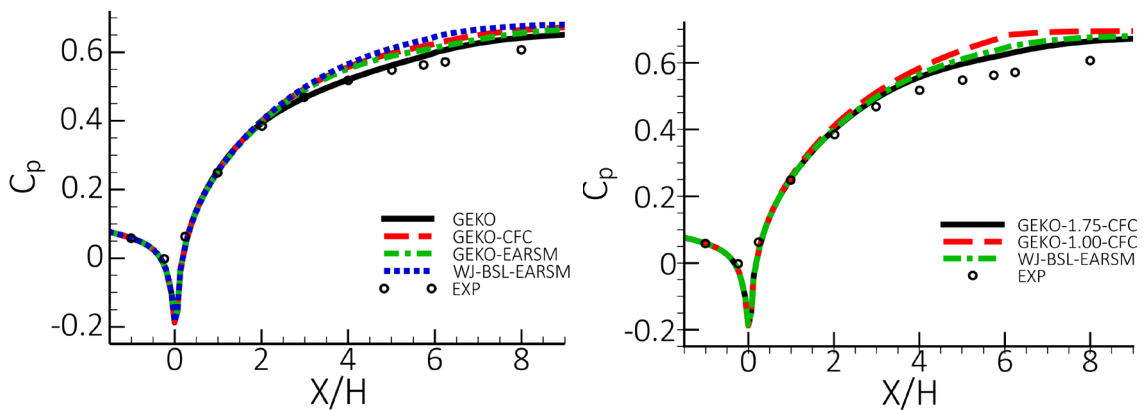


**Figure 41: Distribution of the pressure coefficient along the diffuser at midsection for turbulence models with and without non-linear terms for the DLR diffuser [41].**

## Stanford Diffuser

This flow studied experimentally by Cherry et al. [42], [43] is even more challenging than the flows considered above. For this case, separation has proven to be very sensitive to details of turbulence modeling. It seems clear that the anisotropy of the normal stresses must be accounted for to avoid the formation of an incorrect flow topology.

The geometry of the diffuser is shown in Figure 42. The top wall of the diffuser is inclined by an angle of 11.3 degrees. To achieve asymmetry, one the side walls is inclined by 2.56 degrees. The coordinate system used in the computations is shown in Figure 43. The origin of the coordinate system in the X-direction is located at the cross-section of the diffuser corresponding to the intersection of its straight and inclined walls in the Y- and Z-directions; it is in the vertex of the dihedral angle formed by the straight walls of the diffuser.

In accordance with the experimental setup, the inlet flow is considered as fully developed flow in a rectangular duct with the bulk velocity providing a Reynolds number of Re = $10^4$. The velocity in the inlet plane is specified using precursor computations of the developed rectangular channel flow with the same turbulence model used later for the diffuser simulation. The computations were carried out with the GEKO model with and without corner flow correction (CFC), GEKO-EARSM model and differential Reynold-Stress GEKO model (GEKO-RSM).
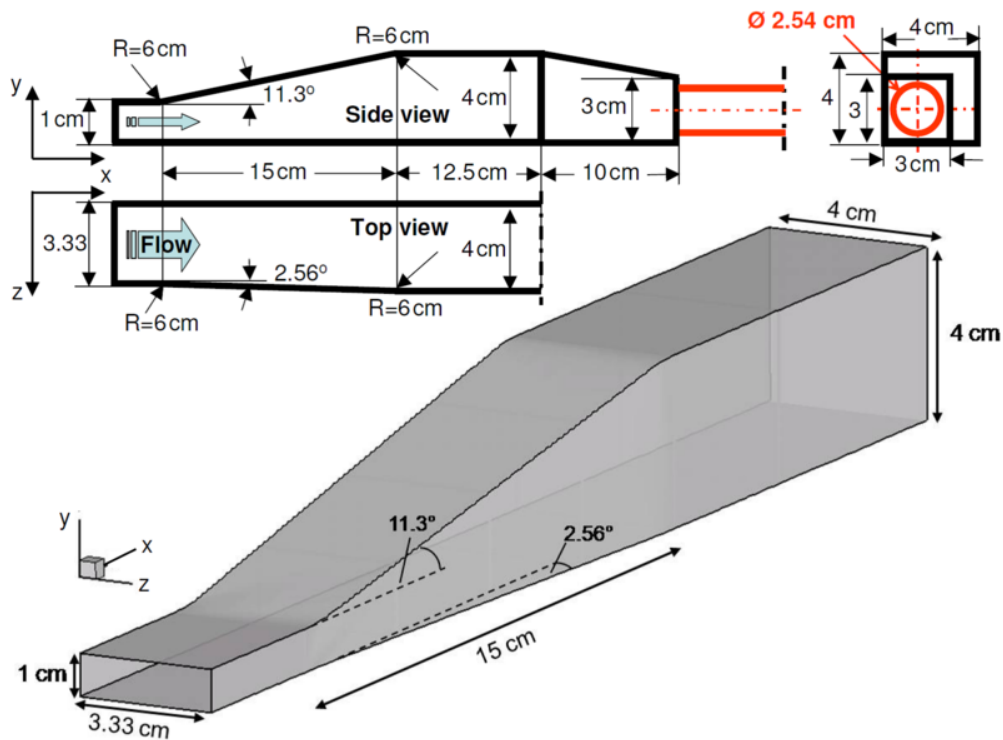


**Figure 42: Geometry of Stanford diffuser [42], [43].**
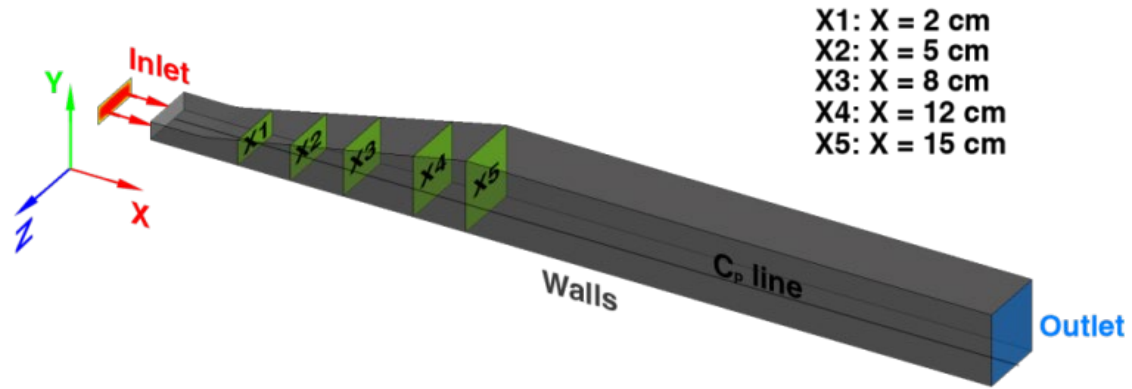
**Figure 43: Computational domain with boundary conditions for the Stanford diffuser [42], [43].**

Figure 44 shows the 3D flow topology for the linear, the non-linear GEKO model and the experiment (note that these pictures are turned by 180° for visualization purposes). It is well seen that in the experiment the separation occurs mainly on the strongly inclined wall. The linear GEKO model predicts massive corner separation in the expanding part of the diffuser and separation occurs on the non-inclined side wall. The non-linear model decreases the size of the corner separation zone which dramatically changes the flow topology. For the non-linear model, the separation occurs mainly on the strongly inclined wall which is in better agreement with the experimental flow topology. The effects of the nonlinearity on the flow topology are also shown on Figure 45 where the streamwise velocity contours at section X5 are plotted (blue colors indicates negative values). The non-linear terms change the separation zone location (from the side wall to the inclined wall). The results of all the non-linear models are close to each other.
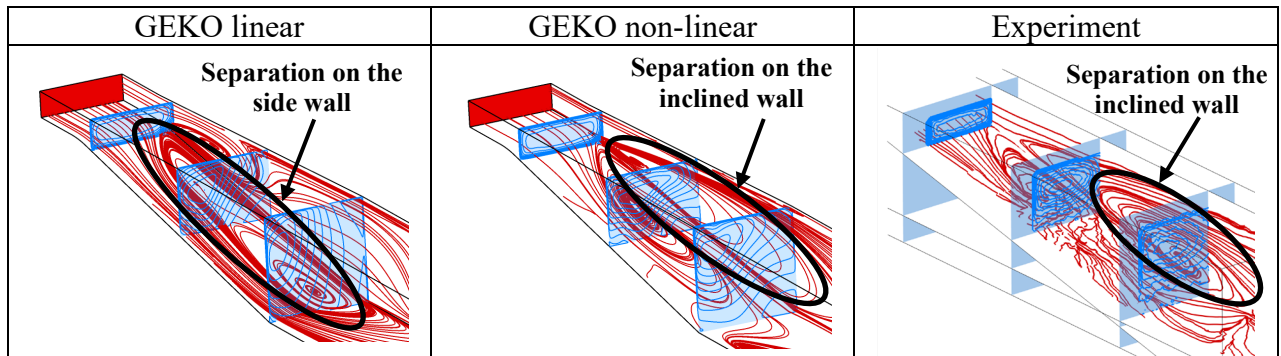


**Figure 44: Flow topology for the linear (left) and non-linear CFC-GEKO model (middle) for the Stanford diffuser. Experimental data (right) [42], [43].**



**Figure 45: Streamwise velocity contours predicted be the linear and non-liner GEKO ($C_{SEP}$ = 1.00) model at X5 section. Blue colors indicate recirculation zone.**

Interestingly, the flow topology for the non-linear models also depends on the baseline linear model. Figure 46 shows that the increase of $C_{SEP}$ in the GEKO model from $C_{SEP} = 1.00$ to $C_{SEP} = 1.75$ leads a separation on both, the side and inclined wall. The effect of the $C_{SEP}$ value on the prediction of the pressure coefficient is shown in Figure 47. As seen, the more aggressive $C_{SEP}$ settings (higher $C_{SEP}$) fail to capture the overall pressure distribution.

As the tests indicate, this flow is extremely sensitive to modeling details, as it allows for topology changes in the solution based on model settings. Poor results are obtained for $C_{SEP} = 1.75$, as typically chosen for aerodynamic flows. This might be a result of the large separation zone predicted by the model. Such zones tend to be poorly predicted by RANS as the reattachment dynamics can be dominated by small-scale shedding from the separation line. As such effects are not included in RANS, it can lead to overly large separation zones. The error can be reduced by more conservative settings e.g. for $C_{SEP} = 1$, which delays separation and thereby reduces the separation zone. While giving a better overall agreement with data, it could be the result of a cancelation of errors. This example shows that seemingly simple experimental configurations can still pose severe challenges to RANS modeling.

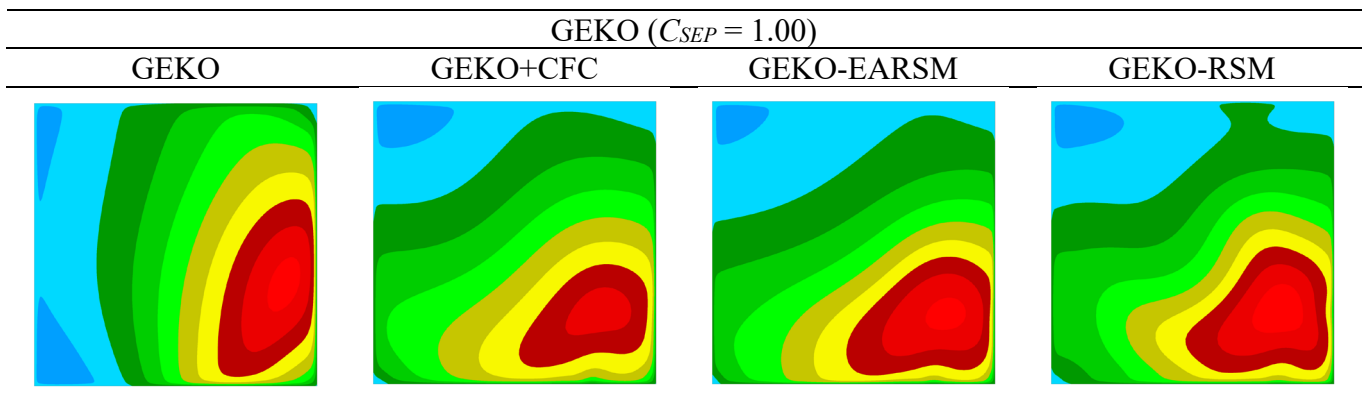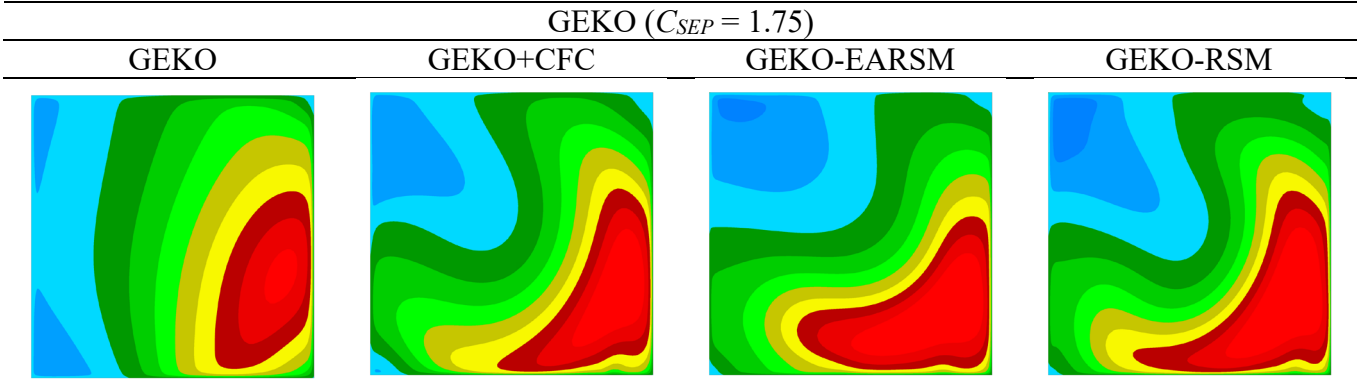| GEKO ($C_{SEP} = 1.75$) | | | |
|---|---|---|---|
| GEKO | GEKO+CFC | GEKO-EARSM | GEKO-RSM |



**Figure 46: Streamwise velocity contours predicted be the linear and non-liner GEKO ($C_{SEP} = 1.75$) model at X5 section. Blue colors indicate recirculation zone.**
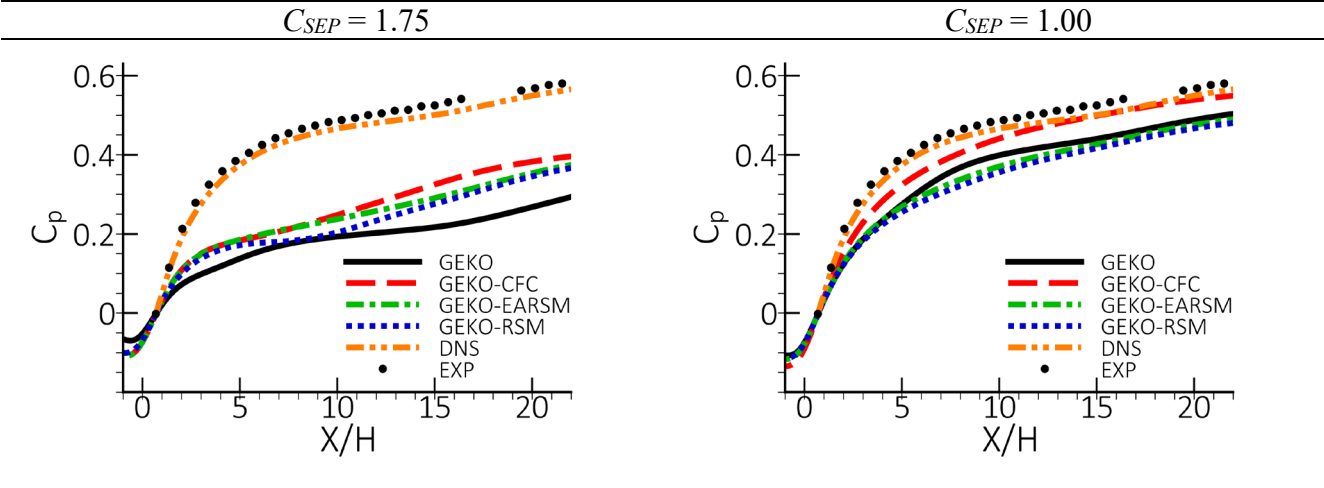


**Figure 47: Distribution of the pressure coefficient along the diffuser at midsection for turbulence models with and without non-linear terms for the Stanford diffuser [42], [43].**

### 4.3.3. Flow around DLR F6 aircraft

Transonic flow past the DLR F6 airplane configuration with mounted engine at a Mach number of $Ma = 0.75$ and $Re = 3 \cdot 10^6$ was considered (Figure 48). The variant for the geometry with mounted engine was selected for comparison, with an angle of attack of 1 degree, providing a lift coefficient of about $C_L = 0.5$. Computations were performed with Ansys CFX® on a block-structured grid of 8.4 million elements.

References to the measurement carried out at ONERA are available from the 2$^{nd}$ AIAA CFD drag prediction workshop (https://aiaa-dpw.larc.nasa.gov/Workshop2/workshop2.html).
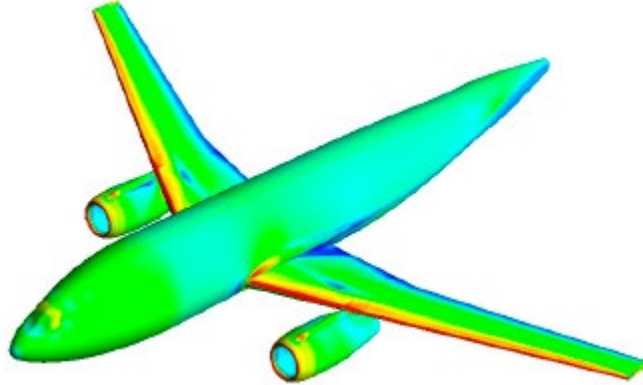


**Figure 48: Geometry DLR F6 Wing-Body-Pylon-Nacelle testcase**

The main challenge in the workshop was to predict the drag differences between a wing-body without and with the engine-nacelle installed. Figure 49 shows the lift-drag polar (different points are for different angles of attack) using the SST model. As can be seen, the data were very well represented in the simulations.
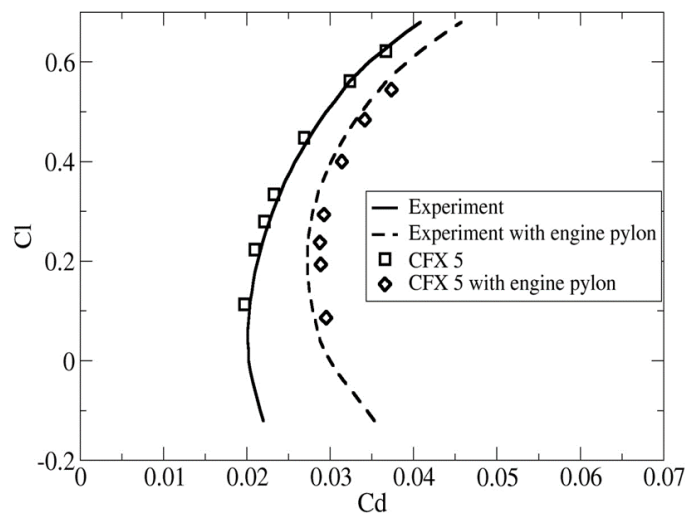


**Figure 49: Lift-Drag Polar for Wing body without and with engine pylon + nacelle**

However, in this section, the interest lies more in the prediction of corners flows and the effect of non-linear models in such areas. The SST model tends to overpredict the size of the corner separation zones, due to the lack of secondary flow prediction capability in corners, as shown in Figure 50. The WJ-BSL-EARSM model improves the result for the wing-fuselage corner separation on the upper wing surface (left set of pictures in Figure 50). The other corner separation zone sits on the lower wing surface where the engine is mounted to the wing. The separation there is also over-predicted by the SST model. With the WJ-BSL-EARSM model, the separation size is substantially diminished in agreement with the experiment.
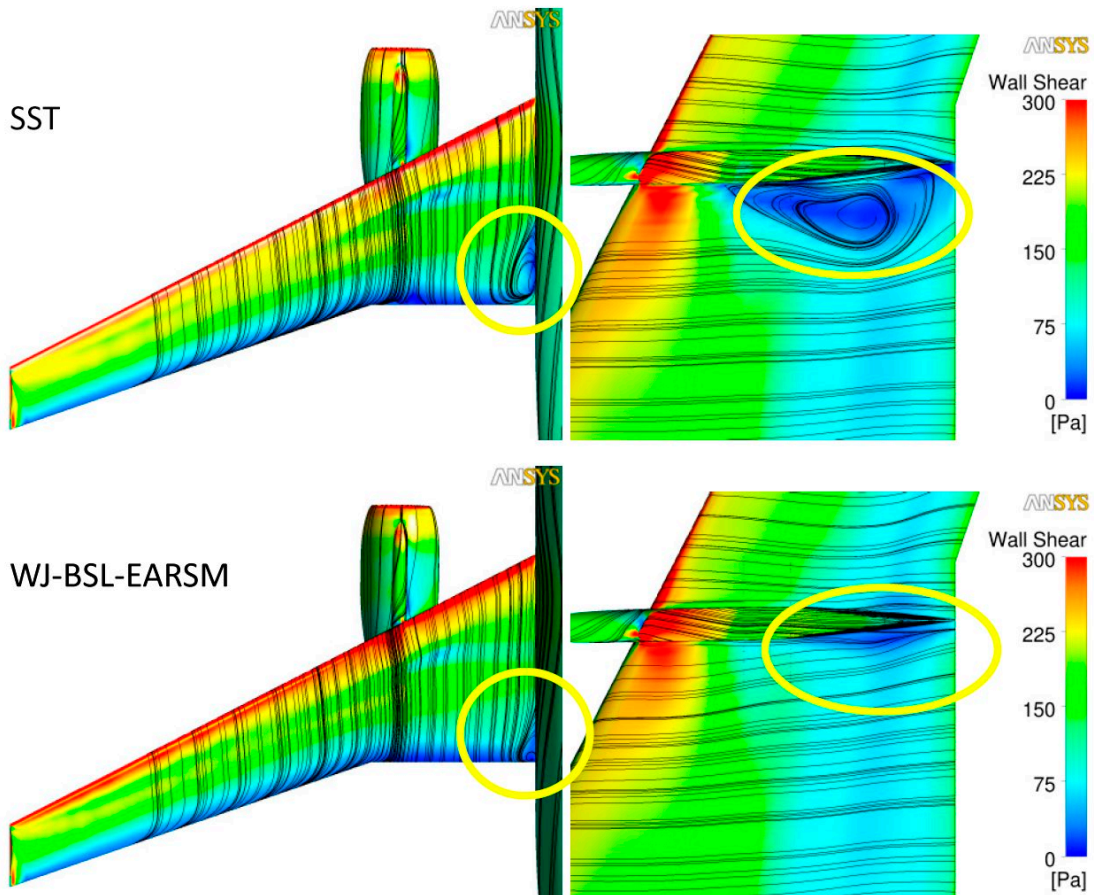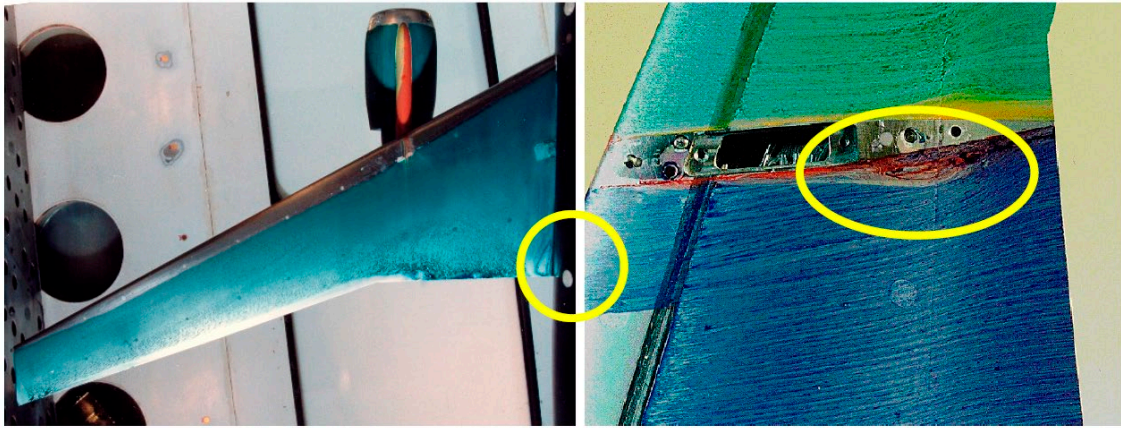
**Figure 50: Separation zone at the upper wing-fuselage junction (left) and lower wing surface behind the engine (right). Top – oil film visualization in the experiment.**

### 4.3.4. Conclusions

Non-linear effects play a significant role for the flows with secondary motions in corners. Linear eddy-viscosity models fail to predict the correct flow topology in the corners. For flows with pressure gradient and separation, this can lead to incorrect predictions of the flow topology. Non-linear models like CFC or EARSM formulations, significantly improve predictions of such flows. The use of the differential Reynolds Stress models does not lead to a significantly further improvement in comparison with the EARSM model.

## 4.4. Swirl Flows

This section shows two examples of the use of the curvature correction (described above in section 3.4.2): flow in a hydro-cyclone and a NACA-0012 wing tip vortex flow. For both cases, the curvature correction is used in combination with the SST model (SST-CC).

### 4.4.1. NACA-0012 Wing Tip Vortex

The NACA 0012 wing tip vortex test case is based on the experiment of Chow et al. [44]. There are several detailed experimental data available at various downstream locations, including velocity fields, pressure, and Reynolds stresses. The 3D wing shown on Figure 51 has a rounded tip and is placed inside a wind tunnel. Due to the lift, the flow from the pressure side travels around the rounded wing tip and rolls up into a strong vortex downstream. The chord-based Reynolds number is $Re_C = 4.6$ million, the Mach number is approximately 0.1 and the angle of attack is $\alpha = 10°$. In the experiment, the flow is tripped at the leading edge and thus considered as fully turbulent.
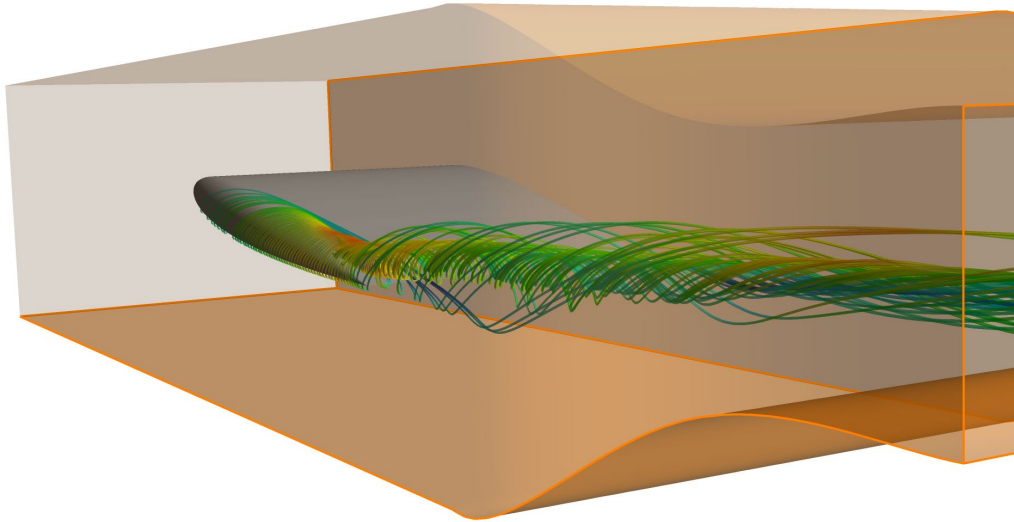


**Figure 51 NACA-0012 wing setup in a wind tunnel showing wing tip vortices as visualized by streamlines.**

The following boundary conditions are adopted for the present simulations. At the inlet section, a total pressure value of $P_{tot} = 1760$ Pa above the atmospheric pressure is specified. Turbulent characteristics at the inlet section are computed from the turbulent intensity value of $Tu = 0.15\%$ and an eddy-to-molecular viscosity ratio equal to $TVR = 5$. A mass flow rate of $\dot{M} = 67.25$ [kg/s] is imposed at the outlet boundary. This results in an area averaged inlet velocity of $U_{inlet} = 51.81$ [m/s] matching the experimental value. The boundary layer on the wind tunnel walls is not considered. Thus, symmetry boundary conditions are specified on the wind tunnel walls for the slip wall imitation and no-slip condition is specified on the NACA-0012 wing.

The mechanism of the curvature correction can be seen through the eddy-viscosity distribution shown in Figure 52 for station $X/C = 0.67$ downstream of the trailing edge. The lower turbulent viscosity in the vortex core region provided by the SST-CC model is a result of the reduction of production of turbulence kinetic energy by the CC modification. This prevents a premature decay of the core axial velocity to a value well below that found in the freestream.
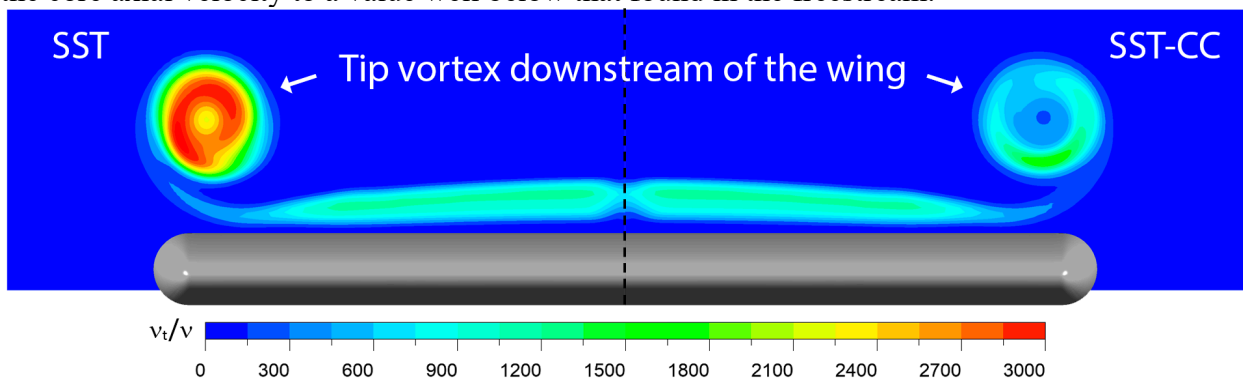


**Figure 52. Front view of eddy-viscosity ratio contours computed with the use of SST and SST-CC turbulence models downstream of the NACA-0012 wing [44].**

The predicted non-dimensional cross flow velocity and axial velocity at three planes located downstream of the trailing edge are shown in Figure 53 in comparison with the experimental data. The coordinate $X/C$ is based on the distance from the trailing edge. One can see that the vortex strength is better captured by the SST-CC model as measured by the maximum of the streamwise velocity. The original SST model decays the vortex too rapidly, as also seen through the axial velocity plots. The SST-CC model shows a significant improvement at the station $X/C = 0.24$ when compared with SST. However, at the far downstream location, $X/C = 0.67$, even the SST-CC model is no longer able to reproduce the experimental velocity profiles, despite the eddy-viscosity being significantly reduced by the correction. There is however also some mismatch in the axial freestream values which points to a potential discrepancy between the experiments and the CFD set-up.

Figure 54 shows the effect of the CC in a contour plot of the axial velocity for a plane going through the vortex core. The increased region of flow acceleration when using the CC extension is clearly visible. It breaks down however just upstream of the $X/C = 0.67$ measurement station.
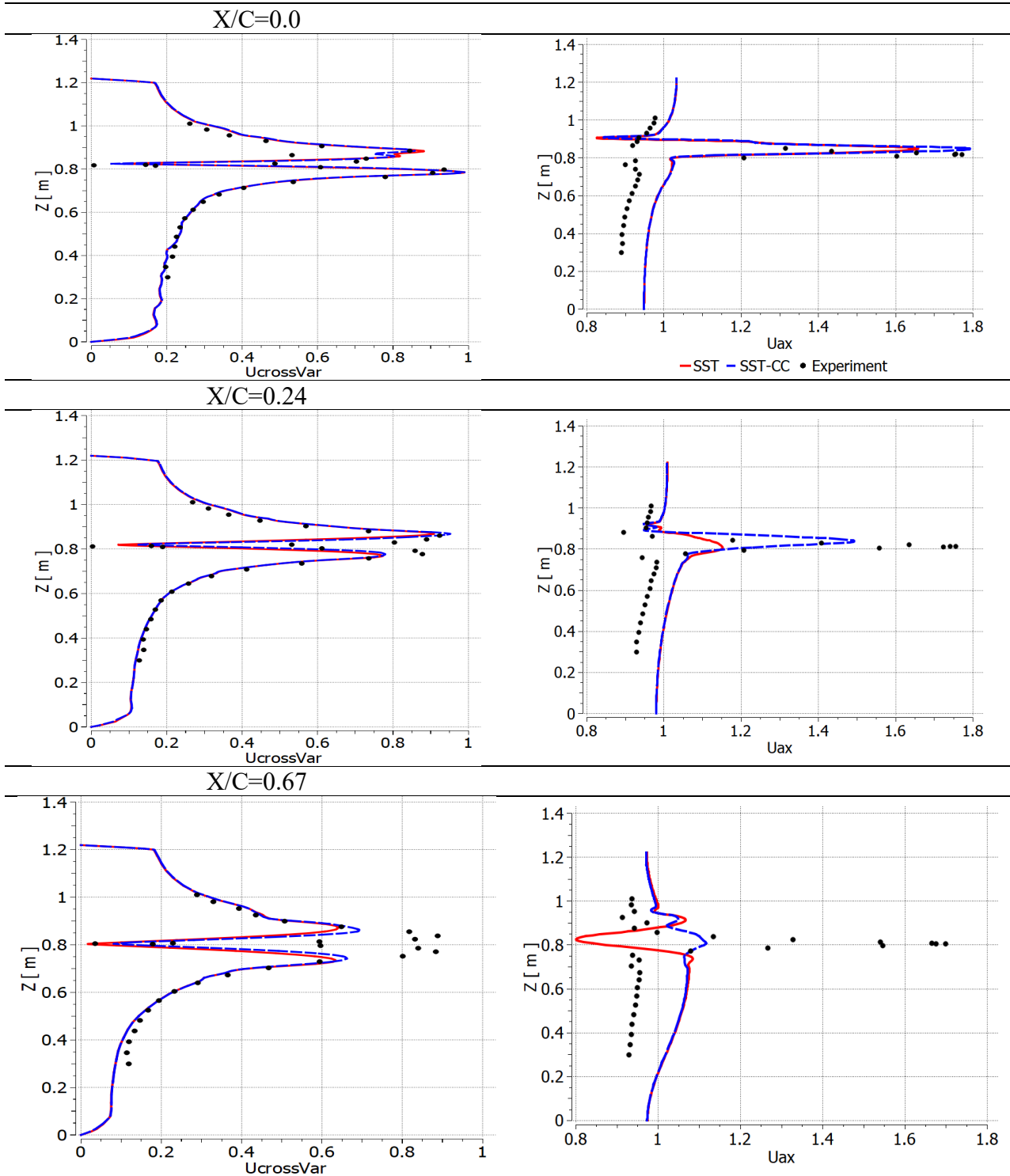
**Figure 53. Non-dimensional cross flow velocity (UcrossVar) and axial velocity (Uax) at three planes located downstream of the trailing edge of the NACA 0012 wing tip [44].**
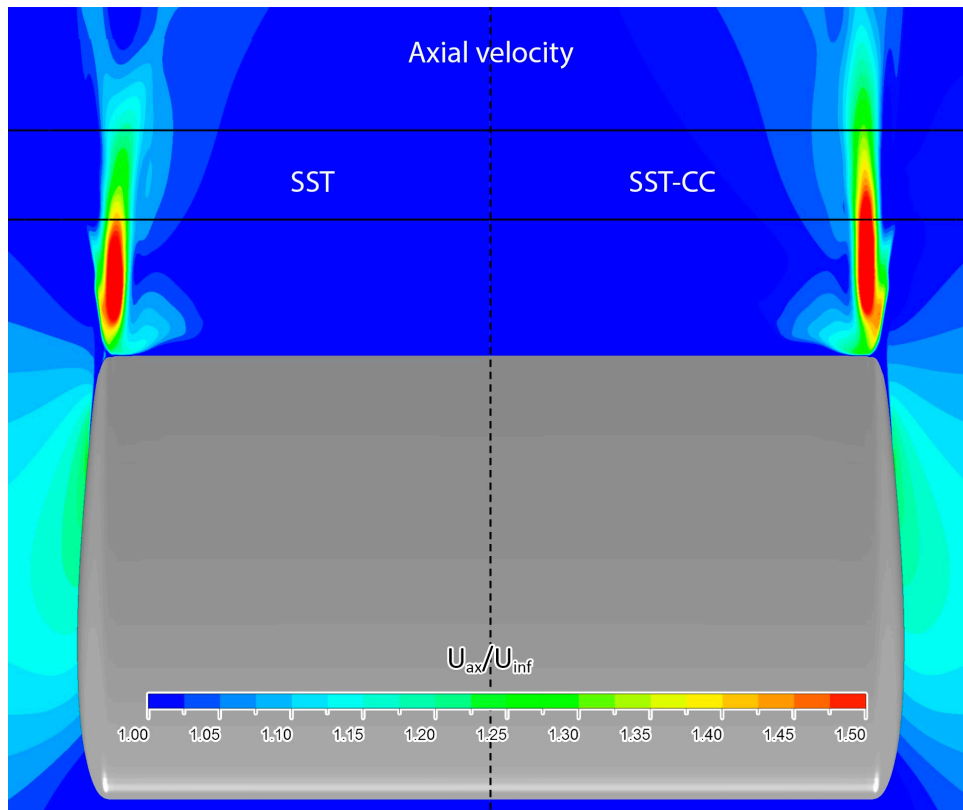
**Figure 54. Computed distributions of the axial velocity at the plane passing through the vortex core for the NACA 0012 wing tip vortex [44].Top view.**

### 4.4.2. Flow in Hydro-Cyclone

The hydro-cyclone's typical flow structure and geometry is shown in Figure 55. The principle behind the cyclone separation is to utilize the strong radial force acting on particles in a strongly swirling flows. The fluid/particle mixture is injected tangentially into the cyclone and spirals downwards in the cyclone barrel (cylindrical section) and then in the cyclone conical section. Under the influence of centrifugal forces, the heavy particles are pushed towards the wall and exit the cyclone due to gravity at the lower exit. The light phase moves towards the cyclone axis, where it joins the upwards flow in a central vortex, leaving the cyclone through the upper outlet. Flow inside a hydro-cyclone is characterized by the formation of a strong vortex core in the central region. To predict such flows accurately, the correct representation of the turbulence is a challenging task for turbulence models.
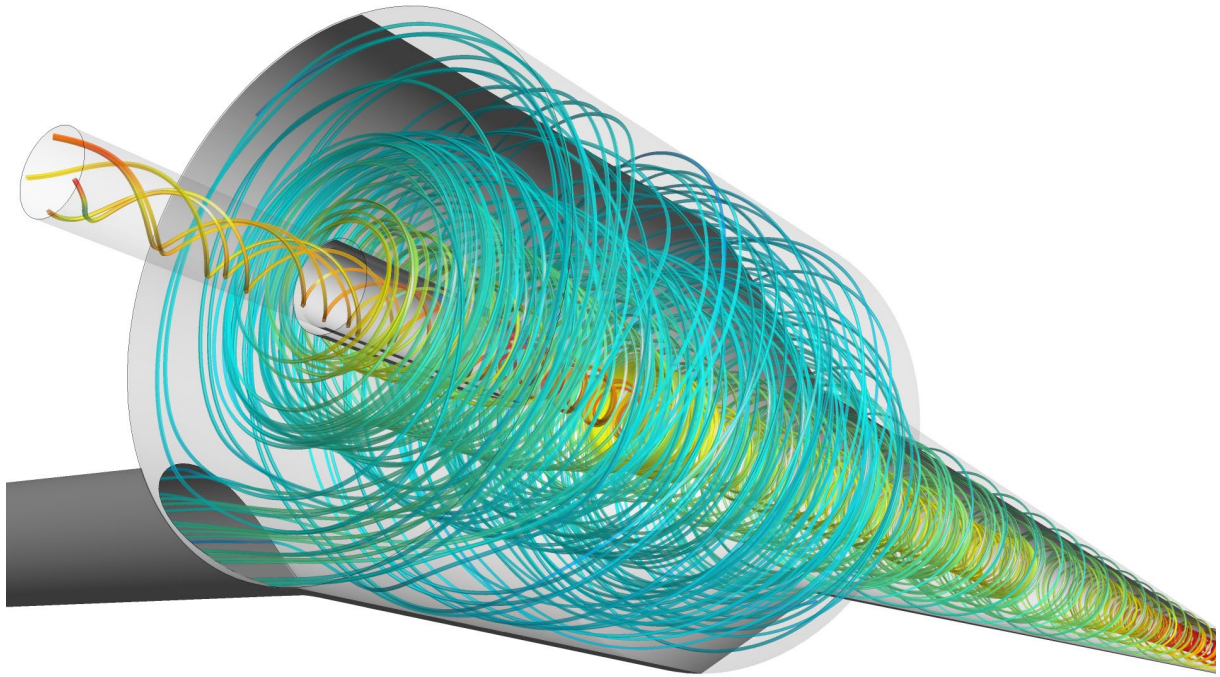
**Figure 55. Flow structure in the hydro-cyclone visualized by the streamlines.**

The current simulations are carried out for the hydro-cyclone investigated experimentally by Hartley [45]. Experimental data of axial and tangential velocities are available at various vertical locations in the cyclone. It is important to note that with a steady-state approach, no physically correct results are obtained, so the case is run in unsteady mode. This is physically correct as it is known that the vortex core is not stable and meanders around the axis of the cyclone.

Figure 57 shows the sensitivity of the simulated tangential velocity to the choice of turbulence model for various z-locations in the hydro-cyclone as indicated in Figure 56. The location z = −20 mm is just below the vortex finder. Here, the typical Rankine-vortex is clearly visible from the experimental data, showing an 'inviscid' vortex at the outer radii and a solid-body rotation close to the axis. The original SST model does not predict the 'inviscid' vortex at large radii, with a tendency towards a solid body rotation everywhere. A substantial improvement can be obtained by applying the curvature correction method for the SST model. The main mechanism of the curvature correction lies in capturing the stabilizing effect of "solid body rotation" near the axis which results in a strong reduction of the turbulence (and therefore eddy-viscosity) in that region. In the comparison there is also the combination of the SST model with the Kato-Launder production limiter (see 9.2.3) included. This modification does influence vortex flows as vorticity and strain rate are no longer equal. However, the effect is small compared with the CC modification.
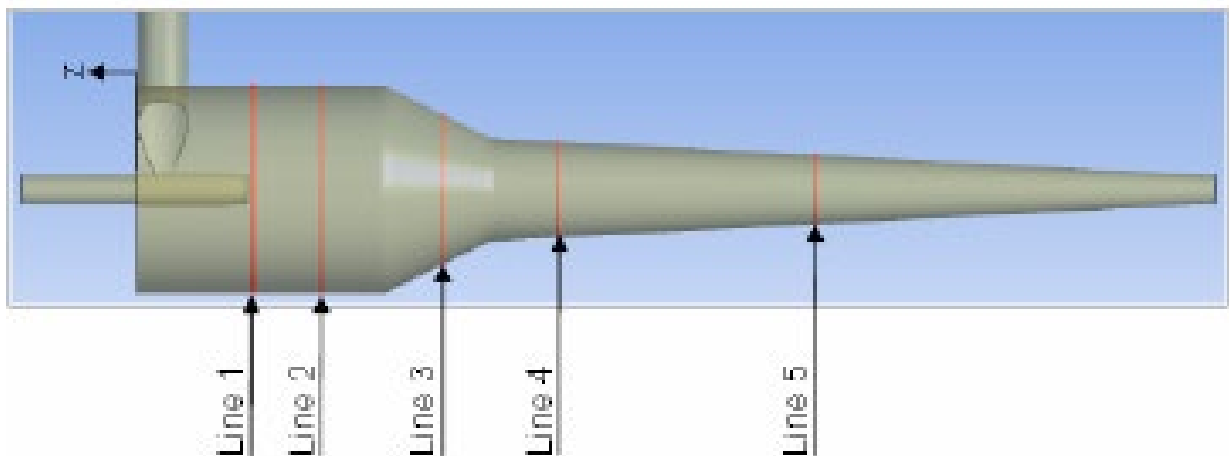


**Figure 56. Measurement planes in the hydro cyclone [45].**

**Tangential velocity profiles, Line 1**
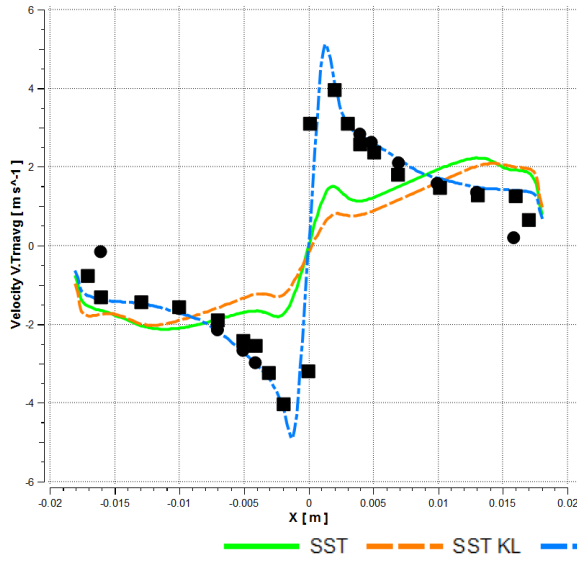
**Tangential velocity profiles, Line 2**
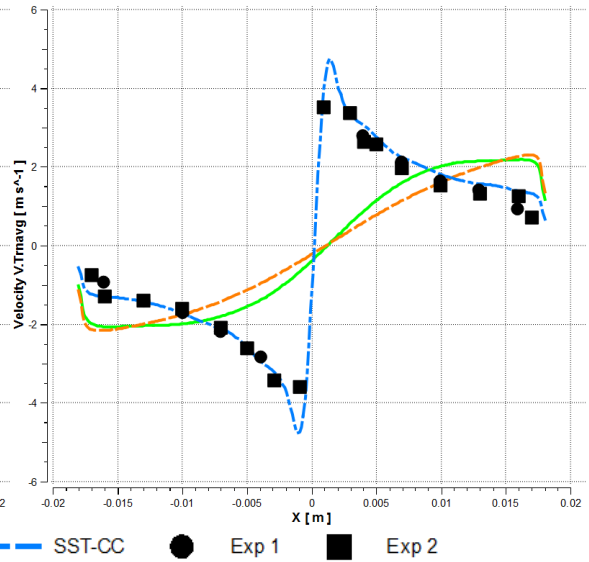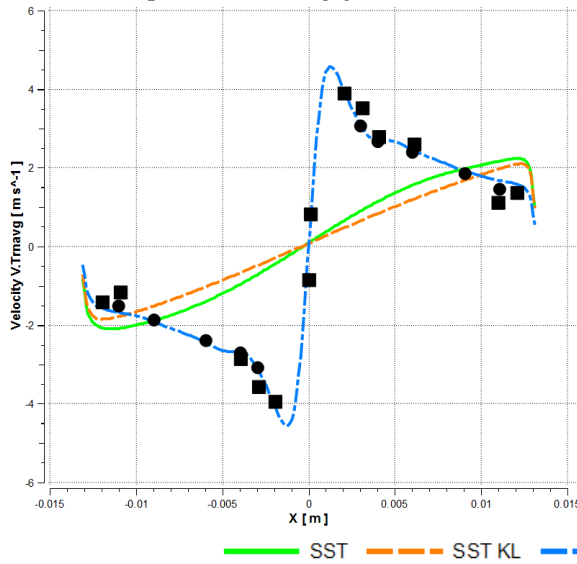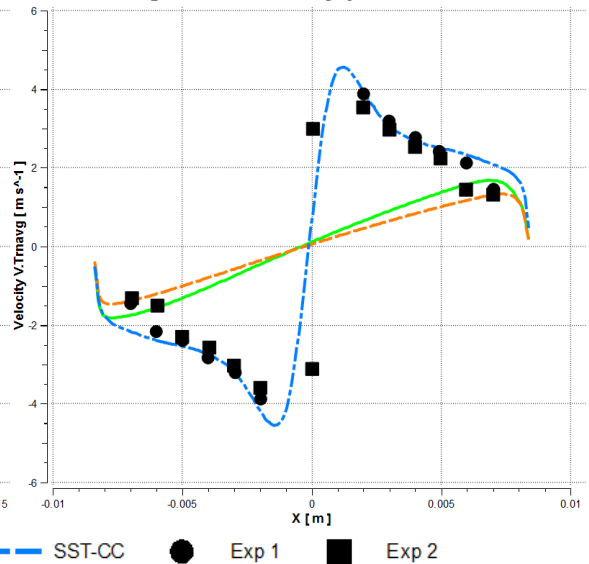
**Tangential velocity profiles, Line 3**
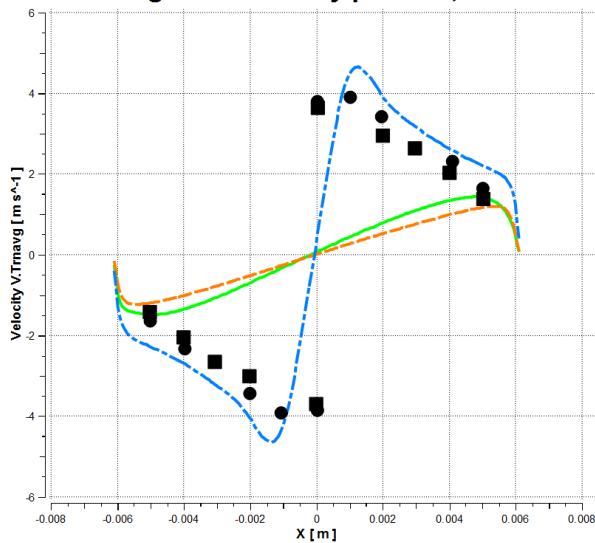
**Tangential velocity profiles, Line 4**

**Tangential velocity profiles, Line 5**

## 4.5. Reattachment Flows

The primary focus of the NASA Hump Flow [46]–[48] (Figure 58) is to assess the ability of turbulence models to predict 2-D separation from a smooth body (caused by an adverse pressure gradient) as well as the subsequent reattachment and boundary layer recovery. Since its introduction, this case has proved to be a challenge for all known RANS models.
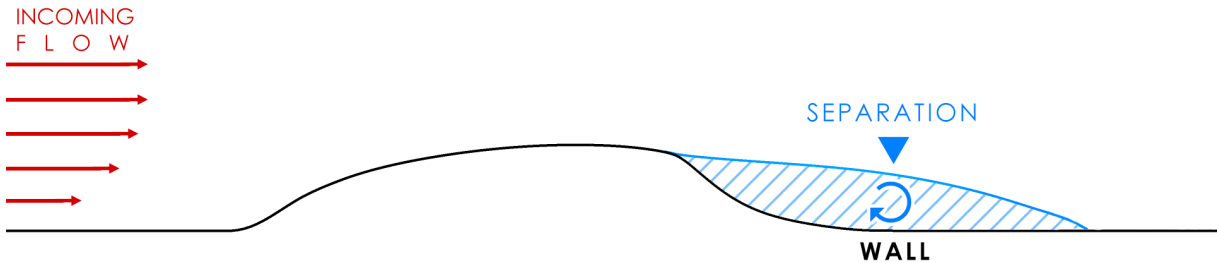


**Figure 58: Schematic of the NASA hump flow.**

Models tend to underpredict the turbulent shear-stress and the turbulence kinetic energy in the separated shear layer, and therefore tend to predict too long a separation bubble. This is an issue with all RANS models and is one the main remaining deficiencies of this model family. It is important to note that the effect is not observed for cases where the separation is fixed by the geometry, like in a backward facing step (see Figure 1). It seems that the difference between these cases lies in a potential unsteadiness of the separation line for the hump flow, which could result in small-scale vortex shedding. Such an effect is in principle outside the realm of RANS models, as it constitutes unsteady flow and not turbulence. Naturally, there is a desire to model such effects within the existing RANS models, as the alternative would be much more expensive Scale-Resolving Simulations. For this reason, different, highly ad-hoc RANS model enhancements have been proposed. They are not used widely and should not generally be activated. However, in some applications, they have shown some improvements and one of the methods is therefore discussed here. The model presented is implemented in Ansys CFX®. The formulation has also been adopted in a NASA TM by Rumsey [49] using different coefficients.

As the SST model typically predicts the onset of separation with good accuracy, there is a need to introduce additional production of turbulence under such conditions. The Reattachment Modification (RM) model introduces the production term $P_{RM}$ into the SST model to enhance turbulence levels in the separating shear layers emanating from walls.

$$P_{RM} = P_k min\left(4max\left(0,\frac{min(S^2,\Omega^2)}{0.09\omega^2} - 1.6\right), 1.5\right)F_{LR}$$

$$F_{LR} = \tanh\left(\left(\frac{k}{10\omega\nu}\right)^2\right)$$

(4.1)

The motivation for this formulation is that in the separating shear layer, the ratio $\frac{min(S^2,\Omega^2)}{0.09\omega^2}$ increases significantly beyond one, which can then be used as an indicator to trigger the additional production term. Unfortunately, the reattachment modification is very sensitive to the combination of the computational mesh resolution and numerics for the turbulence equations. Three meshes, as shown in Figure 59, have been tested, with Mesh-1 being the finest and Mesh-3 the coarsest. Figure 60 shows the effect of the RM on the solution, as a function of mesh and discretization. The RM improves the prediction of the reattachment point only on the coarse meshes (Mesh-3) for the first

order upwind scheme. The results of the original SST model and the SST-RM model using 2$^{nd}$ order numerics are virtually the same for all the meshes. The efficiency of the model can be improved by reducing the limiter of 1.6 in the equation, but this can have the effect that the modification will affect generic flows, especially turbulent mixing layers. The spreading rate of mixing layers would then be over-predicted. The NASA version of the model effectively reduces the limiter from 1.6 → 1.25 resulting in a more active model, but at the price of affecting generic flows.
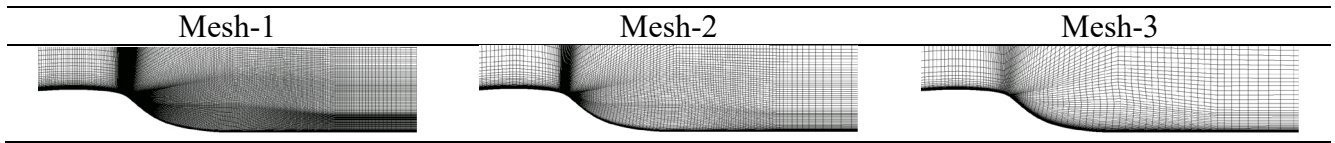


**Figure 59: Computational meshes for the Hump flow.**
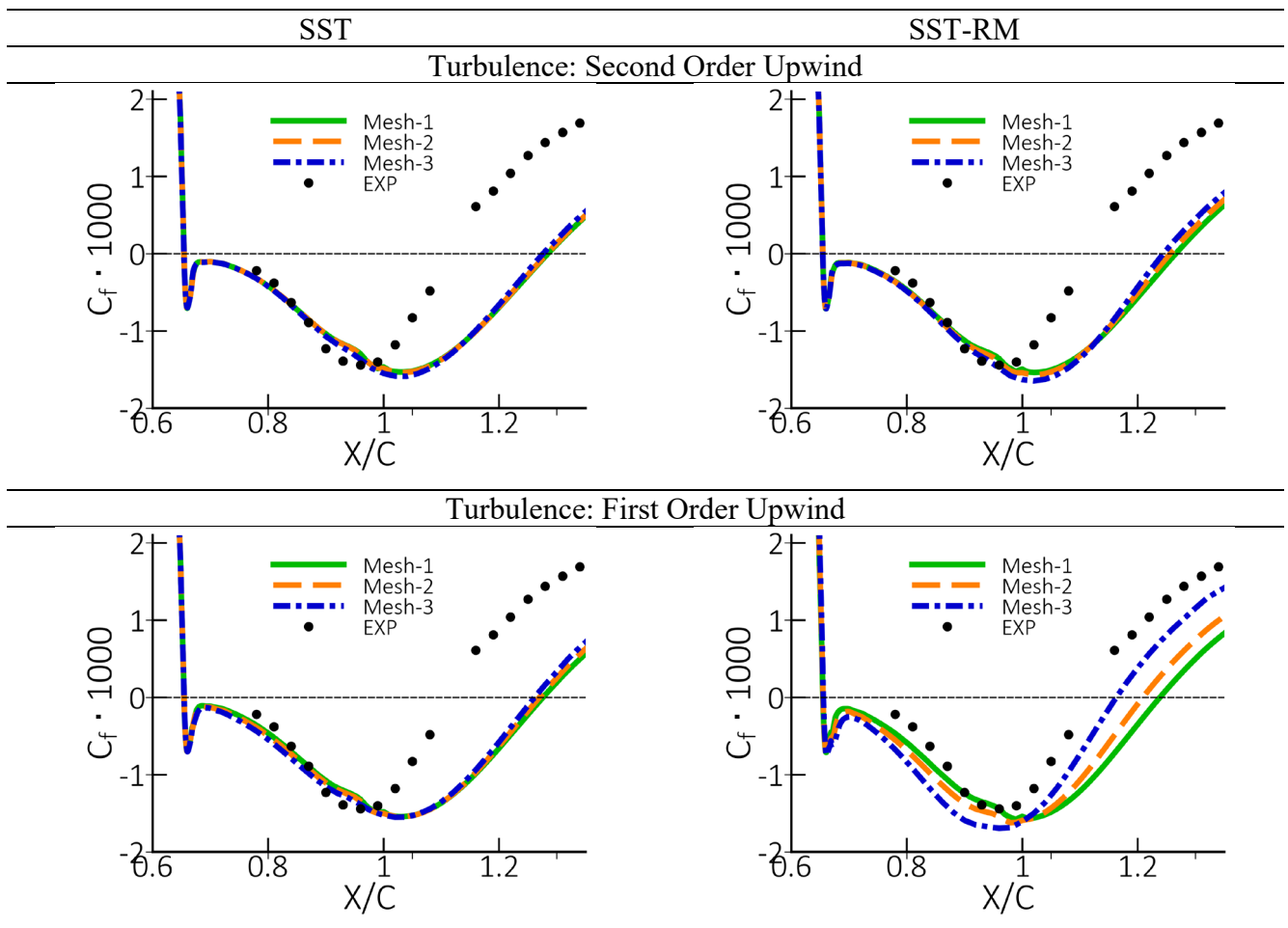


**Figure 60: Comparison of wall shear stress coefficient for NASA Hump flow.**

An improvement of the reattachment prediction can also be achieved with the turning of the GEKO model. Figure 61 shows the effect of the decrease of the $C_{SEP}$ coefficient on the prediction of the reattachment point. The prediction of the velocity and Reynolds stresses are also improved for the $C_{SEP} = 1.00$ value (Figure 62) albeit at the expense of delayed separation onset prediction. However, the Reynolds normal stresses $\overline{u'u'}$ are still underpredicted in the separation region and virtually independent of the $C_{SEP}$ value which is shown in Figure 63.
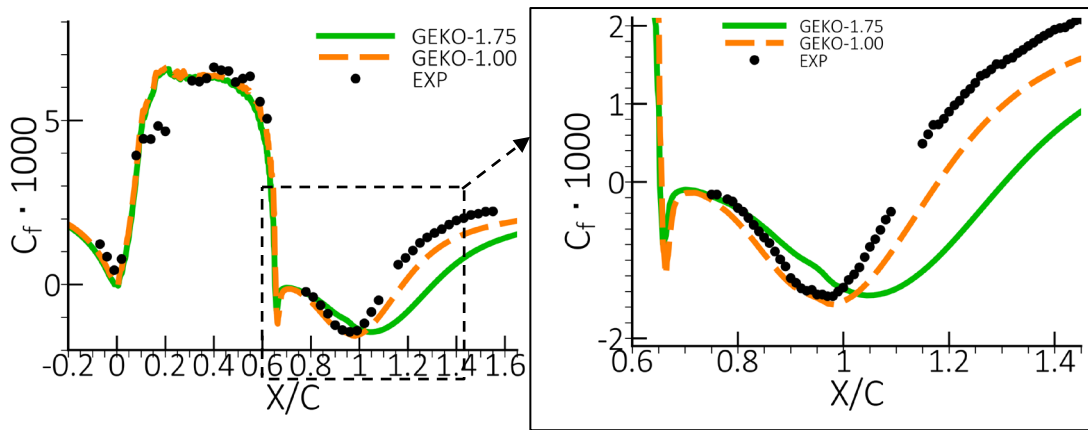
**Figure 61: Comparison of wall shear stress coefficient predicted with GEKO model for NASA Hump flow [48].**
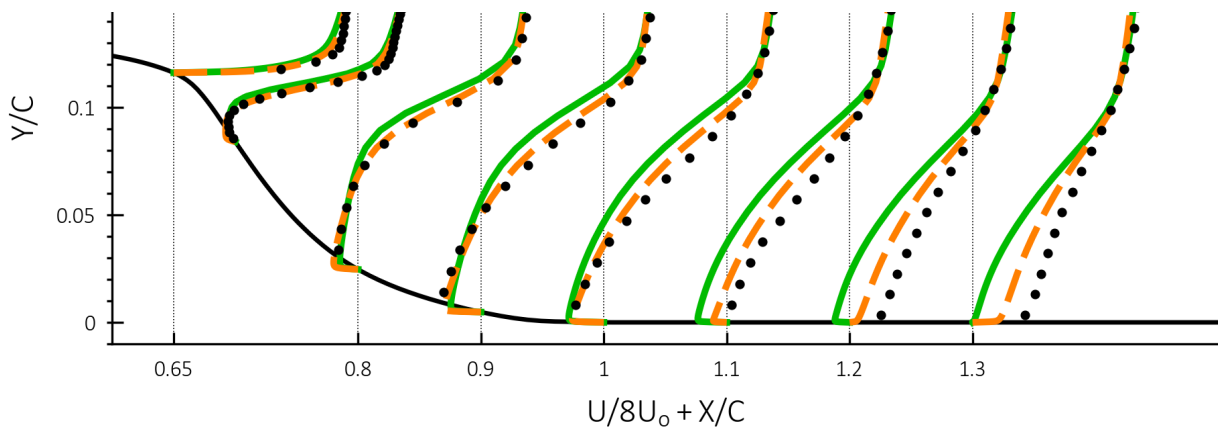


**Figure 62: Effect of the GEKO CSEP on the streamwise velocity for NASA Hump flow [46], [47].**
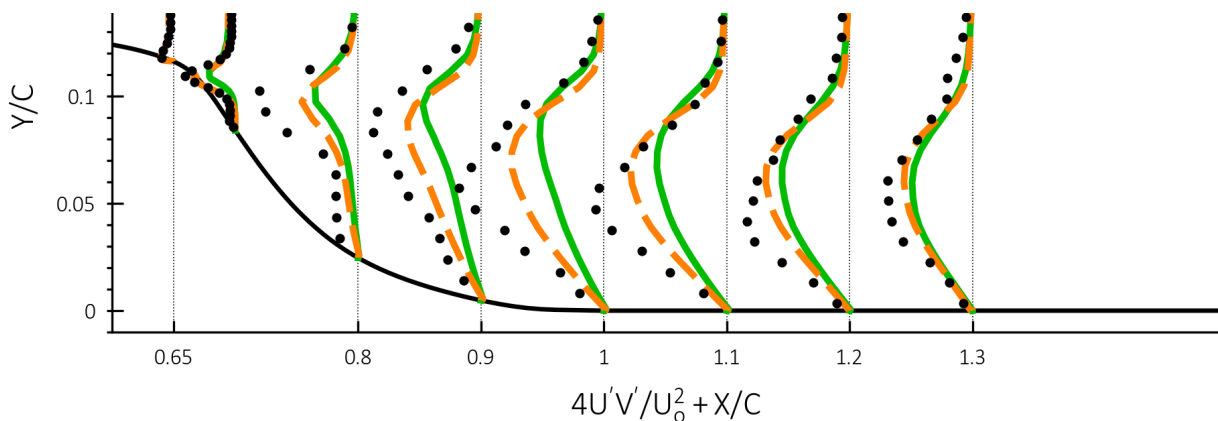


**Figure 63: Effect of the GEKO CSEP on the Reynolds shear stresses for NASA Hump flow [46], [47].**

Again, it needs to be stressed that the change to $C_{SEP}$=1.00 is not considered a model for the true physics of these flows, but can help in practical applications to obtain better agreement with the data.

## 4.6. Impinging Flows

Impinging jets are a very effective way to enhance surface heat transfer and are frequently employed in industrial devices (impingement cooling). The considered test case is based on the experiments carried out by Baughn et al. [50]. The flow being modeled is the incompressible flow of a turbulent jet impinging onto a flat plate. Figure 64 shows the geometry of the flow domain. The

size of the computational domain in the plane is 13D×13D, where D = 0.0265 m is the diameter of the pipe.
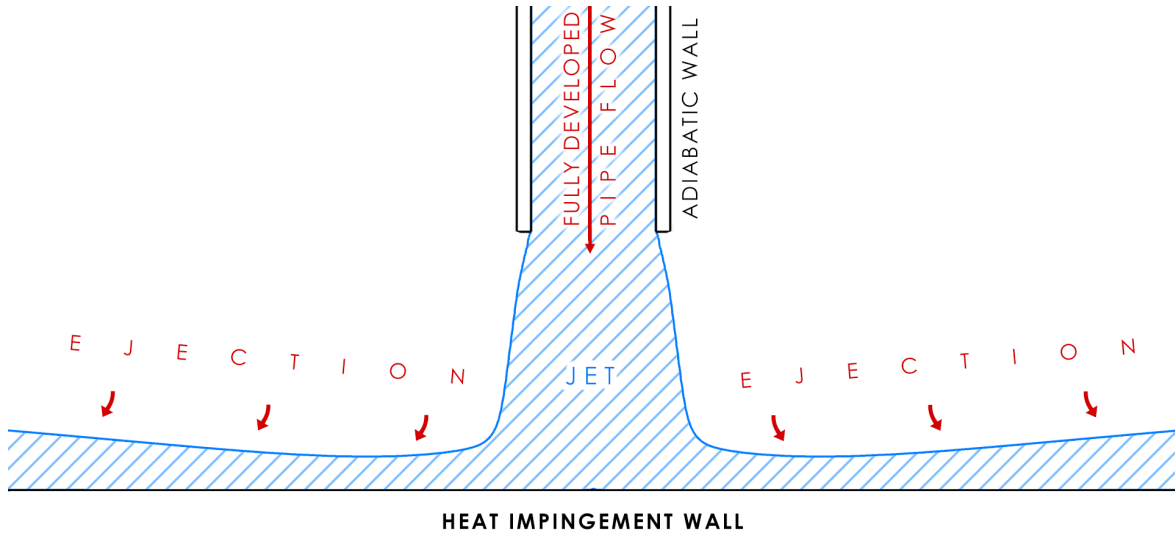


**Figure 64: Scheme of the impinging jet flow.**

The computational domain with boundary conditions is shown in Figure 65. The inflow conditions for velocity and turbulence are specified using profiles for fully developed turbulent flow through a pipe, which are calculated in separate simulations. The Reynolds number based on the bulk inlet velocity, $U_{bulk}$ = 15.45 [m/s], and pipe diameter is Re = 2.3·10⁴. The heated surface is modeled as a wall with a specified constant heat flux, $q$ = 300 W/m². All other walls are treated as adiabatic walls. An auxiliary inlet boundary condition is employed to allow for entrainment of fluid from outside. Zero gauge total pressure along with the inflow direction is assumed on this segment. The right boundary is modeled as a modified outlet boundary which changes to an inlet with 10 degrees flow direction to the boundary, in case fluid enters the domain. This treatment avoids massive flow entrainment at that boundary.
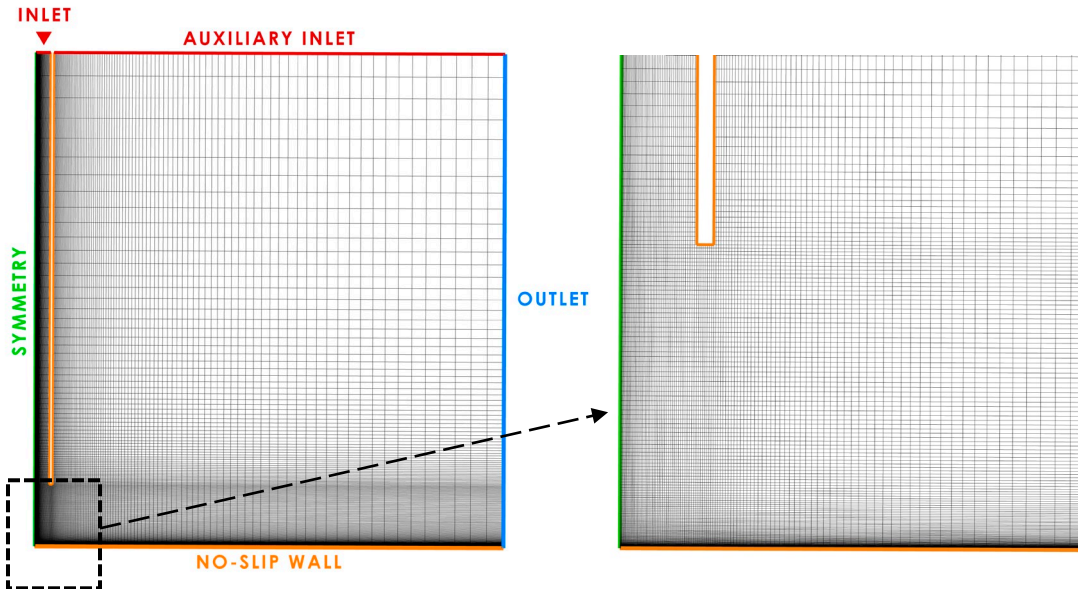


**Figure 65: Computational domain with boundary conditions and mesh for the impinging jet.**

Figure 66 (left) compares the predicted Nusselt number distributions for different turbulence models. The $k$-$\varepsilon$ and SA models underestimate Nu over almost the entire length of the heated wall, while the SST model gives a reasonable agreement downstream from $r/D$ = 1.5. However, all the models fail in predicting the dip in the Nu number at $r/D$ < 1.5. To investigate this further, a simulation is performed, where the SST model is combined with the $\gamma$-transition model [36]. Figure

66 (right) demonstrates that the inclusion of the laminar-turbulent transition phenomena is essential in predicting the local minima. It coincides with the location of laminar-turbulent transition of the boundary layer developing on the impingement wall, which is triggered by the shear layer from the outer boundary of the impinging jet. Note that in case of the transition computations, the computational mesh (see Figure 67) was refined in the radial direction ($r/D < 1.5$) for the proper resolution of the laminar-turbulent transition zone (this refinement had no effect on the fully turbulent simulations).
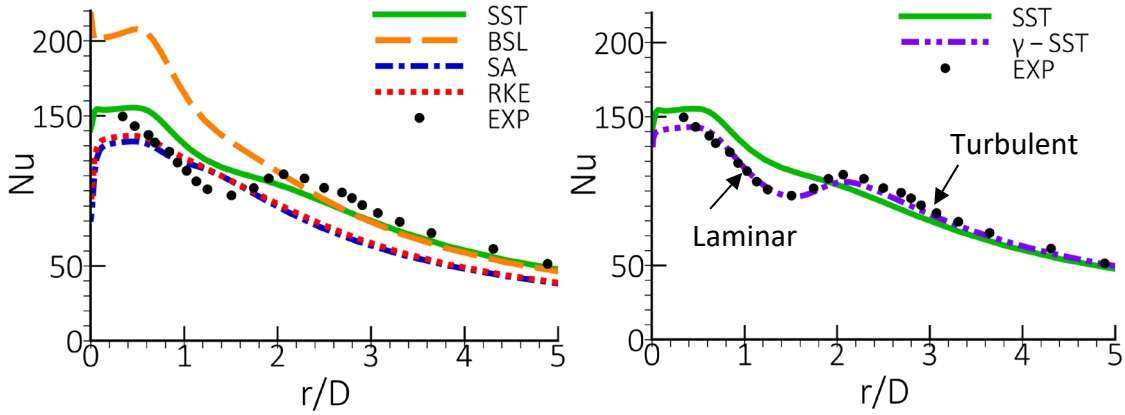


**Figure 66: Local Nusselt number computed using different turbulence models (left) and SST model with and without taking into account the laminar turbulent transition (right).**
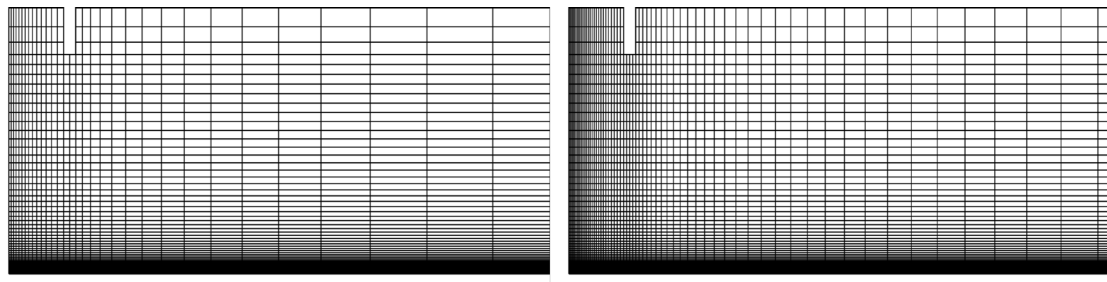


**Figure 67: Computational mesh for the fully turbulent regime (left) and regime with taking into account laminar-turbulent transition (Right).**

## 4.7. Buoyancy Flows

### 4.7.1. Stratified Mixing Layer

A stably-stratified mixing layer flow between fresh water and a saline stream was experimentally investigated by Uittenbogaard [51] at the Delft Hydraulics laboratory. Their installation is sketched in Figure 68. Two flows with different densities enter the domain horizontally separated by a splitter plate. The upper flow is a fresh water stream with a density of 1015 [kg/m$^3$] and an average velocity of 0.52 [m/s]. The lower current is a salt water solution with density of 1030 [kg/m$^3$] and an average velocity of 0.32 [m/s]. The flow can be considered two dimensional in the CFD setup as shown in Figure 68. The flow properties are presented in Table 3.
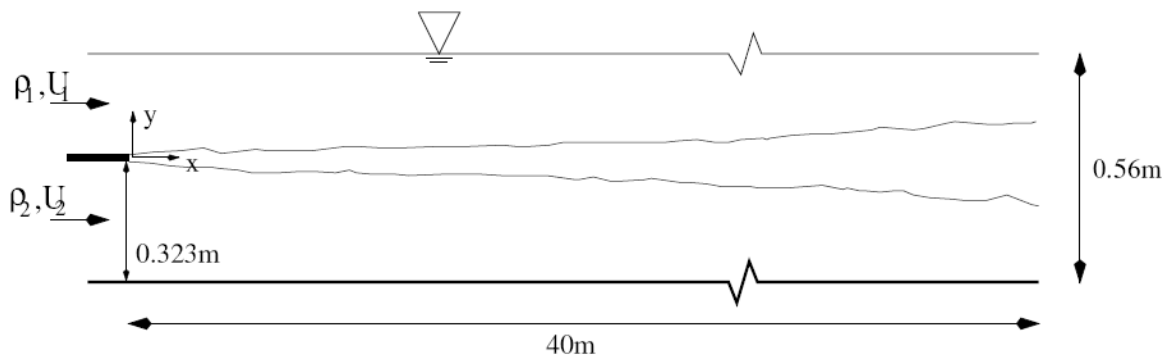
**Figure 68: Scheme of the stratified mixing layer.**

**Table 3. Flow parameters of the stratified mixing layer**

| $\rho_{fresh}$, kg/m³ | $\rho_{salt}$, kg/m³ | $\mu$, Pa s | Thermal Conductivity, W/(m K) | Mass Diffusivity, m²/s | Specific Heat, J/(kg K) | Molecular Weight, kg/kmol |
|---|---|---|---|---|---|---|
| 1015 | 1030 | $8.899\times10^{-4}$ | 0.6069 | $10^{-9}$ | 4182 | 18.0152 |

The computational domain with boundary conditions is shown in Figure 69. The length and height of domain are 40 [m] and 0.56 [m] corresponding to the experimental test section. At the inlet boundary, the thicknesses of the fresh and salt water layers are 0.237 and 0.323 [m] respectively.

Computations are carried out with Standard $k$-$\varepsilon$ model and SST and GEKO models without and with buoyancy corrections. For all the cases, the boundary conditions are as follows. At the inlet boundary, the experimental velocity profiles, turbulence characteristics and component concentration are specified. Constant pressure is specified on the outlet boundary. The lower boundary is modeled as a non-slip wall and upper boundary of the flow is a free surface.
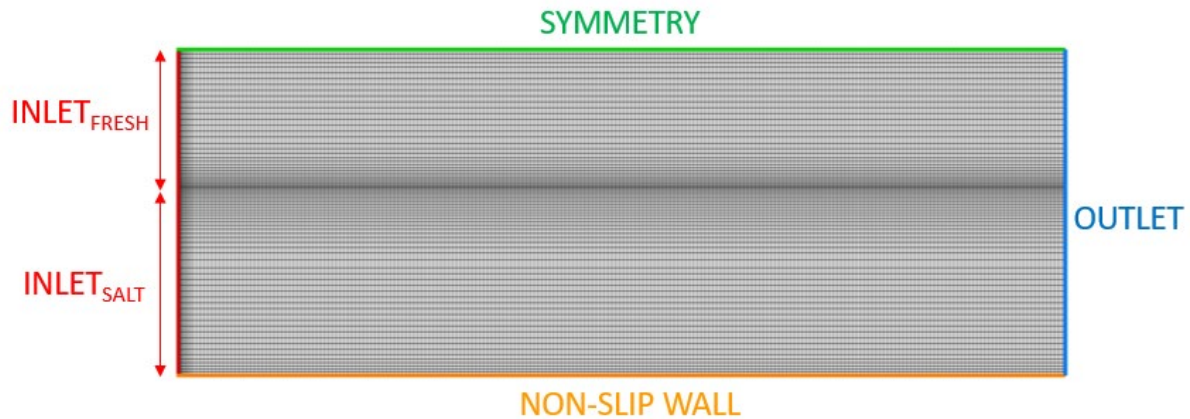


**Figure 69: Computational domain with boundary conditions and mesh for the stratified mixing layer.**

Figure 70 shows comparison of the density and velocity profiles at three different sections for the SST model without and with buoyancy correction (SST-BC). $X = 5$ [m] is the section near the inlet boundary and $X = 40$ m corresponds to the outlet location. The non-dimensional density variable computes as $\frac{\rho}{\rho_{ref}} = \frac{\rho - \rho_{fresh}}{\rho_{salt} - \rho_{fresh}}$. It is evident from Figure 71 that without considering buoyancy effects the stabilizing effect of the density stratification is not felt and the rate of mixing of the two fields is excessive. The buoyancy production term in the k-equation reduces the turbulence kinetic energy generated in the shear layer, as shown in Figure 72. This leads to a reduction of the eddy viscosity and the Reynolds shear stresses. As a result, the mixing layer develops in better agreement with the experiment. The station furthest downstream at $X = 40$ m indicates that the buoyancy correction imposes too strong a damping effect on turbulence as seen by the lack of mixing in both the density and the velocity profiles. Default settings were used, and no effort was undertaken to fine-tune the model.

| $X = 5$ [m] | X = 10 [m] | X = 40 [m] |
|---|---|---|
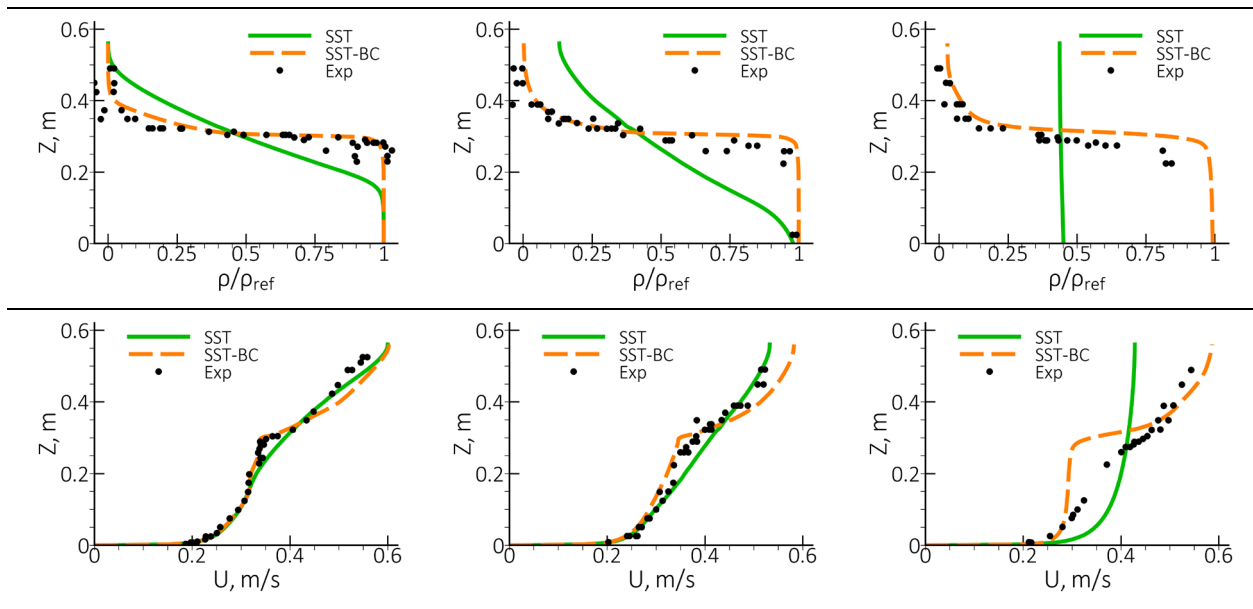
**Figure 70: Density and streamwise velocity profiles at different sections for the stratified mixing layer.**
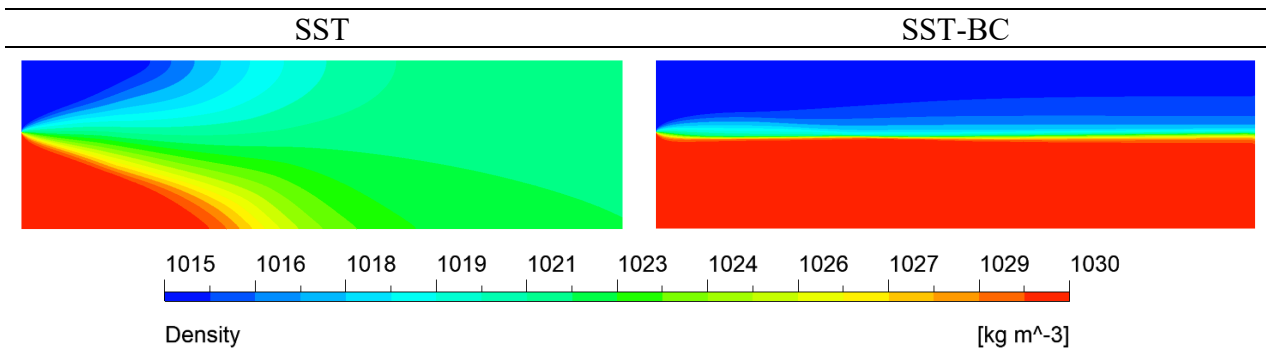


**Figure 71: Density field for the SST (Left) and SST-BC (Right) model.**
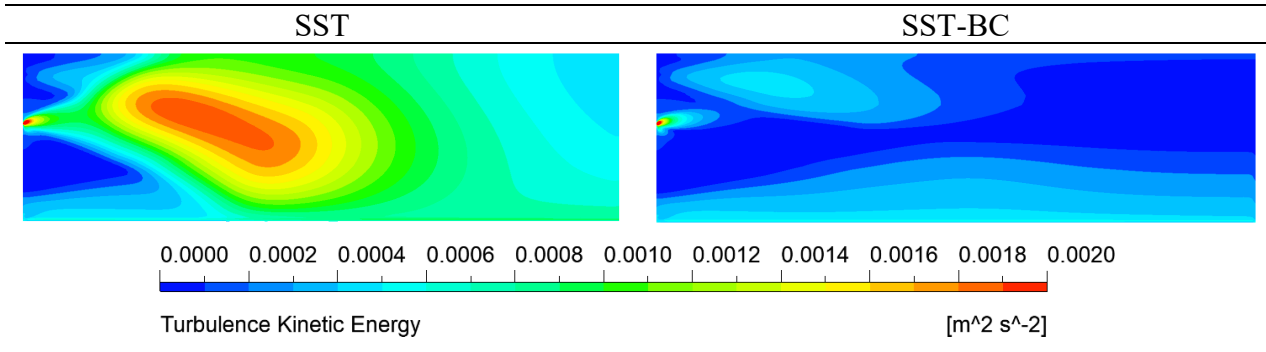


**Figure 72: Turbulence kinetic energy field for the SST (Left) and SST-BC (Right) model.**

The comparison of different turbulence models shown in Figure 73 demonstrates that the sensitivity to the turbulence model is negligible and much smaller than the buoyancy effects. Due to similar results for different sections only those for $X = 10$ [m] are shown.
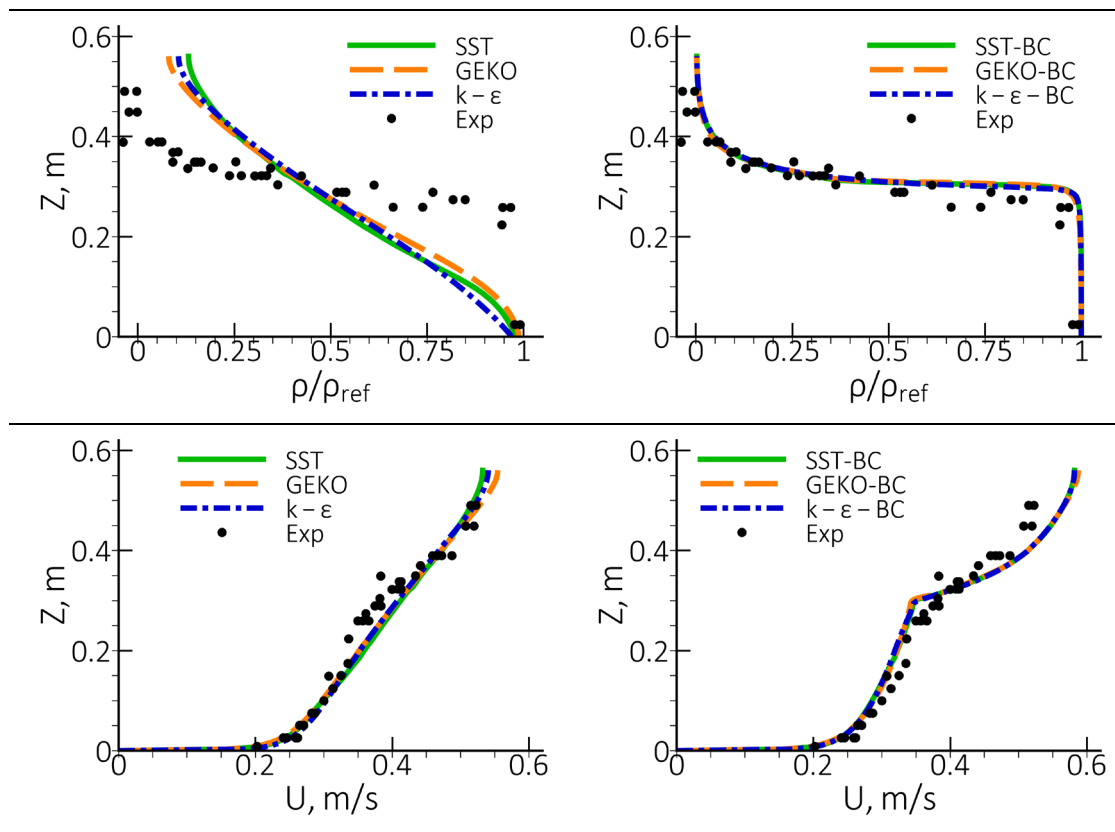
**Figure 73: Density (upper row) and streamwise velocity (lower row) profiles for different models for the stratified mixing layer at *X* = 10 [m] section.**

## 4.8. Effect of Limiters

As mentioned in section 3.3.5 the use of limiters in the formulation of the eddy-viscosity or the production term prevents the formation of unphysically high turbulence kinetic energy levels and, therefore, high eddy-viscosity levels near stagnation regions. It should be noted that the unphysical build-up of turbulence does not only occur in stagnation regions, but in any other region with non-zero shear strain rate, $S$, outside shear layers (e.g. also in accelerating inviscid flow).

Detailed descriptions of the limiters are given in Section 9.2.3. This section demonstrates the effect of realizability limiters, the production limiter and the Kato-Launder limiter for different turbulence models for flow around a NACA-4412 airfoil at $\alpha = 14^\circ$. Note that RKE model features an internal realizability limiter which cannot be turned off. This limiter is not the same as the realizability limiter used in the GEKO model. As shown below, it is also not as effective as the GEKO limiter.

For all the Figures the following notations are used:

- $Real_{lim}$ – Realizibility limiter (Eq (9.34))
- $Pk_{lim}$ – Production term limiter (Eq (9.53))
- $Pk_{,KL}$ – Kauto-Launder production term formulation (Eq (9.52)).

As seen in Figure 74, Figure 75 and Figure 76, all the considered limiters avoid the eddy-viscosity and turbulence kinetic energy build-up in the stagnation regions of a NACA 4412 airfoil. For the GEKO model, the default $Real_{lim}$ has the same effect as other limiters. The effect of the production limiter is strongest for the *k-ε* Standard model. On the other hand, the in-built realizability limiter of the *k-ε* RKE model improves the solution in the stagnation region, however, the model still predicts high eddy-viscosities outside the boundary layer. Again, the use of the $P_{k,lim}$ fixes this issue.

In case of laminar-turbulent transition modeling, the effectiveness of limiters is very important, as even small turbulence build-up can affect the transition onset location. Typically, a strong combination of limiters is used (Pk limiter and Kato-Launder for the SST model).
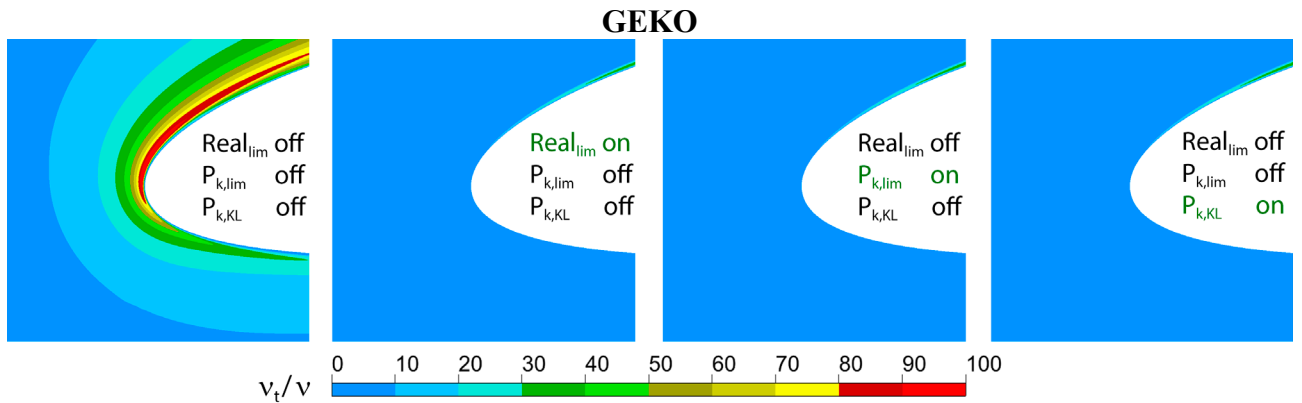
**GEKO**

Figure 74: Effect of limiters for the GEKO model near the stagnation point for flow around airfoils.
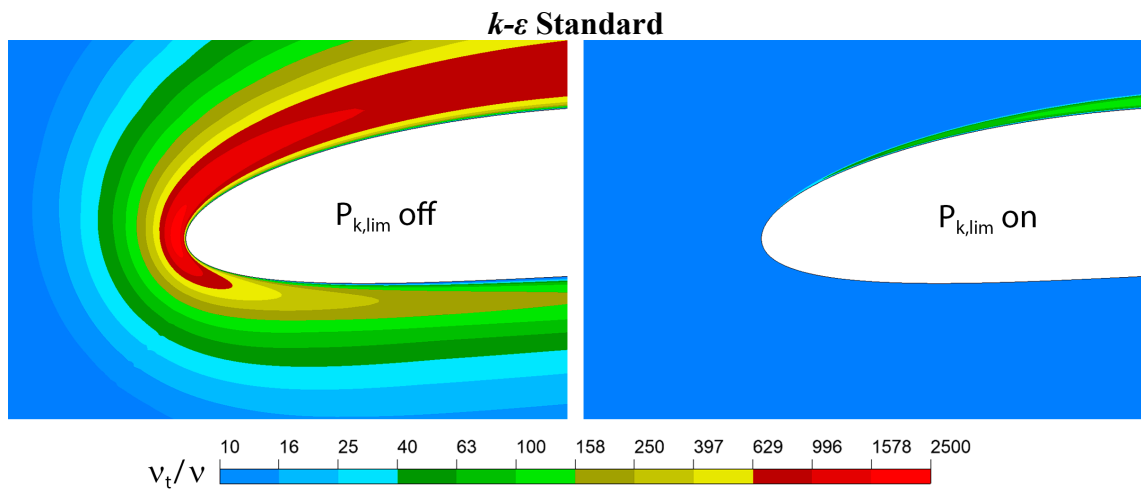
**$k$-$\varepsilon$ Standard**

Figure 75: Effect of production limiter for the $k$-$\varepsilon$ Standard model near the stagnation point for flow around airfoils.

**$k$-$\varepsilon$ RKE**
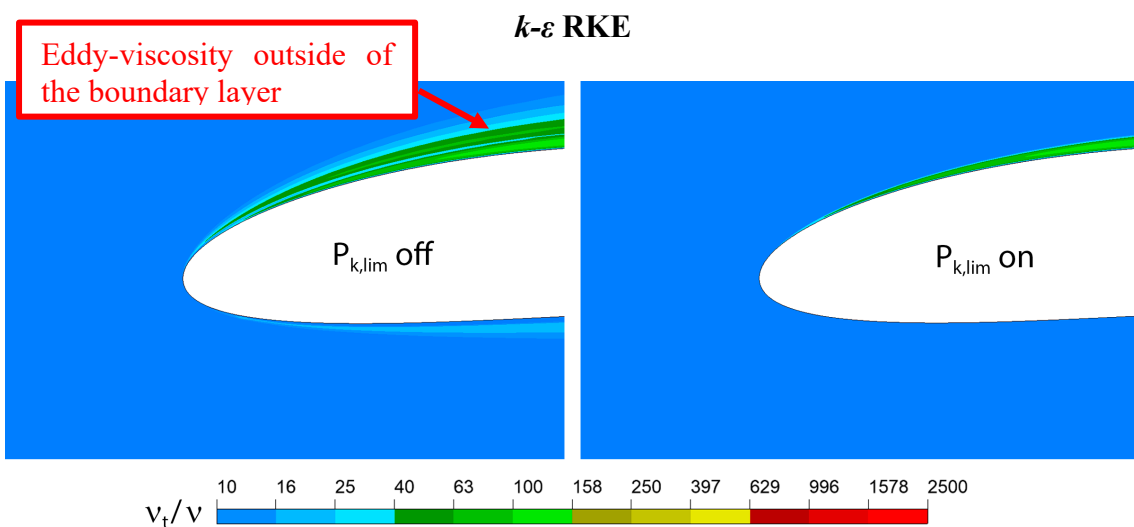
Figure 76: Eddy-viscosity field predicted with the RKE turbulence model near the stagnation region for flow around airfoils

## 4.9. **Mesh Resolution Requirements**

Mesh resolution and mesh quality are key elements for a successful CFD simulation. There are several nested requirements for mesh resolution:

### 4.9.1. Inviscid Flow

The most basic requirement is that the grid must be able to resolve the inviscid parts of the flow. This means that regions of flow acceleration/deceleration as well as streamline curvature etc. must be properly resolved. This also includes the resolution of strong gradients, especially shocks. Inviscid flow resolution is typically of importance in regions of geometrical changes (corners, edges, trailing edges, leading edge suction peaks, inviscid vortex flows, ….). Insufficient mesh resolution in this context is typically noticeable through changes in pressure distribution under mesh refinement.

### 4.9.2. Free Shear Flows

Free shear flows, like mixing layers, jets or wakes typically require at least ~10 cells normal to the layer. The resolution in stream/spanwise direction is usually of the order of the shear layer thickness.

There are two main challenges with free shear layers. The first is that they can be very thin at their origin. It is therefore hard to capture the initial formation of such layers – in most cases they are therefore under-resolved. The second challenge is that their location is often not known before the simulation. One should therefore investigate the solutions and refine the meshes if important shear layers have been missed or under-resolved by the mesh. Alternatively, the layers can be targeted by mesh adaptation using adaptation criteria indicative of the layer (gradients of velocity or turbulence kinetic energy etc.).

Figure 77 shows examples of coarse, medium and fine meshes which correspondingly have ~ 5/10/20 cells across the mixing layer. For all the meshes the streamwise resolution is identical. The coarse mesh does not provide a grid-independent solution, while results on the medium and fine meshes are in perfect agreement. This is shown on Figure 78 where self-similar profiles of the streamwise velocity component, turbulence kinetic energy and Reynolds shear stress are plotted for the SST model.
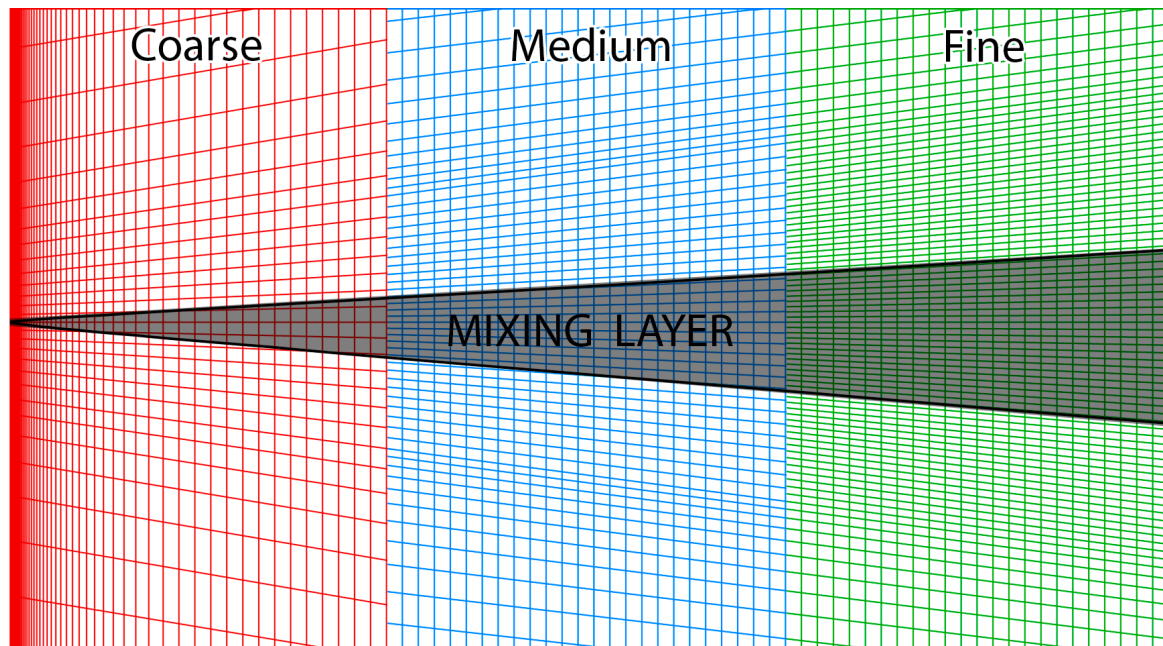


**Figure 77: Computational meshes for the mixing layer.**
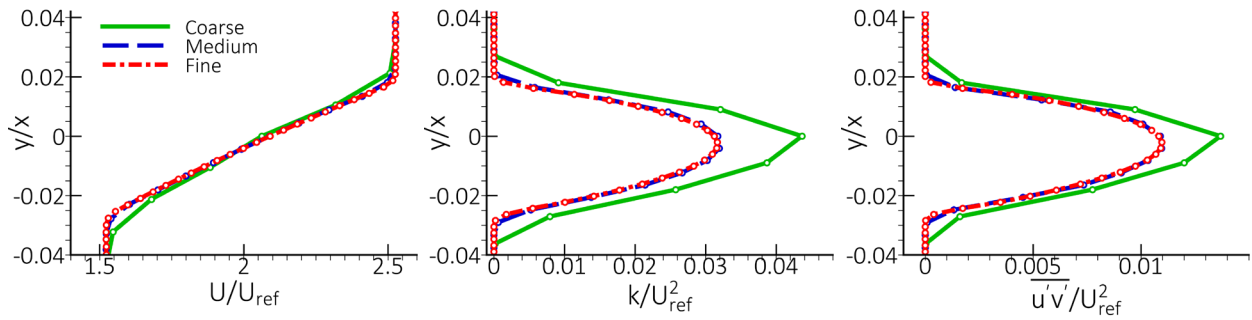
**Figure 78: Comparison of the velocity (left), turbulence kinetic energy (middle) and Reynolds shear-stress (right) profiles on different meshes for the mixing layer.**

### 4.9.3. Fully Turbulent Boundary Layers

Wall boundary layers are the most demanding in terms of mesh resolution, as the solution gradients inside boundary layers can be very high. This is true for both, primary solution variables, like velocity or temperature, but even more so for turbulence quantities like $k$, $\omega$ or $\varepsilon$.

Most CFD users are fixated on the $y^+$ values of the first cell center of the wall cells and assume that achieving a given threshold $y^+$ value ensures enough mesh resolution inside the boundary layer. This is not the case as a given $y^+$ value does not by itself ensure that there are enough cells inside the boundary layer. It is important to understand that for the same $y^+$-value and the same grid expansion ratio (growth rate between cells $ER = \Delta y_{j+1}/\Delta y_j$) there would be many more cells inside a high Reynolds number boundary layer than in a low Reynolds number one. This is clear from Figure 79 which shows that the boundary layer thickness in terms of $\delta^+$ is much larger for the high than for the low Reynolds number case.
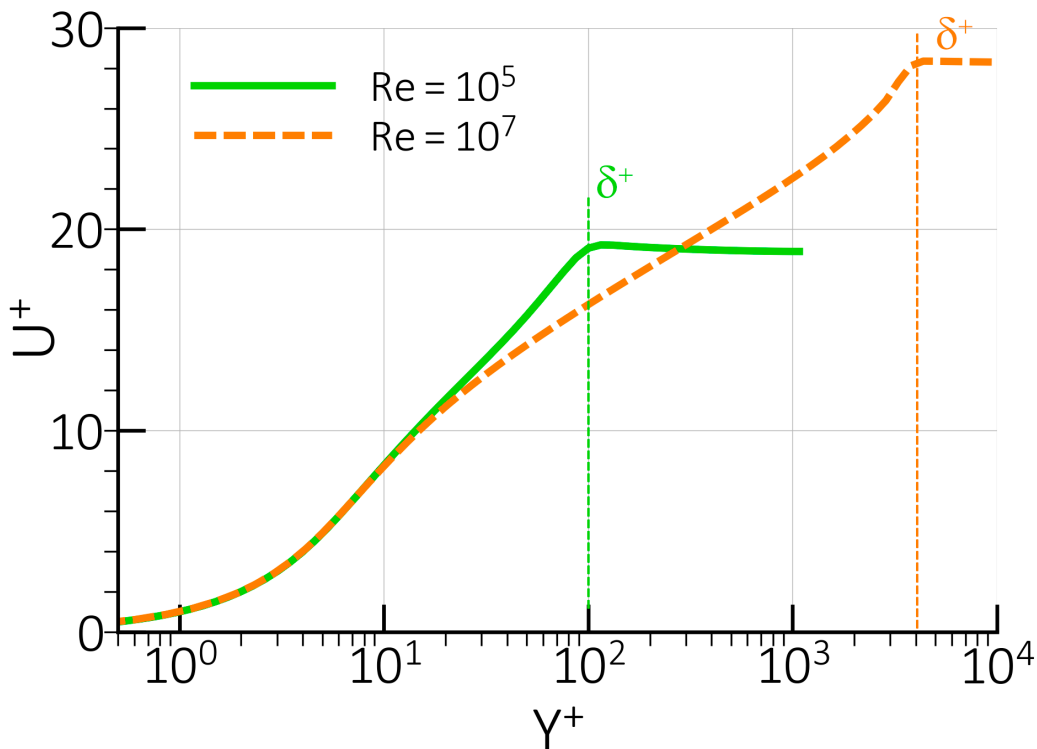


**Figure 79: Boundary layer thickness in wall units for low and high Reynolds number.**

The main quality criterion for boundary layer meshes is therefore not $y^+$, but the number of cells (prism layers) <u>inside</u> the boundary layer (estimates of boundary layer thickness are given in Section 9.4). It is important to stress the word 'inside', as prism layers generated with a given number of cells do not ensure that the layers are resolving the boundary layer – it is easy to create prism layers where the boundary layer is much thinner or much thicker than the prism layer height. If prismatic

layers cover only a part of the boundary layer (see Figure 80) it is under-resolved due to a large edge length change from the prism layers to the tetra/poly cells. In this case, the outer part of the boundary layer cannot be resolved.
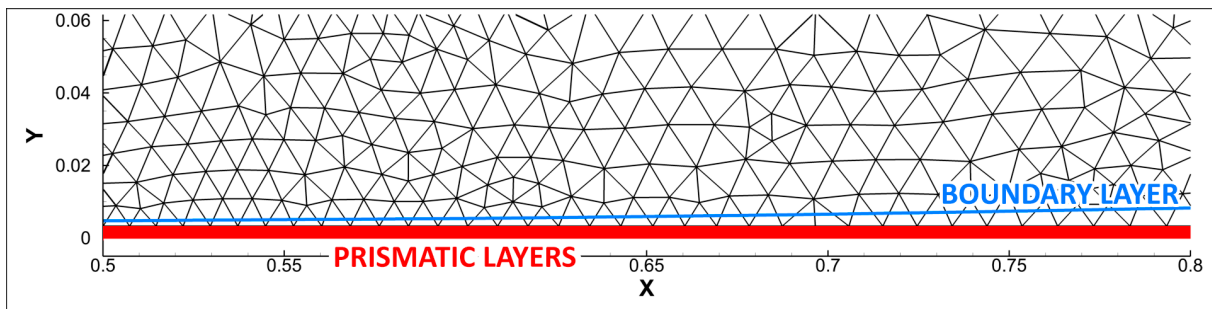


**Figure 80: Computational unstructured mesh with prismatic layers (red) thinner than the boundary layer (blue line) thickness.**

There is no single number for how many cells across a boundary layer are optimal, as this depends on the type of flow and the required accuracy. The highest accuracy demands are for external aeronautical applications with safety concerns – especially aircraft simulations. For such flows, boundary layers are often resolved with 30-40 cells. For most industrial flows, 10 layers inside the boundary layer are reasonable. However, there are also many technical flows, where only smaller cell counts can be afforded, and reasonable solutions can often be achieved with only 3-5 layers.

The need to accurately resolve the boundary layer increases with the need:

- To resolve flow separation from smooth surfaces like airfoils (contrary to separation from geometric discontinuities like edges or corners).
- Flows with heat transfer, where the resolution of conditions in the very near wall region is important. This is even more important for flows with high Prandtl numbers, where the thermal sublayer is very thin.
- Flows with laminar-turbulent transition, where the laminar boundary layers are typically very thin and needs to be resolved for the transition model to operate properly (see below).

Streamwise resolution is typically several times the boundary layer thickness (say 1-5), whereas 'spanwise' grid spacing can be even higher depending on the gradients in that direction (for 2D flows it can be arbitrarily coarse). However, in most technical flows, there is no clear distinction between streamwise and spanwise and the grid surface spacing is then typically selected as 'isotropic'.

Grid resolution of boundary layers should be checked during and/or after the simulation. A good quantity to visualize is the ratio of turbulent to molecular viscosity ($TVR = \mu_t/\mu$). It has a maximum near the center of the boundary layer and decays to low freestream values outside the layer. Visualizing TVR in a contour plot with overset grid lines allows a good estimate of grid resolution by counting the wall normal cells which are inside the elevated TVR levels near the wall. This is shown in Figure 81 for different grids for a NACA 4412 airfoil. Here the fine grid provides a grid-independent solution, while the boundary layer is under resolved near the leading edge for the coarse and medium grids. There are ~ 5 cells across the boundary layer near the leading edge for the medium mesh and the coarse mesh does not resolve the boundary layer at all. As a result, the boundary layer is thicker for these meshes which leads to earlier separation (see Figure 82) on the suction side of the airfoil. The local mesh refinement in wall normal direction in the leading-edge region, shown in Figure 83 improves the prediction of the boundary layer. Figure 84 shows that the results on the refined medium mesh and on the fine mesh are in good agreement.

Coarse

Medium

Fine
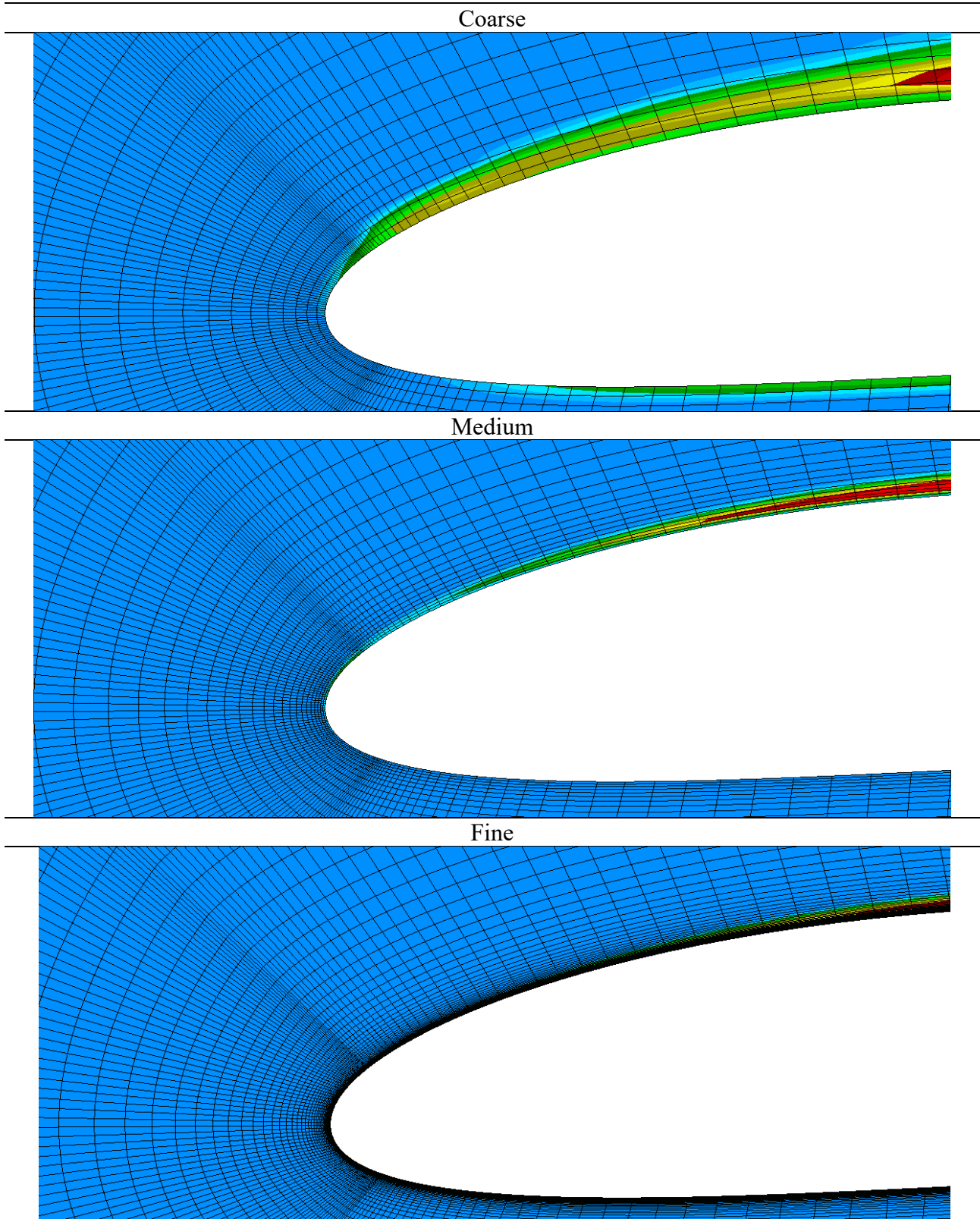
**Figure 81: The boundary layers thickness visualized by eddy-viscosity ratio field for different meshes around NACA-4412 airfoil. Blue color shows the area of the inviscid flow.**
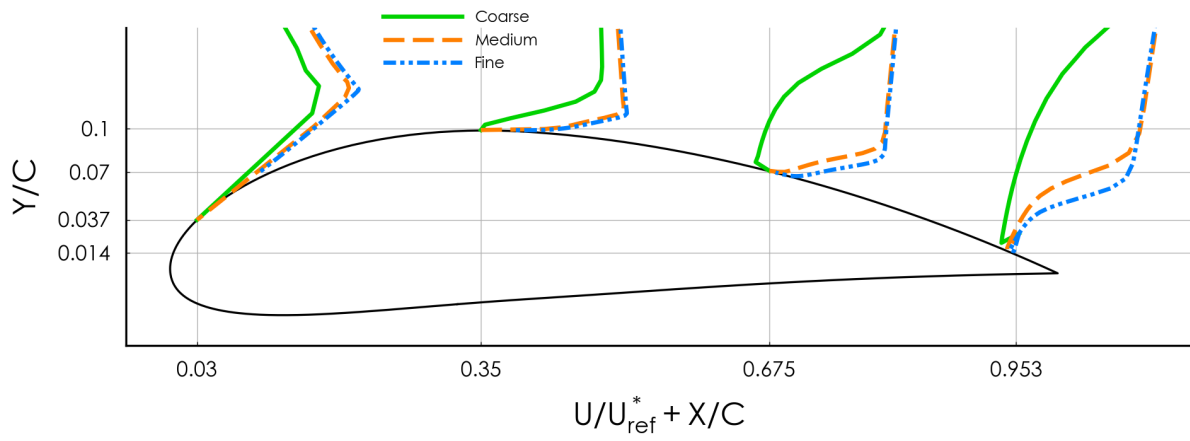
**Figure 82: Comparison of velocity profiles on different meshes for flow around the NACA-4412 airfoil.**
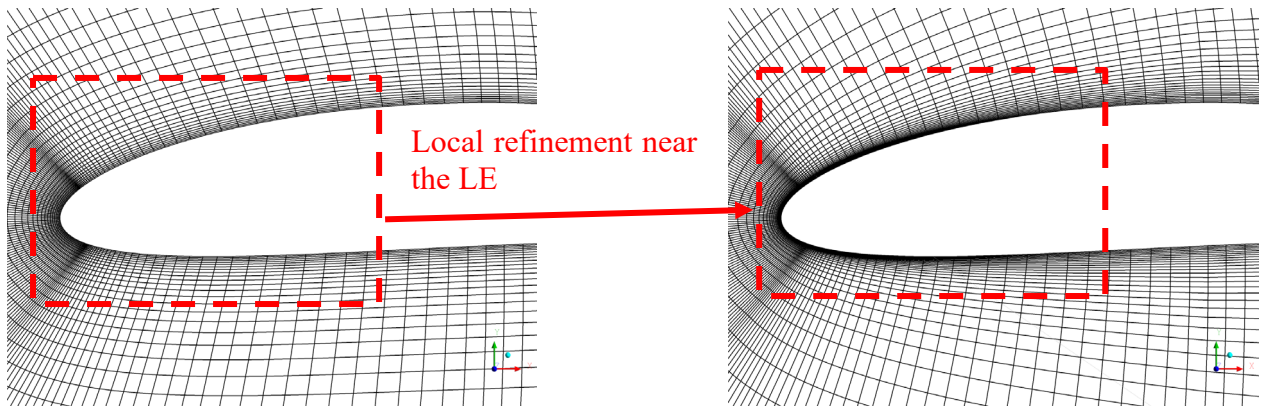


**Figure 83: Local mesh refinement on the leading edge for the medium mesh.**
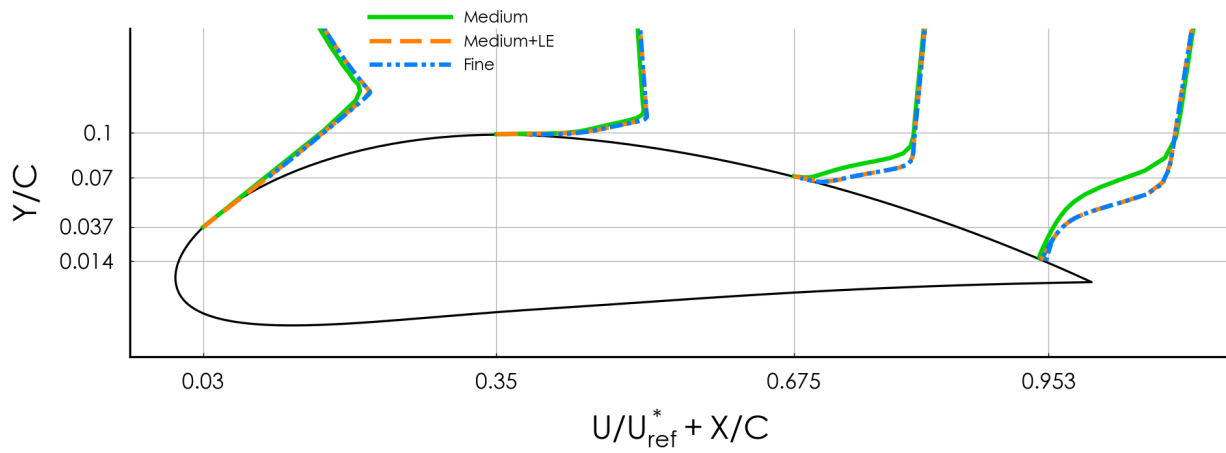


**Figure 84: Comparison of the velocity profiles on the medium and refined medium (medium+LE) meshes.**

Another grid-quality measure is the smoothness by which prism layers merge into the outer unstructured mesh. Grids with large size jumps in this region should be avoided as they can inhibit the proper growth of the boundary layer (which then cannot grow outside the prism layer mesh due to low resolution). The optimal mesh structure:

- Prismatic layers cover the entire boundary layer.
- The number of prismatic layers should be sufficient for the boundary layer resolution.
  - The first near wall grid step ensures $y^+ < 1$ without wall treatment.
  - However, higher y+ values can also be applied if the overall number of cells across the layer is sufficient.
- Smooth connection of the prismatic layers and tetra/poly cells.
- Streamwise grid step at the wall should be sufficient for the proper resolution of the flow features.
  - stagnation region
  - separation
  - shock wave
  - transition
  - corner flow

Figure 85 illustrates the optimal mesh topology and resolution for an unstructured mesh for the flow around an airfoil.
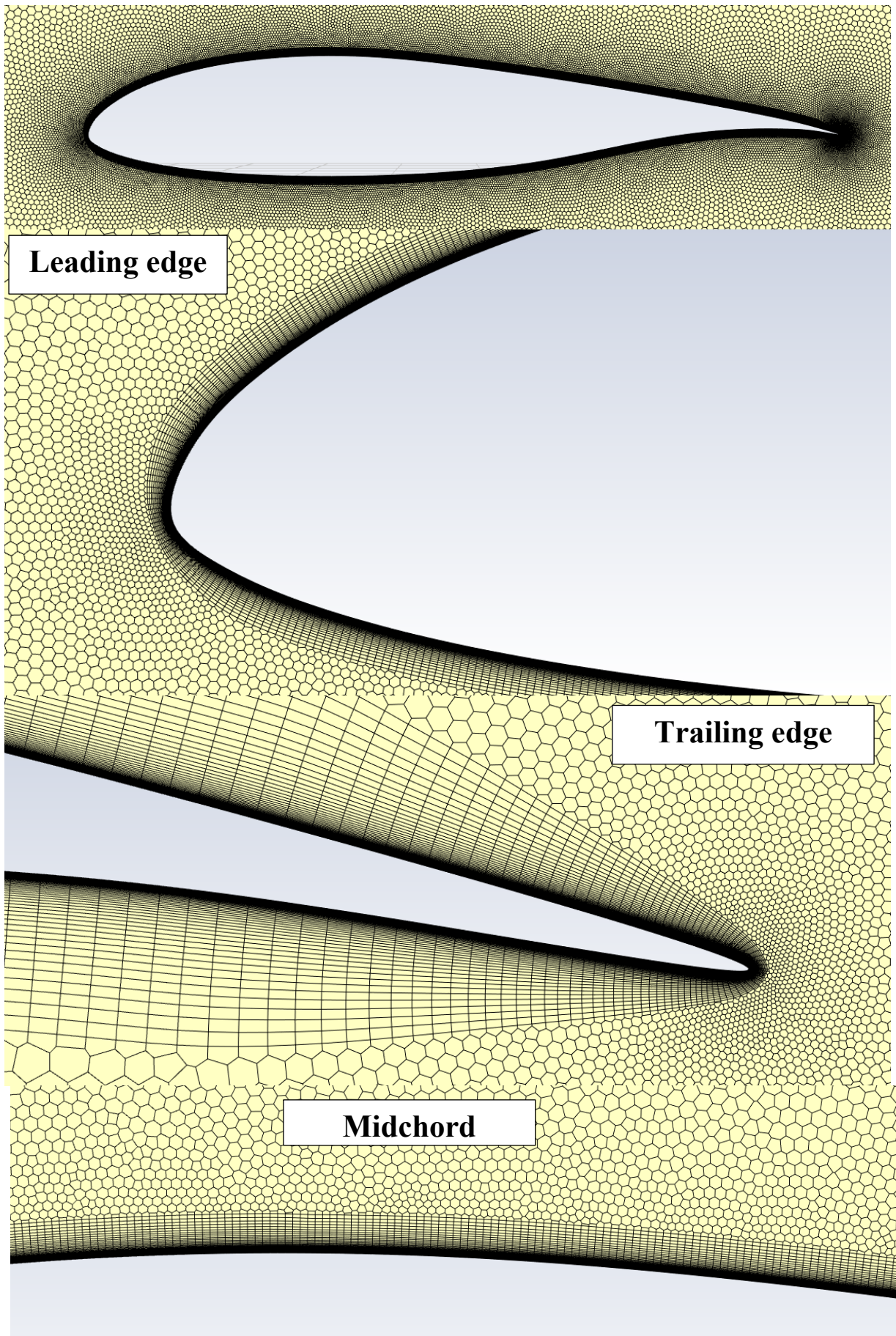
**Figure 85: Optimal unstructured mesh topology for flow around airfoil.**

### 4.9.4. Transitional Boundary Layers

Boundary layers undergoing transition are more sensitive to the mesh resolution than fully turbulent boundary layer. Meshes for fully turbulent simulations are not sufficient in the transition region, especially in the streamwise direction. Unfortunately, the transition location is unknown without precursor simulations in most cases. Therefore, a two-stage approach is recommended for the computations using transition models:

- 1st stage – computations on the baseline fine fully turbulent mesh and estimation of the transition region.
- 2nd stage – mesh refinement in streamwise, wall-normal and spanwise (in case of the fully three-dimensional flow) directions in the transition region. Repeat until grid-converged solution is achieved.

It should be noted that the mesh requirements also depend on the transition model choice. Here the three transition models described in section 3.4.1 are considered. Figure 87 shows the effect of streamwise mesh resolution on the transition prediction on the flat plate for different transition models. The baseline fully turbulent mesh with streamwise grid step $\Delta x = 10\delta$ ($\delta$ is boundary layer thickness) is only sufficient for the $\gamma$-$Re_\theta$-SST model but not for the other two models and should be refined in the transition region. The baseline and refined meshes are shown on Figure 86. For the refined mesh, the streamwise grid step is $\Delta x = 1\delta$ in the transition region and $\Delta x = 10\delta$ in the laminar and fully turbulent parts. In this context it is important to note that for many technical devices, transition is triggered through laminar-turbulent bubble separation. In such cases, the streamwise mesh resolution is even more important to detect and resolve the laminar bubble. It is usually required to resolve the bubble with 5-10 streamwise cells. For this reason, it is not recommended in general to use coarse $\Delta x$ spacings in transition simulations, as the mechanism of transition is often not known a priori.

In case of first near wall height variation the transition location is insensitive to $y_1^+ < 1$ in the transition region (see Figure 88). For higher values of $y_1^+$ in this area, the transition location moves upstream. For both streamwise and wall-normal mesh studies the two-equation model ($\gamma$- $Re_{\theta t}$-SST) is much less sensitive to the mesh resolution than one-equation intermittency transition model ($\gamma$-SST), or the algebraic intermittency model ($\gamma$-alg-SST), which is most sensitive to the mesh resolution.

Finally, the basic recommendation for all the transition models for the mesh generation.
- $\Delta x = 1\delta$ in the transition region
- $\Delta y_1^+ < 1$ in the transition region
- $ER < 1.1$ in the transition region ($ER = \Delta y_{j+1}/\Delta y_j$)
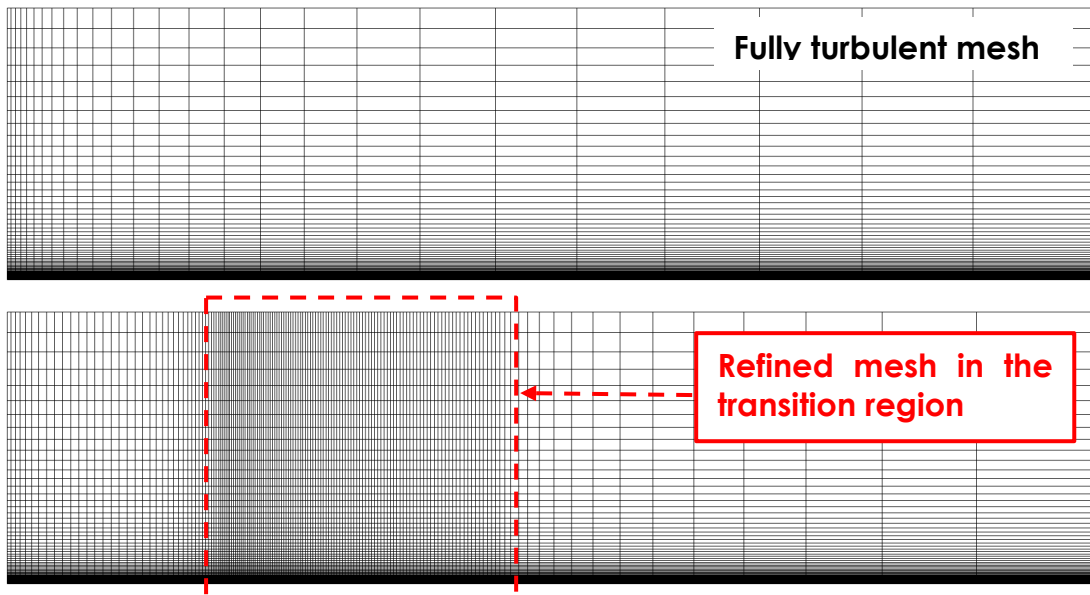
**Figure 86: Computational meshes for the fully turbulent (upper) and transitional (lower) boundary layer.**
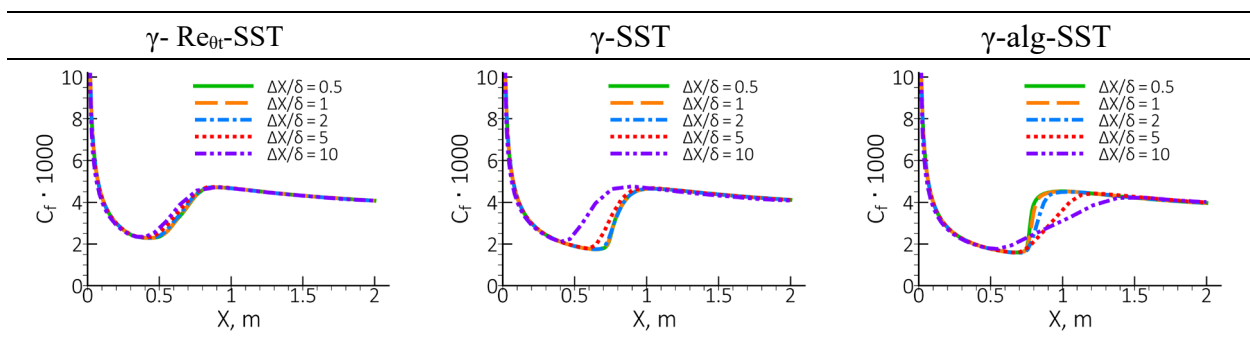


**Figure 87. Effect of the resolution of transition region in streamwise direction for different transition models for the T3A flat plate boundary layer.**
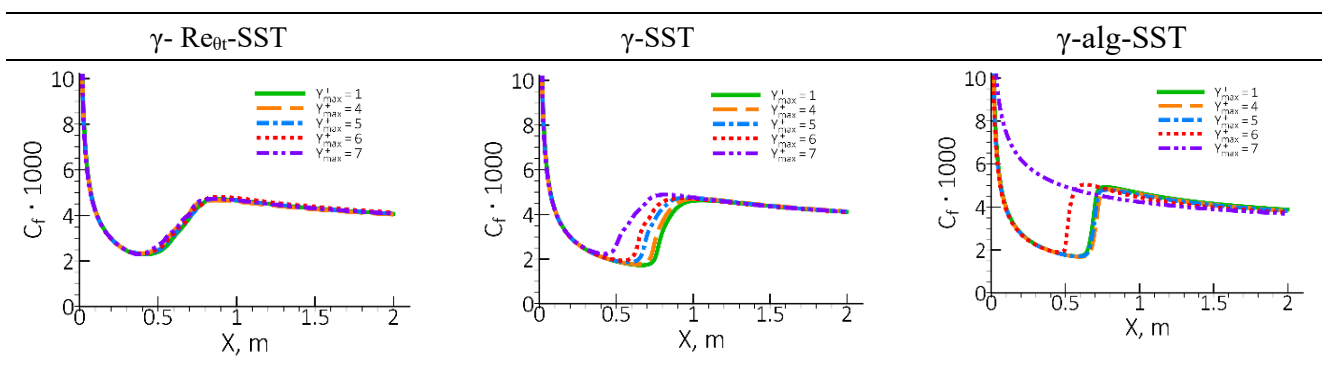


**Figure 88. Effect of the resolution of transition region in wall-normal wall direction for different transition models for T3A the flat plate boundary layer.**

## 4.9.5. Corner Flows

When activating the Corner Flow Correction or an EARSM to compute the secondary flow into corners, the mesh resolution into the corners especially for unstructured meshes (tetrahedral, polyhedral or cartesian), is critical.

Ideal meshes for corner flows are structured meshes as shown in Figure 89 where the wall normal refinement for one wall ensures automatically proper refinement into the corner for the adjacent walls (meaning small edge length on the wall going into the corner). Such corner mesh refinement

avoids additional mesh refinement in the streamwise direction which should be done for the unstructured meshes.

The meshing requirements to resolve the corner flow are especially challenging for the DLR diffuser [41] described in Section 4.3.2. For this test case, a uniform flow (U = 10m/s, Tu = 1%, TVR = 1) was specified at the inlet. This results in a very thin boundary layer at the onset of the diffuser. While this boundary layer can easily be resolved in wall normal direction, it is much harder to resolve the flow dynamics into the corner (the secondary flow is taking place inside the boundary layer and has to be resolved in the plane normal to the mean flow direction). While the structured mesh (Str mesh) in Figure 89 has sufficient resolution in that area due to its mesh topology, the resolution of this zone by unstructured meshes is much harder. Two unstructured meshes, one without refinement (PH-1) and one with refinement (PH-2) into the corner are shown in Figure 90 and Figure 91, respectively. Figure 92 shows contours of the eddy-viscosity ratio with the mesh plotted on top. It is intuitively clear that mesh PH-1 does not have sufficient resolution into the corner. While the mesh can be refined into the corners (PH-2), it results in a disproportionably large mesh count due to local refinement in all directions. For the current example, the mesh size is increased by a factor ten between the two grids shown. Another issue is that due to the refinement into the corner, the thickness of the prismatic layer shrinks in the corner region (Figure 91).

The effect of mesh refinement on the structure and strength of the corner vortex can be seen in Figure 93. Clearly, mesh PH-1 is not sufficient to resolve the vortex. Figure 94 shows the skin friction prediction on the inclined wall for the DLR diffuser for the two unstructured meshes in comparison with a structured Hex-mesh (Str) using the SST-CFC model. It is evident that the mesh resolution near the corners is not only important near the corners but also affects the flow in the center. In the current test case, the effect on the center part of the flow is moderate and the predicted pressure distribution (Figure 95) is in good agreement with the experimental data for both unstructured meshes. Note however that the incorrect prediction of corner flow separation can in the worst-case result in incorrect flow topologies which in turn can have a strong impact on global flow parameters.

It is important to stress, that the challenge for the DLR diffuser lies in the thin boundary layer in the corner region. For flows with a fully developed inlet profile, like the Stanford diffuser [42], the resolution requirements are much less demanding. In any case, meshes with intersecting mesh lines from the two side walls (like in the structured mesh) are ideal for such simulations.

**Cross section**                                   **3D view**
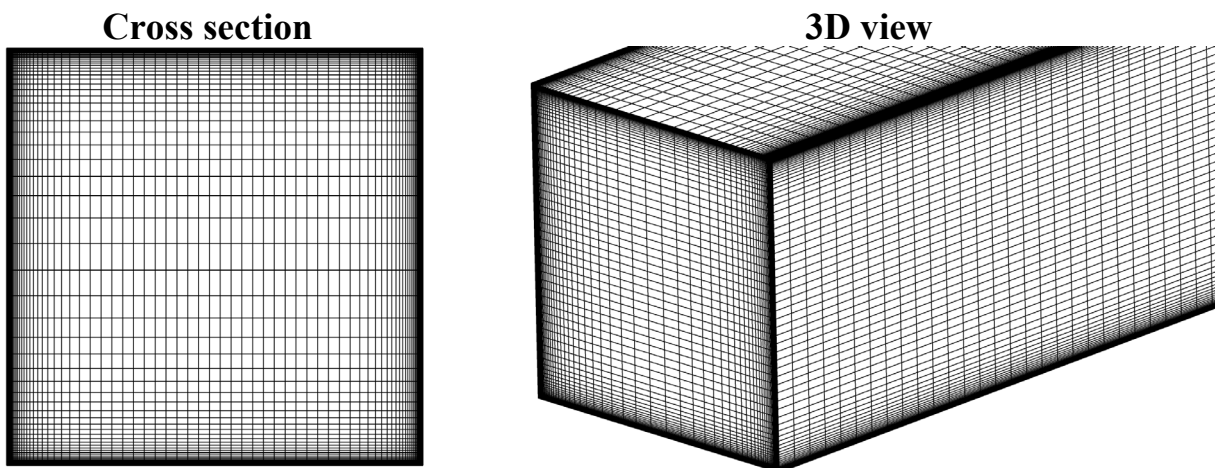


Figure 89. Baseline structured mesh with fine resolution in the corners for the DLR-Diffuser [41].
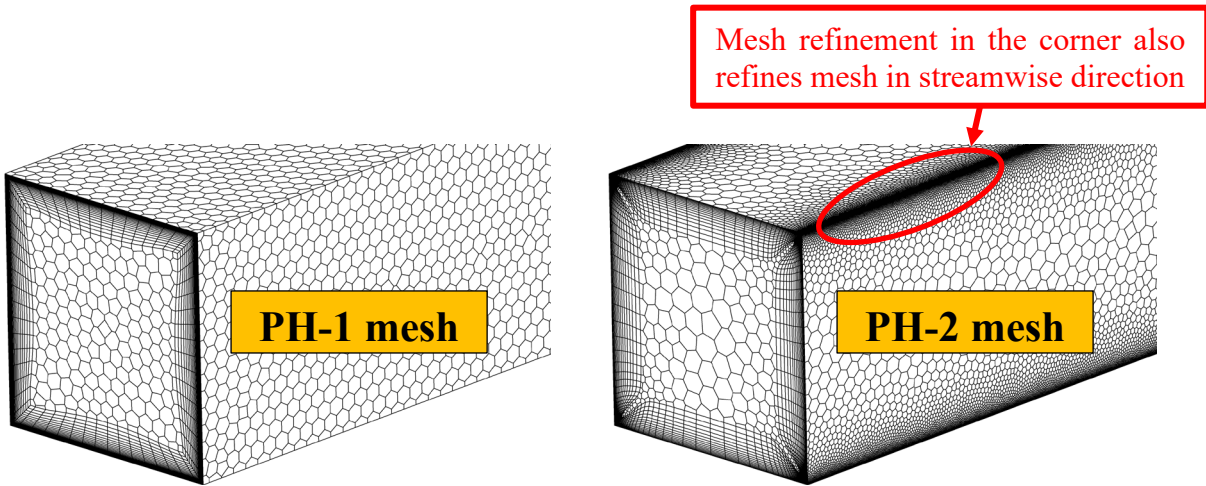
**Figure 90. Baseline mesh PH-1 (left) and refinement mesh PH-2 (right) near the corners for the unstructured meshes for the DLR-Diffuser [41].**
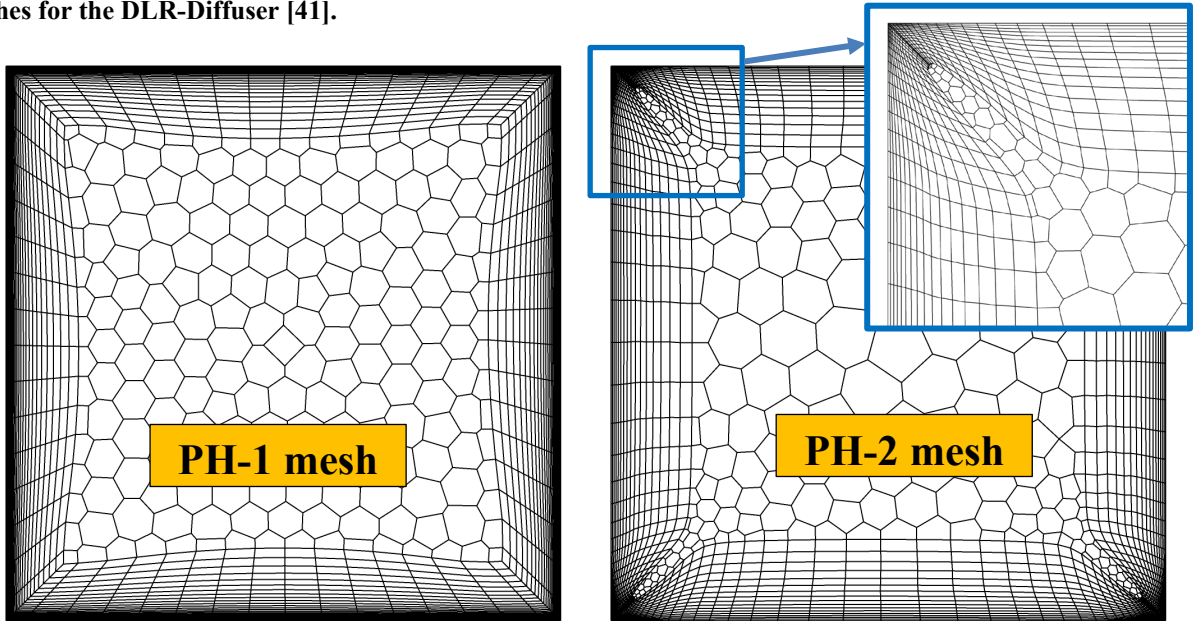


**Figure 91. Cross section of typical unstructured mesh PH-1 in rectangle channel (left) and collapsing of the prismatic cells near the corners on the refined mesh PH-2 (right) for the DLR-Diffuser [41].**

**Structured mesh**  **PH-1 mesh**  **PH-2 mesh**



**Structured mesh**  **PH-1 mesh**  **PH-2 mesh**
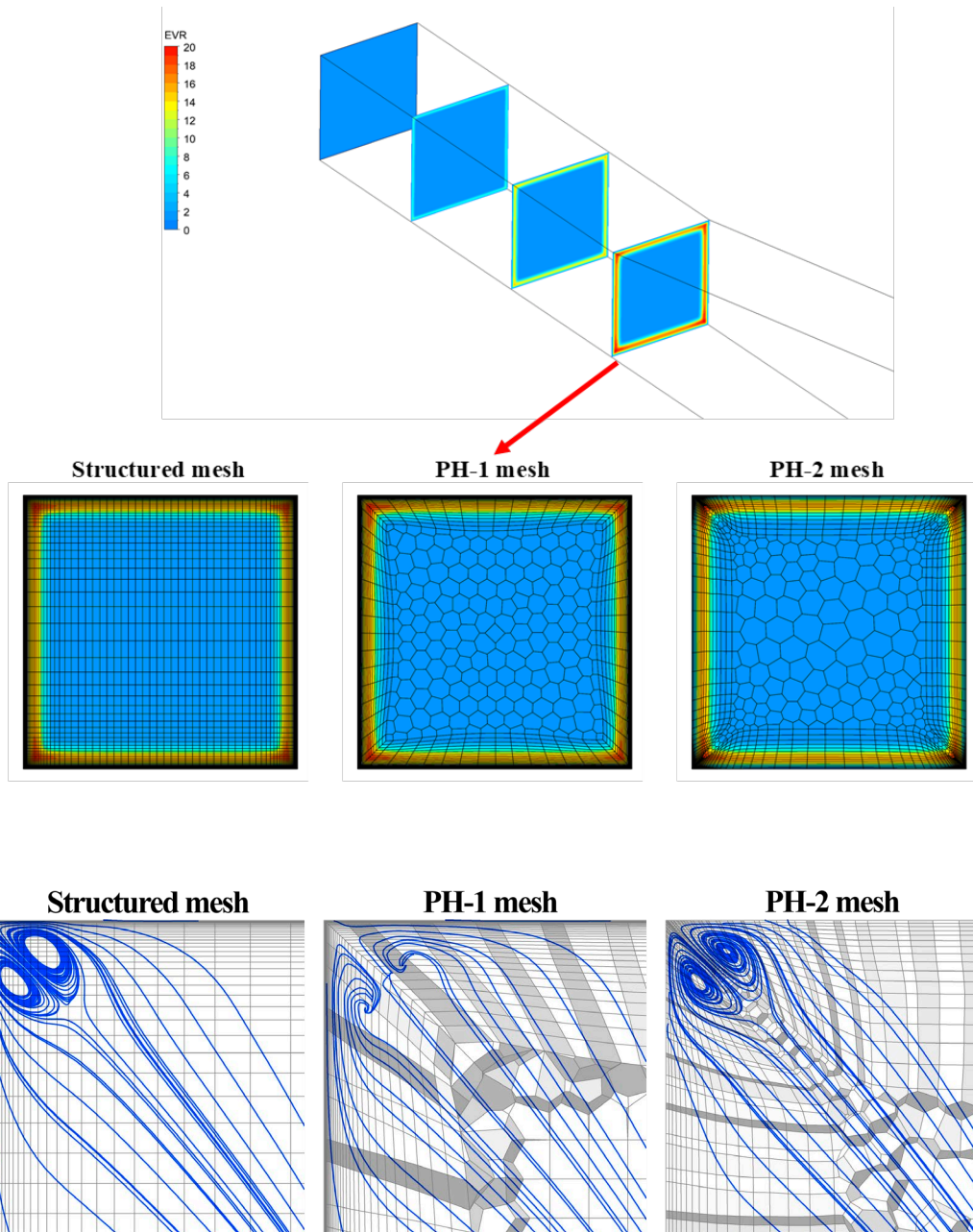
**Figure 93: Streamlines of crossflow pattern at the start of the diffuser for three different meshes.**
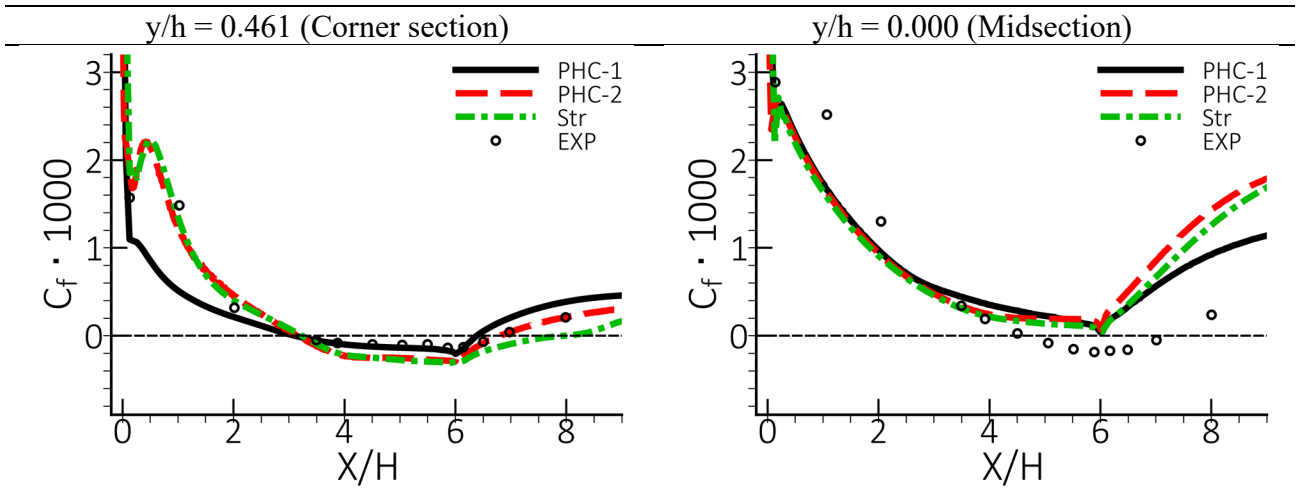
**Figure 94: Distribution of the skin friction along the diffuser at midsection (left) and near the corner (right) for SST-CFC for the DLR diffuser for two unstructured and one structured mesh [41].**
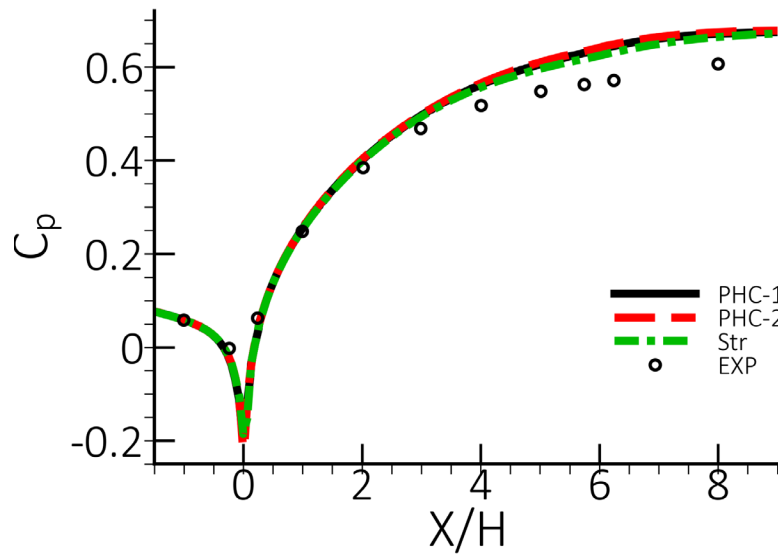


**Figure 95: Distribution of the pressure coefficient along the diffuser at midsection for SST-CFC for the DLR diffuser for two unstructured and one structured mesh [41].**

# 5. Numerical Settings

CFD simulations based on RANS models are typically carried out in 'steady-state' model (see Section 3.2). In most cases the following settings are appropriate:

- Coupled solver
- Pseudo-transient
    - Use default proposed time step
    - In case of convergence problems vary time step
- Second order momentum
- Second order turbulence
    - This is very helpful for unstructured grids and or grids not well aligned with the flow. For hexahedral grids with good flow alignment the difference between 1st and 2nd order space discretization is typically moderate.
    - Experience has shown that 2nd order space discretization for turbulence does not have an overall negative influence on convergence – it is therefore recommended.

## 5.1.1. Example: High-Lift Aircraft

A drastic example for the danger of non-converged solutions is the following flow around a generic airplane geometry with high-lift devices (slats upstream and flaps downstream of the wing employed) deployed. The simulations for the JAXA geometry were carried out in the framework of the 3rd AIAA CFD High Lift prediction Workshop (https://hiliftpw.larc.nasa.gov/Workshop3/geometries.html). A first simulation with the SST model using default model and steady state settings resulted in a substantial under-prediction of the maximum lift coefficient ($C_{Lmax}$) due to a massive separation on the main wing. This can be seen in Figure 96 (left) showing the skin friction on the surface for the 'steady-state' set-up for an angle of attack of $\alpha=18°$. At first, this was attributed to the SST model's separation prediction capabilities, which were apparently interpreted as being overly 'aggressive' for this case. For this reason, the $a_1$ coefficient in the SST model was increased to $a_1 = 1$ to reduce separation sensitivity. However, it was found that convergence for the case with the default SST model setting was poor and the case was therefore re-run with unsteady solver settings. The difference due to this change in numerical settings was dramatic as shown in Figure 96 (right) which shows the skin friction distribution for the unsteady run. The unsteady set-up allowed the simulation to 'escape' from the incorrect flow topology and move to a more realistic and much less separated condition.

The effect on the lift coefficient can be seen in Figure 97 which contains three curves. One for SST-default and 'steady state mode', one for SST with $a_1=1.0$ (instead of default $a_1=0.31$) and again 'steady state mode' and finally with SST default ($a_1=0.31$) and 'unsteady mode'. The change in the $a_1$ coefficient results in less separation and therefore a better agreement with the experimental data. However, such a change in $a_1$ is not justified from a physics standpoint, when considering 2D airfoil performance (see 4.2.2). Alternatively, the solution was also improved significantly by switching from the steady-state set-up to the unsteady set-up. The lift for the URANS simulation is still somewhat lower than the experiment, but by a much lower factor compared with to that from the steady run. There is also indication that including laminar-turbulent transition in the simulation will further increase the lift curve, so that the remaining difference can partly be attributed to this effect.
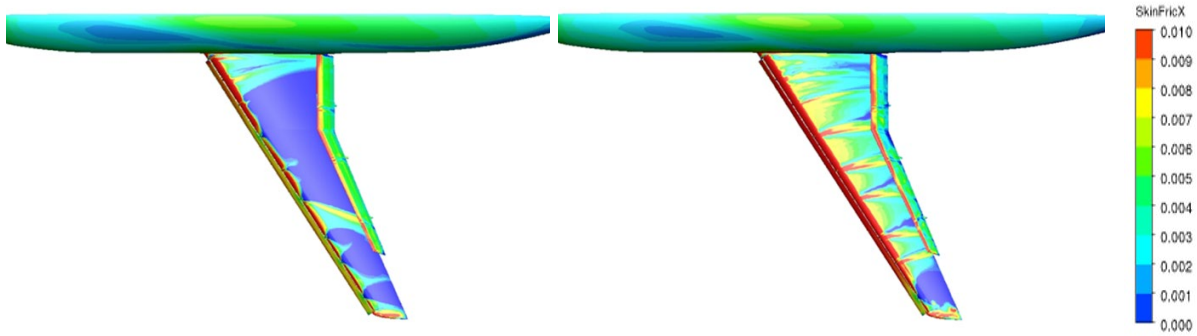
**Figure 96: Wall shear stress for high-lift airplane simulation for α=18°. Left: Simulation in 'steady-state mode'. Right: Simulation in 'unsteady mode'.**
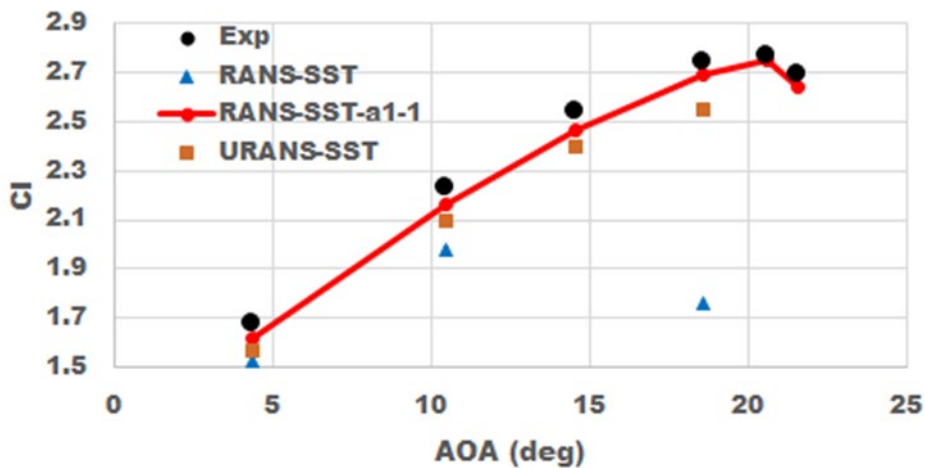


**Figure 97: Lift coefficient, Cl, for high-lift aircraft simulation versus angle of attack (AOA). RANS-SST with default and 'steady state mode', SST with a1=1.0 and 'steady state mode' and URANS-SST with default SST and 'unsteady mode' set-up.**

It is important to stress that situations like the one shown above appear very seldomly, but they can happen in CFD. The exact cause for such scenarios is not easy to determine. However, there are some contributing factors:

- Large variation in size of geometric features (in this case the thin pylons holding the slat versus the size of the airfoil).
- Large variation in cell size between different regions (often because of the first bullet point).
- Large aspect ratio grids in the domain.
- Potential for topology changes in the flowfield – meaning that the flow can change from 'attached' to stalled' on certain sections of the wing.
- Local regions of unsteady flow with relevance to the overall flow topology.

# 6. Summary

The current document has been compiled to provide information about the optimal selection and usage of turbulence models. It was pointed out that not all differences between CFD simulations and experimental data are the responsibility of the turbulence model, but that many different set-up details play a crucial role.

The turbulence modeling strategy at Ansys, designed around $k$-$\omega$ models was discussed and different sub-models of that family have been presented in comparison with different types of $k$-$\varepsilon$ models. It was shown that the $k$-$\omega$ based models offer significant advantages in terms of integration

to the wall, as well as increased accuracy and robustness for complex flows, especially flows with separation from smooth walls.

The motivation behind the tunable GEKO model has been presented. The influence of the different parameters has been shown for some building-block flows. A more detailed Best Practice document for the GEKO model is available [9], in addition to a Best Practice Document for Scale-Resolving Simulations [1].

Numerous sub-models and model extensions have been discussed and their effect on the simulation has been presented.

An area of active research in turbulence modeling is Machine Learning (ML). The topic has not reached the maturity required to be included in a Best Practice document. However, Ansys is currently developing a comprehensive infrastructure for optimization of GEKO parameters using ML. This infrastructure is based on an adjoint solver for the turbulence model in Ansys Fluent$^{®}$ including non-linear EARSM coefficients. The infrastructure will enable users to employ ML concepts to their own CFD applications in an integrated and convenient fashion.

# 7. Acknowledgment

# 8. References

[1] F. R. Menter, "Best Practice: Scale-Resolving Simulations in ANSYS CFD," ANSYS Report.

[2] P. A. Durbin, P.A. and Petterson Reif, B.A., *Statistical Theory and Modeling for Turbulent Flows*. Wiley, 2010.

[3] Leschziner, M., *Statistical Turbulence Modelling For Fluid Dynamics - Demystified: An Introductory Text For Graduate Engineering Students*. Imperial College Press, London, 2016.

[4] Pope, S.B., *Turbulent Flows*. Cambridge University Press, 2000.

[5] Hanjalic, K. and Launder, B., *Modelling Turbulence in Engineering and the Environment*. Cambridge University Press, 2011.

[6] Rotta, J.C., *Turbulente Strömungen - Eine Einführung in die Theorie und ihre Anwendung*. Springer Verlag, 1972.

[7] D. C. Wilcox D.C., *Turbulence Modeling for CFD*. DCW Industries, 2006.

[8] ERCOFTAC Best Practice Guidelines, *Industrial Computational Fluid dynamics of Single Phase Flows*. 2000. [Online]. Available: https://www.ercoftac.org/publications/ercoftac_best_practice_guidelines/single-phase_flows_spf

[9] F. R. Menter, R. Lechner, and A. Matyushenko, "Best Practice: Generalized k-w Two-Equation Turbulence Model in ANSYS CFD (GEKO)," ANSYS Germany GmbH, ANSYS Report, 2019.

[10] F. R. Menter, A. Matyushenko, and R. Lechner, "Development of a Generalized K-ω Two-Equation Turbulence Model," in *New Results in Numerical and Experimental Fluid Mechanics XII*, 2020, pp. 101–109. doi: 10.1007/978-3-030-25253-3_10.

[11] P. Spalart and S. Allmaras, "A One-Equation Turbulence Model for Aerodynamic Flows," *AIAA*, vol. 439, Jan. 1992, doi: 10.2514/6.1992-439.

[12] J. C. Vogel and J. K. Eaton, "Combined Heat Transfer and Fluid Dynamic Measurements Downstream of a Backward-Facing Step," *Journal of Heat Transfer*, vol. 107, no. 4, pp. 922–929, Nov. 1985, doi: 10.1115/1.3247522.

[13] D. Cokljat, S.-E. Kim, G. Iaccarino, and P. Durbin, "A Comparative Assessment of the V2F Model for Recirculating Flows," presented at the 41st Aerospace Sciences Meeting and Exhibit, Reno, Nevada, Jan. 2003. doi: 10.2514/6.2003-765.

[14] W. P. Jones and B. E. Launder, "The prediction of laminarization with a two-equation model of turbulence," *International Journal of Heat and Mass Transfer*, vol. 15, no. 2, pp. 301–314, Feb. 1972, doi: 10.1016/0017-9310(72)90076-2.

[15] T.-H. Shih, W. W. Liou, A. Shabbir, Z. Yang, and J. Zhu, "A new k-ϵ eddy viscosity model for high Reynolds number turbulent flows," *Computers & Fluids*, vol. 24, no. 3, pp. 227–238, Mar. 1995, doi: 10.1016/0045-7930(94)00032-T.

[16] O. S. A *et al.*, "Renormalization Group Modeling and Turbulence Simulations.," *Near-Wall Turbulent Flows*, pp. 1031–1046, 1993.

[17] F. R. Menter, "Two-equation eddy-viscosity turbulence models for engineering applications," *AIAA Journal*, vol. 32, no. 8, pp. 1598–1605, Aug. 1994, doi: 10.2514/3.12149.

[18] F. R. Menter, M. Kuntz, and R. Langtry, "Ten Years of Industrial Experience with the SST Turbulence Model," *Proceedings of the 4th International Symposium on Turbulence, Heat and Mass Transfer, Begell House Inc., West Redding, 2003, pp. 625-632.*.

[19] S. Wallin and A. V. Johansson, "An explicit algebraic Reynolds stress model for incompressible and compressible turbulent flows," *J. Fluid Mech.*, vol. 403, pp. 89–132, Jan. 2000, doi: 10.1017/S0022112099007004.

[20] P. R. Spalart, "Strategies for turbulence modelling and simulations," p. 12, 2000.

[21] Kato M and Launder B.E., "The Modeling of Turbulent Flow Around Stationary and Vibrating Cylinders," presented at the Ninth Symposium on Turbulent Shear Flows, Kyoto Japan, 1993.

[22] P. E. Smirnov and F. R. Menter, "Sensitization of the SST Turbulence Model to Rotation and Curvature by Applying the Spalart–Shur Correction Term," *Journal of Turbomachinery*, vol. 131, no. 4, 2009, doi: 10.1115/1.3070573.

[23] P. R. Spalart and M. Shur, "On the sensitization of turbulence models to rotation and curvature," *Aerospace Science and Technology*, vol. 1, no. 5, pp. 297–302, Jul. 1997, doi: 10.1016/S1270-9638(97)90051-1.

[24] F. R. Menter, R. B. Langtry, S. R. Likki, Y. B. Suzen, P. G. Huang, and S. Völker, "A Correlation-Based Transition Model Using Local Variables—Part I: Model Formulation," *Journal of Turbomachinery*, vol. 128, no. 3, pp. 413–422, Mar. 2004, doi: 10.1115/1.2184352.

[25] R. B. Langtry, F. R. Menter, S. R. Likki, Y. B. Suzen, P. G. Huang, and S. Völker, "A Correlation-Based Transition Model Using Local Variables—Part II: Test Cases and Industrial Applications," *Journal of Turbomachinery*, vol. 128, no. 3, pp. 423–434, Mar. 2004, doi: 10.1115/1.2184353.

[26] R. B. Langtry and F. R. Menter, "Correlation-Based Transition Modeling for Unstructured Parallelized Computational Fluid Dynamics Codes," *AIAA Journal*, vol. 47, no. 12, pp. 2894–2906, Dec. 2009, doi: 10.2514/1.42362.

[27] N. V. Nikitin, N. V. Popelenskaya, and A. Stroh, "Prandtl's Secondary Flows of the Second Kind. Problems of Description, Prediction, and Simulation," *Fluid Dyn*, vol. 56, no. 4, pp. 513–538, Jul. 2021, doi: 10.1134/S0015462821040091.

[28] B. Aupoix, "Roughness Corrections for the k–ω Shear Stress Transport Model: Status and Proposals," *Journal of Fluids Engineering*, vol. 137, no. 2, Sep. 2014, doi: 10.1115/1.4028122.

[29] K. Wieghardt and W. Tillmann, "On the Turbulent Friction Layer for Rising Pressure," *UNT Digital Library*, Oct. 1951. https://digital.library.unt.edu/ark:/67531/metadc62980/ (accessed Jul. 23, 2021).

[30] D. Driver, D.M., "Reynolds shear stress measurements in a separated boundary layer flow," in *22nd Fluid Dynamics, Plasma Dynamics and Lasers Conference*, American Institute of Aeronautics and Astronautics, 1991. doi: 10.2514/6.1991-1787.

[31] D. M. Somers, "Design and experimental results for the S805 airfoil," National Renewable Energy Lab., NREL/SR--440-6917, Jan. 1997.

[32] D. M. Somers, "Design and Experimental Results for the S825 Airfoil," National Renewable Energy Lab., NREL/SR-500-36346, Jan. 2005.

[33] D. M. Somers, "Design and Experimental Results for the S809 Airfoil," *NRELSR-440-6918*, p. 103, 1997.

[34] D. M. Somers, "Design and experimental results for the S814 airfoil," National Renewable Energy Lab., NREL/SR--440-6919, Jan. 1997.

[35] W. A. Timmer and R. V. Rooij, "Summary of the Delft University Wind Turbine Dedicated Airfoils," *AIAA Paper 2003-0352*, 2003, doi: 10.1115/1.1626129.

[36] F. R. Menter, P. E. Smirnov, T. Liu, and R. Avancha, "A One-Equation Local Correlation-Based Transition Model," *Flow Turbulence Combust*, vol. 95, no. 4, pp. 583–619, Dec. 2015, doi: 10.1007/s10494-015-9622-4.

[37] G. Schewe, "Reynolds-number effects in flow around more-or-less bluff bodies," *Journal of Wind Engineering and Industrial Aerodynamics*, vol. 89, no. 14–15, pp. 1267–1289, Dec. 2001, doi: 10.1016/S0167-6105(01)00158-1.

[38] A. Wadcock, "Investigation of low-speed turbulent separated flow around airfoils," Sep. 1987.

[39] W. D. Bachalo and D. A. Johnson, "Transonic, turbulent boundary-layer separation generated on an axisymmetric flow model," *AIAA Journal*, vol. 24, no. 3, pp. 437–443, Mar. 1986, doi: 10.2514/3.9286.

[40] H. Raiesi, U. Piomelli, and A. Pollard, "Evaluation of Turbulence Models Using Direct Numerical and Large-Eddy Simulation Data," *Journal of Fluids Engineering*, vol. 133, p. 021203, Feb. 2011, doi: 10.1115/1.4003425.

[41] J. Klinner, M. Schroll, C. Morsbach, F. Möller, and C. Willert, "Experimental and numerical investigation of 3-D corner separation in a channel flow with adverse pressure gradient," in *21st STAB/DGLR Symposium on New Results in Numerical and Experimental Fluid Mechanics*, Darmstadt, Nov. 2018, vol. 12, no. 142, pp. 663–673.

[42] E. M. Cherry, C. J. Elkins, and J. K. Eaton, "Geometric sensitivity of three-dimensional separated flows," *International Journal of Heat and Fluid Flow*, vol. 29, no. 3, pp. 803–811, Jun. 2008, doi: 10.1016/j.ijheatfluidflow.2008.01.018.

[43] E. M. Cherry, C. J. Elkins, and J. K. Eaton, "Pressure measurements in a three-dimensional separated diffuser," *International Journal of Heat and Fluid Flow*, vol. 30, no. 1, pp. 1–2, Feb. 2009, doi: 10.1016/j.ijheatfluidflow.2008.10.003.

[44] J. S. Chow, G. G. Zilliac, and P. Bradshaw, "Mean and Turbulence Measurements in the Near Field of a Wingtip Vortex," *AIAA Journal*, vol. 35, no. 10, pp. 1561–1567, Oct. 1997, doi: 10.2514/2.1.

[45] Hartley, C.D, "'Measurement of flow velocities within a hydrocyclone using laser doppler anemometry." Technical Report FTN/X/82, AEA, Power Fluidics, BNFL, 1994.

[46] D. Greenblatt, K. B. Paschal, C.-S. Yao, J. Harris, N. W. Schaeffler, and A. E. Washburn, "Experimental Investigation of Separation Control Part 1: Baseline and Steady Suction," *AIAA Journal*, vol. 44, no. 12, pp. 2820–2830, Dec. 2006, doi: 10.2514/1.13817.

[47] D. Greenblatt, K. B. Paschal, C.-S. Yao, and J. Harris, "Experimental Investigation of Separation Control Part 2: Zero Mass-Flux Oscillatory Blowing," *AIAA Journal*, vol. 44, no. 12, pp. 2831–2845, 2006, doi: 10.2514/1.19324.

[48] J. W. Naughton, S. Viken, and D. Greenblatt, "Skin Friction Measurements on the NASA Hump Model," *AIAA Journal*, vol. 44, no. 6, pp. 1255–1265, 2006, doi: 10.2514/1.14192.

[49] C. L. Rumsey, "Exploring a Method for Improving Turbulent Separated-Flow Predictions with k-ω Models," NASA/TM–2009–215952, 2009.

[50] J. W. Baughn, A. E. Hechanova, and X. Yan, "An experimental study of entrainment effects on the heat transfer from a flat surface to a heated circular impinging jet," *Journal of Heat Transfer*, vol. 113:4, Nov. 1991, doi: 10.1115/1.2911197.

[51] R. E. Uittenbogaard, "Stably Stratified Mixing Layer." IAHR Working Group on Rfeined Flow Modelling, 1989.

[52] F. R. Menter, "Influence of freestream values on k-omega turbulence model predictions," *AIAA Journal*, vol. 30, no. 6, pp. 1657–1659, 1992, doi: 10.2514/3.11115.

[53] P. R. Spalart, "Strategies for turbulence modelling and simulations," *International Journal of Heat and Fluid Flow*, vol. 21, no. 3, pp. 252–263, Jun. 2000, doi: 10.1016/S0142-727X(00)00007-2.

[54] S. Obi, K. Aoki, and S. Masuda, "Experimental and Computational Study of Turbulent Separating Flow in an Asymmetric Plane Diffuser," *Ninth Symposium on "Turbulent Shear Flows", Kyoto, Japan*, p. 5.

[55] H. Grotjans and F. R. Menter, "Wall Functions for General Application CFD Codes."

[56] B. E. Launder and B. I. Sharma, "Application of the Energy-Dissipation Model of Turbulence to Calculation of Flow Near a Spinning Disc," *Lett. Heat and Mass Transfer 1*, vol. 1, no. 2, p. 8, 1974.

[57] K.-Y. Chien, "Predictions of Channel and Boundary-Layer Flows with a Low-Reynolds-Number Turbulence Model," *AIAA Journal*, vol. 20, no. 1, pp. 33–38, Jan. 1982, doi: 10.2514/3.51043.

[58] M. Wolfshtein, "The velocity and temperature distribution in one-dimensional flow with turbulence augmentation and pressure gradient," *International Journal of Heat and Mass Transfer*, vol. 12, no. 3, pp. 301–318, Mar. 1969, doi: 10.1016/0017-9310(69)90012-X.

[59] P. A. Durbin, "Near-wall turbulence closure modeling without 'damping functions,'" *Theoret. Comput. Fluid Dynamics*, vol. 3, no. 1, pp. 1–13, Sep. 1991, doi: 10.1007/BF00271513.

# 9. Appendix A: Theory

## 9.1. The Closure Problem

For a detailed discussion of the derivation of turbulence equations please consult one of the available text books ([2]–[7]). In this section only a very basic model descriptions will be provided to allow the connection between the Best Practice discussions and the turbulence model formulations.

### 9.1.1. Averaging

Due to the high cost of DNS, the engineering approach to CFD lies in the Reynolds-Averaged Navier-Stokes (RANS) equations. These equations are obtained from the exact Navier-Stokes equations through time (or ensemble) averaging.

Time averaging is defined by:

$$\phi(x_i, t) = \bar{\phi}(x) + \phi'(x_i, t) \tag{9.1}$$

$$\bar{\phi} = \lim_{T \to \infty} \frac{1}{T} \int_0^T \phi(x_i, t) dt \tag{9.2}$$

In other words, the instantaneous quantity $\phi(x_i, t)$ is split into a time-mean value $\bar{\phi}(x)$ and a fluctuating part $\phi'(x_i, t)$. The simulation is then only concerned with the time-mean part. More generally, one can also perform an ensemble-averaging over many instances of an experiment:

Ensemble averaging is defined by:

$$\phi(x_i, t) = \bar{\phi}(x, t) + \varphi'(x_i, t) \tag{9.3}$$

$$\bar{\phi}(x, t) = \lim_{T \to \infty} \frac{1}{N} \sum_1^N \phi(x_i, t) \tag{9.4}$$

The advantage of ensemble averaging is that it can also be applied to inherently unsteady flows (e.g. the flow in an internal combustion engine with moving parts). Both forms of averaging lead to the same equations and turbulence models, so the same overbar is used for simplicity.

When these averaging processes are applied to the Navier-Stokes equations, one obtains the RANS momentum equations:

$$\frac{\partial(\rho \bar{U}_i)}{\partial t} + \frac{\partial(\rho \bar{U}_i \bar{U}_j)}{\partial x_j} = -\frac{\partial \bar{p}}{\partial x_i} + \frac{\partial}{\partial x_j}\left(\tau_{ij} - \rho \overline{u'_i u'_j}\right) \tag{9.5}$$

where $\bar{U}_i$ is the vector of the averaged velocity field, $\rho$ is the density (assumed constant in this brief overview), $\bar{p}$ is the averaged pressure and $\tau_{ij}$ is the Stokes (laminar) stress tensor. For incompressible flows:

$$\tau_{ij} = \mu\left(\frac{\partial \bar{U}_i}{\partial x_j} + \frac{\partial \bar{U}_j}{\partial x_i}\right) \equiv \mu 2 S_{ij} \tag{9.6}$$

with $\mu$ being the dynamic molecular viscosity.

The last term in the above equation $-\rho \overline{u'_i u'_j}$ is so-called 'Reynolds Stress Tensor' and results from the averaging of the non-linear convection terms. This tensor represents the influence of the turbulent fluctuations on the mean velocity field. The above momentum equations are 'unclosed' as no equations are yet available for the Reynolds Stress Tensor. Turbulence models are needed to provide formulations for this tensor.

The RANS momentum equations above are derived under the assumption that there are no significant density variations due to turbulence – this is typically the case for flows with Mach numbers below M < 3. Note that density variations on the mean flow occur much earlier, starting as low as M~0.1.

### 9.1.2. The Eddy-Viscosity Assumption

The most widely applied assumption in turbulence modeling is the eddy-viscosity assumption. It is based on the concept that turbulent stresses can be represented in a similar fashion as the laminar stress tensor:

$$-\rho \overline{u'_i u'_j} = \mu_t \left( \frac{\partial \overline{U}_i}{\partial x_j} + \frac{\partial \overline{U}_j}{\partial x_i} \right) - \frac{2}{3} \rho k \delta_{ij} \tag{9.7}$$

The last term on the right represents the turbulence kinetic energy, *k*, and accounts for the requirement that the sum of the diagonals of the Reynolds Stress Tensor must amount to *2k*. This term is not essential and can be avoided/ignored (e.g. in one-equation models where *k* is not available).

The original problem of providing closure equations for the six (due to symmetry of the tensor) unknowns of the Reynolds Stress Tensor is thereby now reduced to providing a suitable eddy-viscosity $\mu_t$ (also called turbulent viscosity). It is important to note that $\mu_t$ is not a property of the fluid, but a property of the local turbulence. The eddy-viscosity has dimension:

$$\mu_t = \rho \nu_t \sim \rho \frac{L_t^2}{T_t} \tag{9.8}$$

where $L_t$ and $T_t$ are the length- and time-scales of turbulence, respectively.

### 9.1.3. Reynolds Stress Modeling (RSM)

Contrary to the eddy-viscosity assumption, there are methods, which aim at computing the individual Reynolds Stresses individually. For this purpose, exact transport equations for each Reynolds Stress are derived (6 equations). These exact equations, however, contain again new unknown terms which need to be modeled (see e.g. [5]). Different modeling assumptions for these terms then leads to a large variety of Reynolds Stress Models (RSM). The exact RSM equations read:

$$\frac{\partial \rho \overline{u'_i u'_j}}{\partial t} + \frac{\partial \rho \overline{U}_k \overline{u'_i u'_j}}{\partial x_k} = -\overline{u'_i u'}_k \frac{\partial \rho \overline{U}_j}{\partial x_k} - \overline{u'_j u'}_k \frac{\partial \rho \overline{U}_i}{\partial x_k}$$
$$+ \overline{p' \left( \frac{\partial u'_i}{\partial x_j} + \frac{\partial u'_j}{\partial x_i} \right)} - 2\mu \overline{\frac{\partial u'_i}{\partial x_x} \frac{\partial u'_j}{\partial x_x}} \tag{9.9}$$
$$- \frac{\partial}{\partial x_k} \left[ \rho \overline{u'_i u'_j u'}_k + \overline{p' u'_j} \delta_{ik} + \overline{p p' u'_i} \delta_{jk} \right] + \mu \frac{\partial^2 \overline{u'_i u'_j}}{\partial x_k^2}$$

The terms in these equations are Line 1: time derivative, convection, production. Line 2: pressure strain (PS), dissipation. Line 3: turbulent diffusion and molecular diffusion. All terms in Line 1 are exact and need no modeling. This is true also for the last term in Line 3. All other terms require models to close the equations. In addition, there is a need for information on the turbulent scale required e.g. in the dissipation term. This information is typically obtained from an additional transport equation (e.g. $\varepsilon$-equation or $\omega$-equation). All in all, RSM closure therefore requires the

solution of seven additional equations. Proposed RSM differ mostly by the way they model the pressure-strain term.

### 9.1.4. Explicit Algebraic Reynolds Stress Modeling (EARSM)

Simplified versions of RSM models can be obtained where the Reynolds stresses are computed from algebraic formulations instead of transport equations. Such models are generically of the form:

$$-\rho \overline{u'_i u'_j} = F\big(\bar{S}_{ij}, \overline{W}_{ij}, k, \omega\big) \tag{9.10}$$

with

$$\bar{S}_{ij} = \frac{1}{2}\left(\frac{\partial \overline{U}_i}{\partial x_j} + \frac{\partial \overline{U}_j}{\partial x_i}\right), \quad \overline{W}_{ij} = \frac{1}{2}\left(\frac{\partial \overline{U}_i}{\partial x_j} - \frac{\partial \overline{U}_j}{\partial x_i}\right) \tag{9.11}$$

and $k$ being the turbulence kinetic energy and $\omega$ a turbulent frequency scale. Note that the eddy-viscosity formulation (Eq. (9.7)) is the simplest form of such a model. The main model in Ansys CFD is a version of Wallin-Johansson [19].

### 9.1.5. The Equation for the Turbulence kinetic Energy

All industrial relevant two-equation models use the equation for the turbulence kinetic energy, $k$, to provide one of the two scales required. The $k$-equation can be derived by summing up half of the diagonal of the exact RSM equations (Eq.(9.9)).

$$\frac{\partial(\rho k)}{\partial t} + \frac{\partial(\rho \overline{U}_j k)}{\partial x_j} = P_k - \rho \varepsilon + D^{(k)} + \frac{\partial}{\partial x_j}\left(\mu \frac{\partial k}{\partial x_j}\right) \tag{9.12}$$

with:

$$P_k \equiv -\rho \overline{u_j' u_i'} \frac{\partial(\overline{U}_i)}{\partial x_j} \tag{9.13}$$

$$\rho \varepsilon \equiv \mu \overline{\frac{\partial u_i'}{\partial x_j} \frac{\partial u_i'}{\partial x_j}} \tag{9.14}$$

$$D^{(k)} \equiv -\frac{\partial\left(\overline{u_i' p'} + 0.5\rho \overline{u_i' u_j' u_j'}\right)}{\partial x_i} \tag{9.15}$$

The term $P_k$ is the production term. When inserting the eddy-viscosity formulation (Equation (9.7)) it can be formulated as:

$$P_k = \mu_t \bar{S}^2 \tag{9.16}$$

with $\bar{S}^2 = 2\bar{S}_{ij}\bar{S}_{ij}$.

The term $\varepsilon$ is the turbulence energy dissipation rate, which converts turbulence kinetic energy into heat (typically small enough to be neglected in the overall energy balance).

The term $D^{(k)}$ is called turbulent diffusion. In an integral sense, it does not contribute to the overall production or dissipation of turbulence kinetic energy, but does only smooths out the $k$-distribution. It is typically modeled by a simple gradient-diffusion hypothesis:

$$D^{(k)} \approx \frac{\partial}{\partial x_j}\left(\frac{\mu_t}{\sigma_k}\frac{\partial k}{\partial x_j}\right)$$

(9.17)

The modeled $k$-equation therefore reads:

$$\frac{\partial(\rho k)}{\partial t} + \frac{\partial(\rho \overline{U}_j k)}{\partial x_j} = P_k - \rho\varepsilon + \frac{\partial}{\partial x_j}\left(\left(\mu + \frac{\mu_t}{\sigma_k}\right)\frac{\partial k}{\partial x_j}\right)$$

(9.18)

With these formulations, the only term missing (unclosed) in the $k$-equation is the dissipation term $\varepsilon$. It needs to be provided from a separate scale-equation (e.g. the $\varepsilon$-equation or the $\omega$-equation with $\varepsilon = C_\mu k\omega$).

### 9.1.6. The Turbulence Scale-Equation

What is meant by 'turbulent scales' in the context of RANS modeling? As discussed in the introduction, turbulence consists of a spectrum of scales – so identifying a single length- or time-scale is not trivial. However, the mixing processes which are of foremost engineering interest are driven by the largest scales of turbulence.

The derivation of the scale equation (typically $\varepsilon$ or $\omega$) is one of the weakest steps in RANS modeling. While exact transport equations can be derived e.g. for $\varepsilon$, such equations represent the small scales of turbulence (where dissipation takes place) and do not provide information on the large scales required in RANS closure. One could argue that in RANS $\varepsilon$ is not trying to model 'dissipation' but rather the destruction of large scales into smaller scales – which are no longer relevant for the mixing processes.

To arrive at a suitable model equation, the assumption is made that the scale equation has a form similar to the $k$-equation:

$$\frac{\partial(\rho\varepsilon)}{\partial t} + \frac{\partial(\rho\overline{U}_j\varepsilon)}{\partial x_j} = C_{\varepsilon1}\frac{\varepsilon}{k}P_k - \rho C_{\varepsilon2}\frac{\varepsilon}{k}\varepsilon + \frac{\partial}{\partial x_j}\left(\left(\mu + \frac{\mu_t}{\sigma_\varepsilon}\right)\frac{\partial\varepsilon}{\partial x_j}\right)$$

(9.19)

with the ratio $\varepsilon/k$ introduced for dimensional correctness. The coefficients $C_{\varepsilon1}, C_{\varepsilon2}, \sigma_\varepsilon$ are model coefficients which need to be tuned by experimental data. The coefficients of the standard k-$\varepsilon$ model are:

| $C_{\varepsilon1}$ | $C_{\varepsilon2}$ | $\sigma_k$ | $\sigma_\varepsilon$ | $C_\mu$ |
|---|---|---|---|---|
| 1.44 | 1.92 | 1.0 | 1.3 | 0.09 |

**Table 4: Coefficients for the standard $k$-$\varepsilon$ model (see e.g. [7]).**

An equation for the turbulent frequency, $\omega$, can be derived with the same arguments:

$$\frac{\partial(\rho\omega)}{\partial t} + \frac{\partial(\rho\overline{U}_j\omega)}{\partial x_j} = C_{\omega1}\frac{\omega}{k}P_k - \rho C_{\omega2}\omega^2 + \frac{\partial}{\partial x_j}\left(\left(\mu + \frac{\mu_t}{\sigma_\omega}\right)\frac{\partial\omega}{\partial x_j}\right)$$

(9.20)

With this set of equations, the eddy-viscosity can be computed:

$$\mu_t = C_\mu \rho \frac{k^2}{\varepsilon} = \rho \frac{k}{\omega} \tag{9.21}$$

using $\varepsilon = C_\mu k \omega$.

| $C_{\omega 1}$ | $C_{\omega 2}$ | $\sigma_k$ | $\sigma_\omega$ | $C_\mu$ |
|:---:|:---:|:---:|:---:|:---:|
| 5/9 | 3/40 | 2 | 2 | 0.09 |

**Table 5: Coefficients standard $k$-$\omega$ model (see e.g. [7])**

Since $\varepsilon$ and $\omega$ are related, one can investigate the differences between the $\varepsilon$- and the $\omega$-equations. This can be achieved e.g. by transforming the exact $\varepsilon$-equation to an $\omega$-equation. Assuming for simplicity $\sigma_k = \sigma_\varepsilon = \sigma_\omega$ one gets:

$$\frac{\partial(\rho\omega)}{\partial t} + \frac{\partial(\rho\overline{U}_j\omega)}{\partial x_j} = C_{\omega 1}\frac{\omega}{k}P_k - \rho C_{\omega 2}\omega^2 + CD + \frac{\partial}{\partial x_j}\left(\left(\mu + \frac{\mu_t}{\sigma_\omega}\right)\frac{\partial\omega}{\partial x_j}\right) \tag{9.22}$$

With the cross-diffusion term:

$$CD = \rho\frac{2}{\sigma_\omega}\frac{1}{\omega}\frac{\partial k}{\partial x_j}\frac{\partial\omega}{\partial x_j} \tag{9.23}$$

The transformation of the coefficients gives the relation:

$$C_{\omega 1} = C_{\varepsilon 1} - 1; \quad C_{\omega 2} = C_\mu(C_{\varepsilon 2} - 1) \tag{9.24}$$

In other words, the $\omega$-equation when derived on the same dimensional arguments as the $\varepsilon$-equation results in Equation ((9.20), whereas the transformation of the $\varepsilon$-equation into a $\omega$-equation gives Equation (9.22). The difference lies mainly in the cross-diffusion term $CD$.

What is the effect of the CD term? There are two main effects, one positive and one negative. The negative effect is discussed in detail by Wilcox [7] and is manifested in an improved performance of the $\omega$-equation based models not utilizing the CD term in adverse pressure gradient boundary layers. Such models predict an improved response to the pressure gradient and a higher sensitivity to predict flow separation, compared with $\varepsilon$-equation based models. In other words, the inclusion of the $CD$ term in the $\omega$-equation in the near wall region would inhibit correct separation prediction.

The second effect of including the $CD$ is desirable, as it avoids the strong sensitivity of the standard $\omega$-equation (models without $CD$) based model to freestream values. As discussed in detail in [52] the standard model produces a wide variation in results in case the level of $\omega$ changes outside the boundary or free shear layer (freestream). This is illustrated in Figure 98 for a mixing layer. The left part of the Figures shows the reaction of the Wilcox $k$-$\omega$ model to changes in freestream $\omega$ on the velocity profile and the right part shows the same test using the GEKO $k$-$\omega$ model (which includes the CD term). Figure 99 shows the same effect on the eddy-viscosity profiles, where the difference in the standard $k$-$\omega$ model is more than a factor two between the low and the high freestream values. Since the level of freestream values cannot easily be controlled and is often based on roughly estimated inlet values, solution independence from these values is essential for reliable simulations.
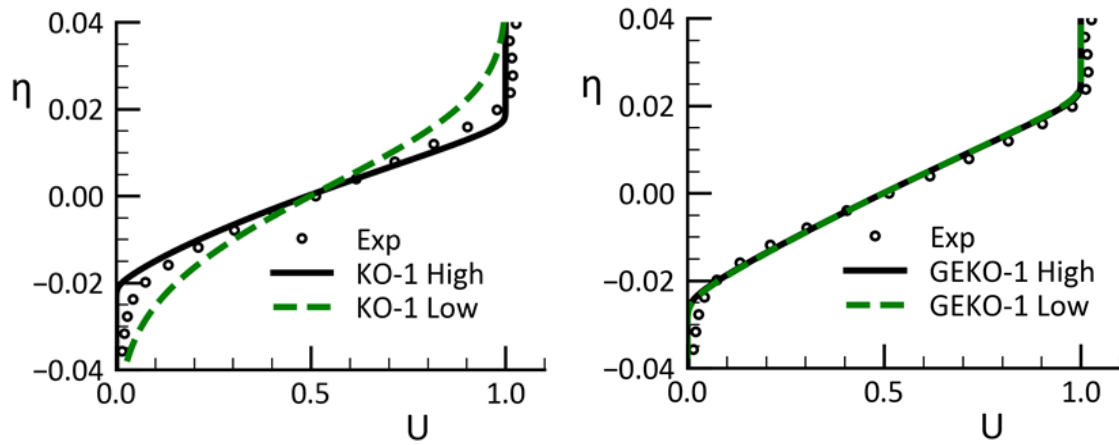
**Figure 98: Effect of freestream $\omega$-levels on velocity profile for free mixing layer solution. Left: standard $k$-$\omega$ model without CD term. Right: GEKO model including CD term.**
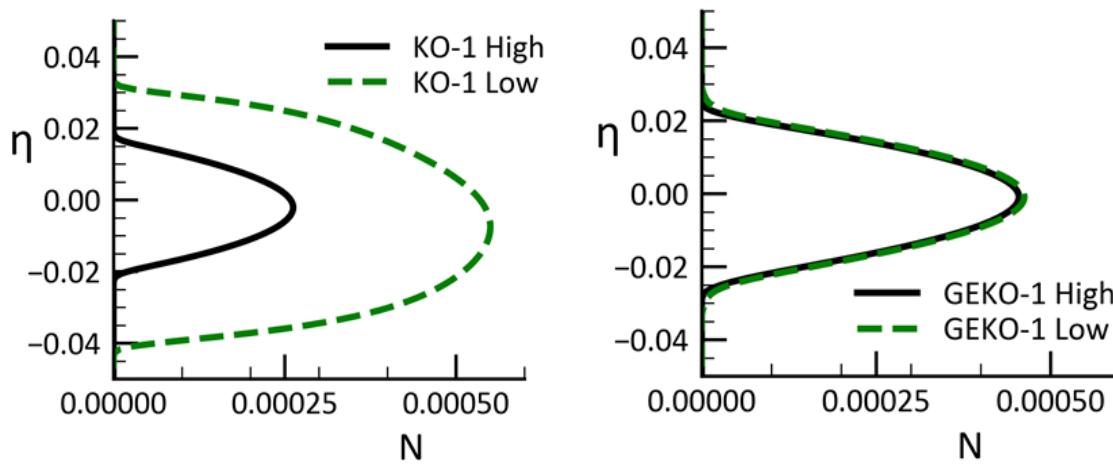


**Figure 99: Effect of freestream $\omega$-levels on non-dimensional eddy-viscosity profiles for free mixing layer solution. Left: standard $k$-$\omega$ model without CD term. Right: GEKO model including CD term.**

The equations discussed so far form the basis of all industrially $\varepsilon$- and $\omega$-based turbulence models.

## 9.2. Two-Equation Models

The motivation behind two-equation models originates from the need to obtain the two scales required to compute the eddy-viscosity. Based on dimensional arguments, a length-scale, $L_t$, and a time-scale, $T_t$, are required for that purpose. Note that any two other scales are equivalent as there are only two independent mechanical scales. These requirements naturally lead to two-equation models as a basis for providing these scales. However, two-equation models also form the basis for all further developments, like One-equation models, Reynolds Stress Models (RSM) or Explicit Algebraic Reynolds Stress models (EARSM). Two-equation models are also the optimal platform for including additional physics, like laminar-turbulent transition, rough walls, buoyancy, as well as hybrid RANS-LES concepts.

Two-equation models are composed of the following elements:

- Turbulence kinetic energy equation
- Scale equation ($\varepsilon$ or $\omega$)
- Eddy-viscosity formulation
- Near-wall treatment
- Limiters

Each one of these elements can have a substantial influence of accuracy and robustness of the simulations.

## 9.2.1. The $k$-$\omega$ Models

### *The BSL/SST Models*

Based on the investigation of the freestream dependency of the Wilcox model [52], Menter proposed model formulations which are composed of a blend of $k$-$\varepsilon$ and $k$-$\omega$ model elements [17]. As discussed in Section 9.2.2, the main difference between these models is the cross-diffusion term (CD) which appears when transforming the $k$-$\varepsilon$ model to a $k$-$\omega$ model. This term avoids the freestream sensitivity near the shear/boundary layer edge. However, while it is desirable to include the term near the shear/boundary layer edge, it is not desirable to activate it near the wall, as it negatively affects the adverse pressure gradient behavior of the model. The BSL model was therefore built on the blending function $F_1$, which is based on wall distance, $y$. The function has a value of $F_1=1$ inside the wall boundary layer and gradually blends to $F_1=0$ in the outer part of the boundary layer and beyond. This function blends the CD term into the $\omega$-equation but also blends the coefficients from those of the $k$-$\omega$ to those of the $k$-$\varepsilon$ model.

$$\frac{\partial(\rho k)}{\partial t} + \frac{\partial(\rho U_j k)}{\partial x_j} = P_k - C_\mu \rho k\omega + \frac{\partial}{\partial x_j}\left[\left(\mu + \frac{\mu_t}{\sigma_k}\right)\frac{\partial k}{\partial x_j}\right] \tag{9.25}$$

$$\frac{\partial(\rho\omega)}{\partial t} + \frac{\partial(\rho U_j\omega)}{\partial x_j} = C_{\omega 1}\frac{\omega}{k}P_k - C_{\omega 2}\rho\omega^2 + \rho(1-F_1)CD + \frac{\partial}{\partial x_j}\left[\left(\mu + \frac{\mu_t}{\sigma_\omega}\right)\frac{\partial\omega}{\partial x_j}\right] \tag{9.26}$$

$$\mu_t = \rho\nu_t = \rho\frac{k}{max(\omega, F_2 S/a_1)} \tag{9.27}$$

$$CD = \frac{2}{\sigma_\omega}\frac{1}{\omega}\frac{\partial k}{\partial x_j}\frac{\partial\omega}{\partial x_j} \tag{9.28}$$

$$Coef = (1-F_1)Coef_{k-\omega} + F_1 Coef_{k-\varepsilon} \tag{9.29}$$

| BSL | $C_{\omega 1}$ | $C_{\omega 2}$ | $\sigma_k$ | $\sigma_\omega$ | $C_\mu$ | $a_1$ |
|---|---|---|---|---|---|---|
| Coef $_{k-\omega}$ | 5/9 | 3/40 | 2 | 2 | 0.09 | ∞ |
| Coef $_{k-\varepsilon}$ | 0.44 | 0.0828 | 1 | 1.17 | 0.09 | ∞ |

**Table 6: Coefficients of BSL model.**

| SST | $C_{\omega 1}$ | $C_{\omega 2}$ | $\sigma_k$ | $\sigma_\omega$ | $C_\mu$ | $a_1$ |
|---|---|---|---|---|---|---|
| Coef $_{k-\omega}$ | 5/9 | 3/40 | 1/0.85 | 2 | 0.09 | 0.31 |
| Coef $_{k-\varepsilon}$ | 0.44 | 0.0828 | 1 | 1.17 | 0.09 | 0.31 |

**Table 7: Coefficients of SST model.**

There are two model variants. The BSL (baseline model) and the SST (Shear Stress Transport) model. The SST model is based on the BSL model, but in addition limits the eddy-viscosity inside the boundary layer (using a second blending function $F_2$) to achieve improved model performance for flows under adverse pressure gradients and separation.

The two blending functions $F_1$ and $F_2$ read:

$$arg_1 = min\left[max\left(\frac{\sqrt{k}}{0.09\omega y}; \frac{500\nu}{\omega y^2}\right); \frac{4\rho\sigma_{\omega 2}k}{max(CD, 10^{-20})y^2}\right]$$
$$F_1 = tanh(arg_1^4)$$

(9.30)

$$arg_2 = max\left(2\frac{\sqrt{k}}{0.09\omega y}; \frac{500\nu}{\omega y^2}\right)$$
$$F_2 = tanh(arg_2^2)$$

(9.31)

The BSL model can also be used as the basis for combination with EARSM and RSM models - where the limiter on the eddy-viscosity is not required, as improved stress prediction is achieved through the EARSM/RSM formulation. The SST model on the other hand is calibrated for accurate prediction of separation and aerodynamic flows when used as an eddy-viscosity model.

There is a clear increase in complexity from the Wilcox model to the BSL/SST models, mainly through the need for blending functions, which in turn require the wall-distance. Wall-distance is not problematic if the mesh/geometry are fixed (as is the case in most CFD simulations). In case of varying mesh/geometry however, the wall distance computation can become expensive as it needs to be repeated for every time-step. Particularly for massively parallel simulations, the wall distance computation can dominate the CPU costs as the algebraic operation does not scale well on such machines. The GEKO model (Section 3.3.2) has therefore been developed with an option avoiding the wall distance.

The SST model allows variation of the $a_1$ coefficient without affecting the calibration of the logarithmic layer. Its value can be increased, thereby reducing the sensitivity to adverse pressure gradient flows and delaying/reducing flow separation. The value cannot be decreased however, as that would interfere with the log-law behavior and would thereby negatively affect the flat plat calibration.

*The Generalized k-ω model (GEKO)*

The main characteristics of the GEKO model is that it has several free parameters for tuning the model to different flow scenarios. The starting point for the formulation is:

$$\frac{\partial(\rho k)}{\partial t} + \frac{\partial(\rho U_j k)}{\partial x_j} = P_k - C_\mu \rho k\omega + \frac{\partial}{\partial x_j}\left[\left(\mu + \frac{\mu_t}{\sigma_k}\right)\frac{\partial k}{\partial x_j}\right]$$

(9.32)

$$\frac{\partial(\rho\omega)}{\partial t} + \frac{\partial(\rho U_j\omega)}{\partial x_j} = C_{\omega 1}\frac{\omega}{k}P_k - C_{\omega 2}\rho\omega^2 + \rho C_{\omega 3}CD + \frac{\partial}{\partial x_j}\left[\left(\mu + \frac{\mu_t}{\sigma_\omega}\right)\frac{\partial\omega}{\partial x_j}\right]$$

(9.33)

$$\mu_t = \rho\nu_t = \rho\frac{k}{max(\omega, S/C_{Realize})}$$

(9.34)

$$P_k = -\tau_{ij}\frac{\partial U_i}{\partial x_j}$$

(9.35)

$$\tau_{ij} = -\rho\overline{u_i'u_j'} = \mu_t 2S_{ij} - \frac{2}{3}\rho k\delta_{ij}$$

(9.36)

$$CD = \frac{2}{\sigma_\omega}\frac{1}{\omega}\frac{\partial k}{\partial x_j}\frac{\partial\omega}{\partial x_j}$$

(9.37)

There is a provision for corner flows which amounts to adding a quadratic term to the stress-strain relation. The terms is essentially the same as the Quadratic Closure Relation (QCR) proposed by Spalart [53]:

$$\tau_{ij} = -\rho \overline{u_i' u_j'} = \mu_t 2 S_{ij} - \frac{2}{3} \rho k \delta_{ij}$$
$$- C_{CORNER} \frac{1.2\, n_t}{max\left(0.3\omega, \sqrt{(S^2 + W^2)/2}\right)} \left(S_{ik} W_{kj} - W_{ik} S_{kj}\right)$$
(9.38)

$$S_{i,j} = \frac{1}{2}\left(\frac{\partial U_i}{\partial x_j} + \frac{\partial U_j}{\partial x_i} - \frac{2}{3}\frac{\partial U_k}{\partial x_k}\delta_{ij}\right); \quad W_{i,j} = \frac{1}{2}\left(\frac{\partial U_i}{\partial x_j} - \frac{\partial U_j}{\partial x_i}\right)$$

The GEKO model formulation is otherwise conventional, it involves the cross-diffusion term which typically is derived from a transformation of the $k$-$\varepsilon$ model to a $k$-$\omega$. This term is included in most of the more recent $k$-$\omega$ models in various ways. It is generally understood that this term is required at the edge of turbulent layers to maintain the $k$-$\varepsilon$ model behavior and avoid freestream sensitivities.

The main difference of GEKO to existing models is the introduction of free parameters which can be tuned by the user to achieve different goals in different parts of the simulation domain. The details of the GEKO model formulation are not published at this point, but the effect of the free parameters will be described. Note that an entire 'Best Practice Guide' exists for the GEKO model [1].

Currently there are the following parameters included for tuning:
- $C_{SEP}$ – Parameter to optimize flow separation from smooth surfaces
- $C_{NW}$ – Parameter to optimize flow in non-equilibrium near wall regions (heat transfer, $C_f$, ….)
- $C_{MIX}$ – Parameter to optimize strength of mixing in free shear flows
- $C_{JET}$ – Parameter to optimize free shear layer mixing (optimize free jets independent of mixing layer)
- $C_{CC}$ – Parameter to optimize flows with streamline curvature and rotation
- $C_{CORNER}$ – Parameter to optimize anisotropic flow in corners

All these parameters are designed so that they do not negatively affect the basic model calibration for flat plate flows. In other words, the logarithmic layer formulation is preserved despite the changes in these parameters. Note that the two last parameters can also be combined with other $k$-$\omega$ models.

All parameters (except $C_{JET}$) are available through User Defined Functions (UDF) access. This means that they can be defined either with a global value (in the GUI/TUI) or as zonal/local values via UDFs.

The function $F_{Mix}$ is defined using the blending function $F_{Blend}$:

$$F_{Mix} = 1 + C_{Mix} F(C_{JET})(1 - F_{Blend})$$
(9.39)

Inside wall boundary layers, the term is de-activated ($F_{Blen\,d} = 1$) to ensure that the $C_{MIX}/C_{JET}$ coefficient only affects free shear flows. It is also seen, that the coefficient $C_{JET}$ only affects the impact of $C_{MIX}$ (e.g. in case $C_{MIX} = 0$ also $C_{JET}$ has no effect). $C_{JET}$ essentially reduced the impact of $C_{MIX}$ on jet flows (where $C_{MIX}$ would otherwise cause an over-prediction of jet spreading rates).

Figure 100 shows the function $F_{Blend}$ for a NACA 4412 airfoil at $\alpha = 12°$ angle of attack. The function is $F_{Blend} = 1$ (red) inside the boundary layer and $F_{Blend} = 0$ (blue) away from the wall. Especially at the trailing edge, where the wake (free shear flow) leaves the wall (boundary layer) the function switches swiftly to activate the $C_{MIX}$-term
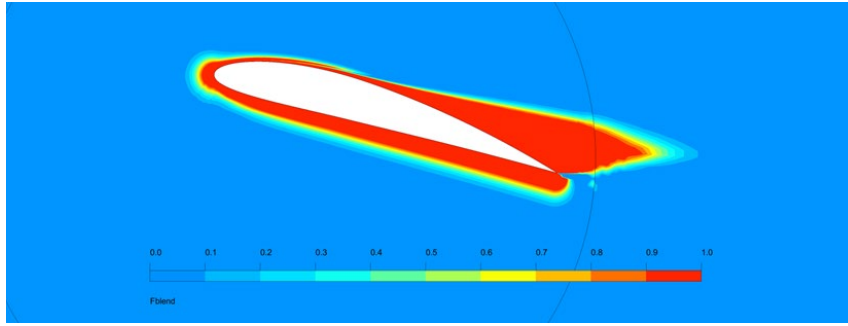
**Figure 100: Blending function F_Blend for introducing additional mixing trough coefficients C_MIX/C_JET.**

The free coefficients should be in the range:

$$0.7 \leq \quad C_{SEP} \quad \leq 2.5$$
$$0.0 \leq \quad C_{MIX} \quad \leq 1.0 \ldots$$
$$-2.0 \leq \quad C_{NW} \quad \leq 2.0$$
$$0.0 \leq \quad C_{JET} \quad \leq 1.0$$

The main tuning parameter for the GEKO model is the coefficient $C_{SEP}$. When increasing $C_{SEP}$, boundary layer separation will be predicted more aggressively. However, in addition, the spreading rates of all free shear flows will be affected by changes in $C_{SEP}$ as it generally decreases the eddy-viscosity level in the entire domain. This is not convenient for users, as they would have to tune two parameters simultaneously. To maintain the spreading rate for the most important free shear flow, namely the mixing layer, while changing $C_{SEP}$, a correlation was developed, which maintains the mixing layer spreading rates under changes of $C_{SEP}$:

$$\Delta C_{SEP} = C_{Sep} - 1$$
$$C_{MixCor} = 0.35 \cdot sign(\Delta C_{SEP}) \cdot \sqrt{|\Delta C_{SEP}|} \tag{9.40}$$

This correlation is set as default – however users can also optimize $C_{MIX}$ by hand, independently of $C_{SEP}$.

The parameter $C_{JET}$ is designed to reduce the spreading rate for round jets, which is over-predicted with all conventional turbulence models. To achieve optimal performance for round jets, one needs to set $C_{SEP}$ to values $C_{SEP}$~1.75-2.00 and $C_{JET}$=0.9 (default). With reduction in $C_{SEP}$ and the corresponding reduction in $C_{MIX}$, the effect of $C_{JET}$ vanishes (see [9].). There is another parameter CJET_AUX which also has an influence on the jet flow. It defines the limit between mixing layers and jet flows. The larger the value, the sharper the 'demarcation' and stronger the effect of $C_{JET}$. The default value is CJET_AUX =2.0. It is suitable for jet flow simulations to set the value to CJET_AUX =4.0. This is not done by default, as it can lead to oscillations on poor meshes. For more details and test cases, see the Best Practice Guidelines for the GEKO model [9].

At first, the versatility of the model seems to pose a challenge to the user as to the optimal selection of coefficients. However, there are strong defaults and there are certain combinations of coefficients, which can be applied to most flows, so that the user would only interfere on specific cases, where the model does not lead to satisfactory results. The selection of $C_{SEP} = C_{NW} = 1$ results in an exact transformation to the $k$-$\varepsilon$ model, albeit with improved sub-layer treatment and limiters activated.

### 9.2.2. The $k$-$\varepsilon$ Models

*The Standard $k$-$\varepsilon$ -Model*

To explain the preference for $\omega$-equation based models, it is important to critically discuss the $\varepsilon$-equation. It needs to be emphasized that the $\varepsilon$-equation has been used in many CFD simulations in the past which is a clear indication that the issues discussed below are not present in all or even the majority of $\varepsilon$-equation model simulations. However, these deficiencies are frequent enough to preclude the $\varepsilon$-equation as a turbulence model integration platform.

The standard $k$-$\varepsilon$ model without a Viscous Sublayer Model (VSM) terms is given by:

$$\frac{\partial(\rho k)}{\partial t} + \frac{\partial(\rho U_j k)}{\partial x_j} = P_k - \rho\varepsilon + \frac{\partial}{\partial x_j}\left[\left(\mu + \frac{\mu_t}{\sigma_k}\right)\frac{\partial k}{\partial x_j}\right] \tag{9.41}$$

$$\frac{\partial(\rho\varepsilon)}{\partial t} + \frac{\partial(\rho U_j\varepsilon)}{\partial x_j} = C_{\varepsilon 1}\frac{\varepsilon}{k}P_k - C_{\varepsilon 2}\rho\frac{\varepsilon}{k}\varepsilon + \frac{\partial}{\partial x_j}\left[\left(\mu + \frac{\mu_t}{\sigma_\varepsilon}\right)\frac{\partial\varepsilon}{\partial x_j}\right] \tag{9.42}$$

$$\mu_t = C_\mu\rho\frac{k^2}{\varepsilon}, \qquad P_k = \tau_{ij}\frac{\partial U_i}{\partial x_j}, \quad \tau_{ij} = -\rho\overline{u_i'u_j'} = 2\mu_t S_{ij} - \frac{2}{3}\rho k\delta_{ij} \tag{9.43}$$

| $C_{\varepsilon 1}$ | $C_{\varepsilon 2}$ | $\sigma_k$ | $\sigma_\varepsilon$ | $C_\mu$ |
|---|---|---|---|---|
| 1.44 | 1.92 | 1.0 | 1.3 | 0.09 |

**Table 8: Coefficients of standard $k$-$\varepsilon$ model.**

The $k$-$\varepsilon$ model provides a 'middle of the road' calibration which covers many flows with sensible accuracy – which might explain its popularity over the years.

A well-published deficiency of the $\varepsilon$-equation is the lack of response to adverse pressure gradient flows [7], [17]. The model produces too large turbulence length scales near the wall and thereby delays or even suppresses flow separation when compared with experimental data. This in turn leads to overly optimistic design choices as the model predicts attached flow under conditions, where the real flow can already be severely separated.

This effect can be seen for a diffuser flow [54]. It consists of a straight wall on one side and an inclined wall on the other. The flow in the experiment separates from the inclined wall. Figure 101 shows the different flow topologies predicted by the SST and the $k$-$\varepsilon$ model. Figure 102 provides a comparison of the model predictions with the experimental velocity profiles which clearly shows that the flow is separated as predicted by the SST model. In case where the design engineer would base the decision of the opening angle of the diffuser on the $k$-$\varepsilon$ model, the real performance (pressure loss) would be much more optimistic than later observed when the device is built.
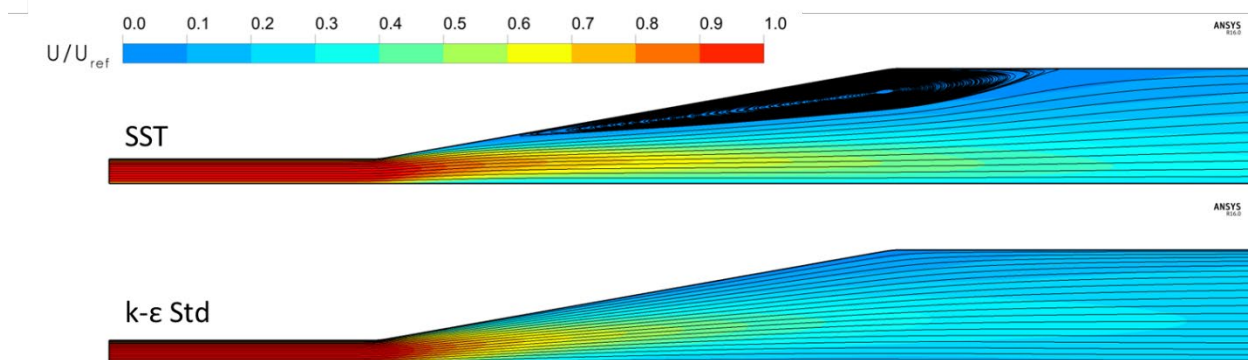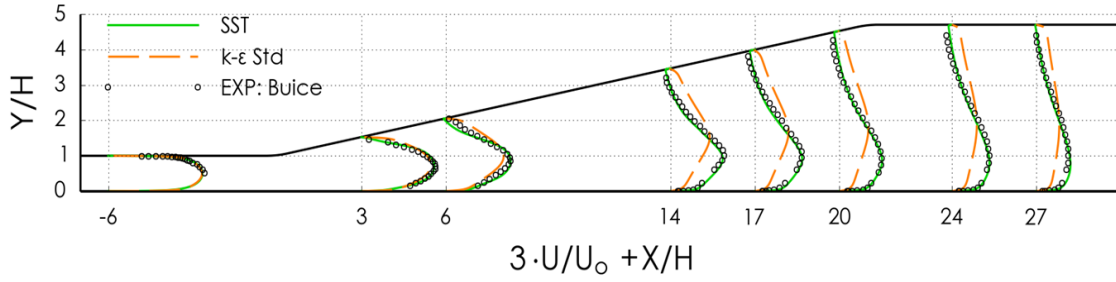
**Figure 102: Velocity profiles for Obi diffuser [54]. Comparison of SST, k-ε and experimental data.**

It is important to emphasize that similar pictures of failure could be produced for almost any turbulence model, as there are always flows where models struggle. However, the ability to accurately predict separation onset is essential for many applications, and the $k$-$\varepsilon$ based models have never been able to overcome their deficiencies in this respect.

*The Realizable k-ε Model (RKE)*

The RKE model is a variation of the standard $k$-$\varepsilon$ model. Its derivation is somewhat curious, involving a mix of small and large scale arguments [15], but this is of no relevance in the current document. The equations read:

$$\frac{\partial(\rho k)}{\partial t} + \frac{\partial(\rho U_j k)}{\partial x_j} = P_k - \rho\varepsilon + \frac{\partial}{\partial x_j}\left[\left(\mu + \frac{\mu_t}{\sigma_k}\right)\frac{\partial k}{\partial x_j}\right] \tag{9.44}$$

$$\frac{\partial(\rho\varepsilon)}{\partial t} + \frac{\partial(\rho U_j \varepsilon)}{\partial x_j} = C_1 \varepsilon S - C_{\varepsilon 2}\rho \frac{\varepsilon}{k + \sqrt{\nu\varepsilon}}\varepsilon + \frac{\partial}{\partial x_j}\left[\left(\mu + \frac{\mu_t}{\sigma_\varepsilon}\right)\frac{\partial\varepsilon}{\partial x_j}\right] \tag{9.45}$$

$$\mu_t = C_\mu\rho\frac{k^2}{\varepsilon}, \qquad P_k = \tau_{ij}\frac{\partial U_i}{\partial x_j}, \quad \tau_{ij} = -\rho\overline{u_i' u_j'} = 2\mu_t S_{ij} - \frac{2}{3}\rho k\delta_{ij} \tag{9.46}$$

$$C_1 = max\left[0.43, \frac{\eta}{\eta + 5}\right], \quad \eta = S\frac{k}{\varepsilon}, \quad S = \sqrt{2S_{ij}S_{ij}}$$

$$C_\mu = \frac{1}{A_0 + A_S\dfrac{kU^*}{\varepsilon}}, \quad U^* = \sqrt{S_{ij}S_{ij} + \Omega_{ij}\Omega_{ij}} \tag{9.47}$$

$$A_0 = 4.04, \quad A_S = \sqrt{6}cos(\varphi)$$

$$\varphi = acos(\sqrt{6}W), \quad W = \frac{S_{ij}S_{jk}S_{ki}}{\tilde{S}^3}, \quad \tilde{S} = \sqrt{S_{ij}S_{ij}} \tag{9.48}$$

| $C_{\varepsilon 2}$ | $\sigma_k$ | $\sigma_\varepsilon$ |
|---|---|---|
| 1.9 | 1.0 | 1.2 |

**Table 9: Coefficients RKE $k$-$\varepsilon$ model**

### 9.2.3. Limiters

One of the lesser appreciated deficiencies of two-equation models is their behavior in inviscid regions with non-zero strain rates. In such regions the vorticity is zero, but the strain-rate is not. A typical example is the stagnation region of an airfoil (outside the boundary layer). As the inviscid

flow approaches the airfoil, there is an increasing level of shear, $S = \sqrt{2S_{ij}S_{ij}}$, but not due to a shear layer, but due to non-zero velocity gradients of the inviscid flow. Similar regions exist when inviscid flow is accelerated. Observations show that two-equation models can exhibit excessively high levels of eddy-viscosity there (Section 4.7). From a physical standpoint, there is very little turbulence production in such areas, so that this is likely an artefact of the eddy-viscosity formulation. The introduction of the eddy-viscosity assumption into the production term of the turbulence kinetic energy equation changes the characteristics of that term. While in the exact $k$-equation it is a product of turbulent stresses times a velocity gradient (see Equation (9.9)) (and therefore linear in terms of the velocity gradients), it becomes a product of the eddy-viscosity times the strain rate square (and therefore quadratic in the velocity gradients). It is believed that this difference is responsible for the observation of high turbulence production.

To avoid such unphysical behavior, different types of limiters have been developed. Each has their pros and cons, but all are better than running the model without limiters.

*Kato-Launder Limiter*

The Kato-Launder limiter [21] is based on the observation that in the inviscid region, the vorticity is zero, whereas in plane shear layers it is equal to the shear strain rate:

$$\begin{aligned} \Omega &= 0 & \text{in inviscid flows} \\ \Omega &= S & \text{in shear flows} \end{aligned} \tag{9.49}$$

With

$$S_{ij} = \frac{1}{2}\left(\frac{\partial \bar{U}_i}{\partial x_j} + \frac{\partial \bar{U}_j}{\partial x_i}\right), \quad W_{ij} = \frac{1}{2}\left(\frac{\partial \bar{U}_i}{\partial x_j} - \frac{\partial \bar{U}_j}{\partial x_i}\right) \tag{9.50}$$

$$S = \sqrt{2S_{ij}S_{ij}}, \quad \Omega = \sqrt{2W_{ij}W_{ij}} \tag{9.51}$$

The Kato-Launder limiter is formulated as a change to the (incompressible portion of the) production term $P_k$:

$$P_k = \mu_t S^2 \quad \rightarrow \quad P_k^{KL} = \mu_t S\Omega \tag{9.52}$$

Since most model calibrations are carried out for shear flows with $S = \Omega$, this does not change the model calibration for such flows. On the other hand, the modification turns off the production term in inviscid flows where $\Omega = 0$. The downside of the Kato-Launder limiter is that it does affect non-trivial flows with 3D effects and/or streamline curvature and rotation where $S \neq \Omega$.

*Production Limiter*

A limiter with much less impact on complex flows was proposed in [17]. The limiter is applied to the production term in relation to the dissipation.

$$P_k = \mu_t S^2 \quad \rightarrow \quad P_k^{PL} = min(P_k, C_{PL}\rho\varepsilon) \tag{9.53}$$

Typically, the limiter is set to a value of $C_{PL} = 10$, which is far away from typical calibration flows for which one has $P_k \approx \rho\varepsilon$.

The realizability limiter is based on the demand that the Reynolds stresses computed from the eddy-viscosity model should adhere to known restrictions to the Reynolds Stresses [2] (e.g. non-negativity etc.). It reads:

$$\mu_t^{Real} = \mu_t \frac{1}{max(1, S/(C_{Real}\omega))} \tag{9.54}$$

with $C_{Real} = 1/\sqrt{3}$. This limiter is like the production limiter but corresponds more closely to a $C_{PL} \approx 4$. It is therefore activated sooner than the production limiter.

*Realizability Limiter of RKE Model*

The realizability limiter of the RKE (Equation (9.47)) model is quite different from the classical realizability limiter. It depends not only on the strain rate but also on the vorticity and the third invariant of the strain rate tensor. Since $A_S$ can become negative, it is not even ensured that the eddy-viscosity is limited. In addition, the production term in the $k$-equation is formulated as a conventional quadratic term in strain rate ($S^2$), whereas the production in the $\varepsilon$-equation is formulated as a linear term in $S$. This all makes it very difficult to judge the activation limit of this limiter and therefore its effectiveness.

## 9.3. Near-Wall Treatment

The wall treatment in a CFD method is necessary to allow the prediction of the wall shear-stress, required in the wall cells in the momentum equations as a wall-force. The wall shear-stress is computed from the known solution for the velocity $\bar{U}$ (and possibly $k$ and other quantities) at point j=1 (known e.g., from the previous iteration). This is depicted in Figure 103 for a cell-centered finite volume method. The task is therefore, given $\bar{U}$ at j=1, compute the wall shear-stress to close the discretization of the momentum equations.
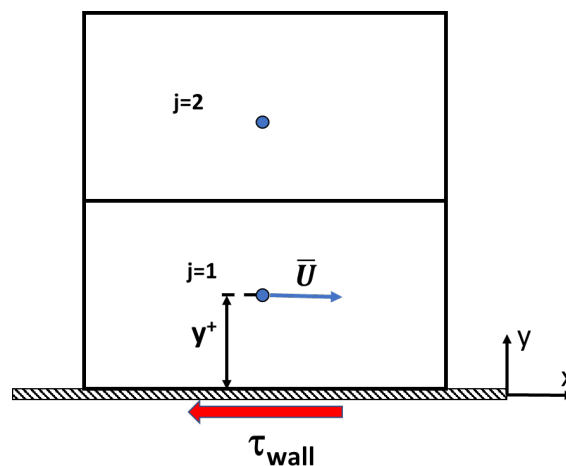


**Figure 103: Near wall grid cells for a finite volume cell-centered method.**

Near the wall of equilibrium flows (zero pressure gradient boundary layer, channel flow, pipe flow, Couette flow), the solution variables follow universal laws which scale with the wall-shear stress $\tau_{wall}$ and the near wall molecular kinematic viscosity, $\nu$. In other words, one can collapse all equilibrium near wall profiles onto a single curve if the near wall variables are non-dimensionalized by these quantities. The non-dimensionalization is based on the wall-friction velocity $u_\tau$ (computed from $u_\tau = \sqrt{\tau_{wall}/\rho}$), the turbulence kinetic energy $u^* = C_\mu^{0.25}\sqrt{k}$ (note that in the logarithmic layer one has $u_\tau = u^*$) and the kinematic viscosity $\nu$ in the following way:

$$U^+ = \frac{\overline{U}}{u_\tau}, \quad y^+ = \frac{u_\tau y}{\nu}, \quad y^* = \frac{u^* y}{\nu}, \quad k^+ = \frac{k}{u_\tau^2}, \quad \omega^+ = \frac{\omega \nu}{u_\tau^2}, \quad \varepsilon = \frac{\varepsilon \nu}{u_\tau^4} \qquad (9.55)$$

Using these variables, one obtains a universal velocity profile of the form:

$$U^+ = F(y^+) \quad or \quad U^+ = F(y^*) \qquad (9.56)$$

Such profiles are depicted in Figure 104 for two Reynolds number of a boundary layer. For both Reynolds numbers, the profiles are identical near the wall and differ in the outer part. The extent to which the universal profile is followed depends on the Reynolds number.

Assuming a universal velocity profile does exist, what is the benefit for CFD? Suppose the velocity is known in the near wall cell (j=1) e.g., from the last iteration. Since the location of the first cell center is also known and so are the viscosity and density, they can all be inserted into Equation (9.56). The only unknown is then the friction velocity $u_\tau$, which can therefore be calculated (iteratively due to the non-linearity of the equation). From $u_\tau$ follows the wall-shear-stress $\tau_{wall} = \rho u_\tau u_\tau$, which is required to close the discretization of the near wall cell. Once this is achieved, a new global iteration can be started until convergence. The details are slightly different for each model (involving e.g., $u^*$) and can be found in the user documentation. However, the principle is as outlined here.

The universal profile consists of different parts. Very close to the wall, turbulence is damped, and the velocity profile is linear (viscous sublayer). In the fully-turbulent near wall layer, the profile follows a logarithmic form (log-law). These two regions are bridged by a 'buffer layer'. This is illustrated in Figure 104 which depicts two flat plate boundary layer profiles (at different Reynolds numbers) in a logarithmic plot. The velocity profile can roughly be split as follows

| | | |
|---|---|---|
| **Linear** | $0 < y^+ < 5$ | $U^+ = y^+$ |
| **Buffer** | $5 \le y^+ \le 20$ | |
| **Logarithmic** | $20 < y^+ < \cdots$ | $U^+ = \frac{1}{\kappa} ln(y^+) + C$ |

The log-profile has two constants - the von Karman constant which is typically selected to be $\kappa = 0.41$ and an additive constant of approximately $C = 5.2$.
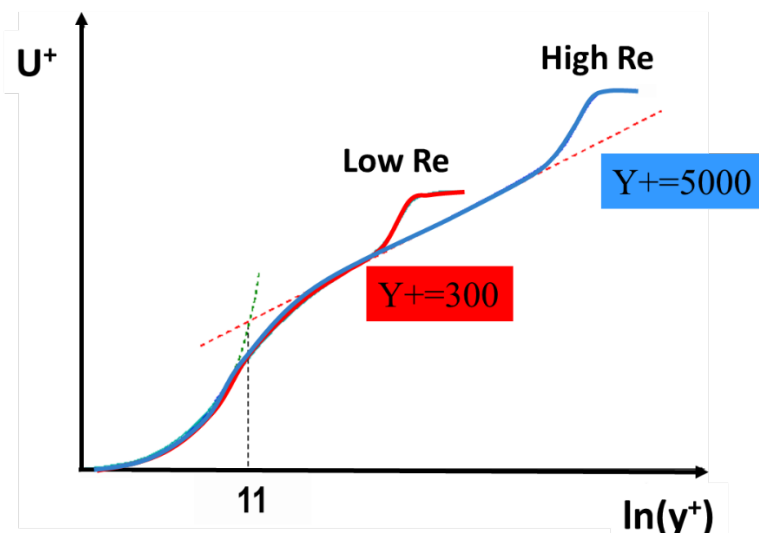


**Figure 104: Universal non-dimensional velocity- profile near the wall.**

Important: while the velocity profile follows a universal law near the wall, the thickness of the log-layer in terms of $y^+$ depends on the Reynolds number. A $y^+$ resolution of say $y^+ = 50$ will therefore be sufficient for a high Reynolds number flow, but not for a Low Reynolds number flow. In the high Re case, there are plenty of cells between the wall cell and the boundary layer edge (which is say at $\delta^+ = 5000$), compared with a low-Re case where the boundary layer edge might be at say $\delta^+ = 200$.

**Important: Even for high Re number flows, the inner layers (sub+ buffer+ log-law) cover only 10-20% of the entire boundary layer thickness.**

### 9.3.1. Standard Wall Functions

Historically, many turbulence models have been combined with a 'wall-function' (WF) approach. WF do not allow/require to integrate the equations through the viscous sublayer. Instead, the user needs to provide a grid, where the first grid point (cell center) lies in the log-layer. The wall shear stress is then computed from the log-layer formulation alone. Details of specific WF formulations can be more elaborate and can be found in the code documentation.

Wall function treatment has the advantage that simulations can be carried out on relatively coarse grids (in wall normal direction). However, the user must ensure that the first cell center lies in the log-layer. As depicted in Figure 104, this is not trivial, as the upper limit of the log-layer depends on the Reynolds number of the boundary layer profile. One can therefore not define a universal upper limit, as to where the log layer is applicable. Especially for low to moderate Reynolds number (device Re numbers of $10^4$-$10^6$) the thickness of the log-layer might be narrow, and the first grid point can easily be placed either too close or too far from the wall, missing the layer. In addition, at the lower Reynolds numbers, even if the first cell center is placed in the log-layer, there might be not enough resolution to cover the rest of the boundary layer with enough cells.

Standard wall functions are highly problematic, as the solution depends on the ability of the user to:

- Ensure that the cell center point is not too close to the wall so as not to fall into the buffer/sublayer.
- Ensure that the cell center point is not too far from the wall to not fall into the outer layer.
- Ensure that the boundary layer is resolved with enough cells.

The violation of any of these conditions can result in substantial errors. Most problematic is that mesh refinement beyond a certain level leads to a deterioration of results. This is counter to the principles of numerical methods, where grid refinement should eventually lead to more consistent and grid-converged solutions. The above requirements are hard to achieve, especially at low-moderate Reynolds numbers. One needs also not to forget that the mesh is created before a solution is available, so placing the first grid cell into the log-layer is a difficult job. The use of standard wall functions is therefore discouraged – it is not available when using k-ω based models for that reason.

Users are often under the false impression that wall functions 'take care of the boundary layer' – meaning that a grid with a properly placed $y^+$ near wall cell is all that is needed for an accurate boundary layer simulation. This is not the case. Wall functions are just a special type of boundary conditions – the boundary layer itself still needs to be resolved with a sufficient number of cells.

**Important: With standard wall functions, one can easily create incorrect solutions, either by overly coarse or overly fine meshes. The usage of standard wall functions is therefore not recommended.**

**Important: having a proper $y^+$ is not sufficient for accurate boundary layer simulations. One also needs a sufficient number of cells inside the boundary layer.**

### 9.3.2. Scalable Wall Functions

A simple trick can be employed to avoid the solution deterioration under mesh refinement with standard wall functions, by applying a limiter onto $y^+$ [55]:

$$\tilde{y}^+ = max(y^+, 11) \tag{9.57}$$

This limiter prevents the wall functions to move into the viscous sublayer and thereby guarantees a consistent wall shear-stress (and wall heat-transfer) even under mesh refinement. While the scalable wall function is a substantial improvement, it still entails significant assumptions, as the mesh is no longer refined towards the wall, but towards a fictitious location at $y^+ = 11$, thereby slightly altering the geometry. This change is more noticeable at low Reynolds numbers as the gap between $y^+ = 0$ and $y^+ = 11$ becomes a larger portion of the overall geometry (e.g. the height of the channel or boundary layer) than for high Reynolds numbers.

### 9.3.3. Viscous Sublayer Model (VSM)

A more consistent, albeit more expensive method is to integrate the equations all the way to the wall. This requires a near-wall grid with a resolution of $y^+ \sim 1$ or finer. However, such an integration can only be performed if the turbulence models is calibrated to represent the sublayer. Since turbulence is damped by viscosity in the buffer- and sublayer, most turbulence models require additional damping terms and/or specific boundary conditions to account for this effect.

Historically models which can be integrated to the wall have been termed 'Low-Reynolds number' models or 'low-Re' models. This is a highly confusing nomenclature, as the term 'low-Re' refers not to the device Reynolds number, but to the turbulent Reynolds number $Re_t = \sqrt{k}y/\nu$ where $k$ is the turbulence kinetic energy, $y$ is the wall distance and $\nu$ is the kinematic viscosity. As $k$ is damped by the presence of the wall, the turbulence kinetic energy $k$ approaches zero for low $y^+$ levels and so does the turbulent Re number. This is the case for all flows close to the wall, at all device Reynolds numbers! In the following, the term 'low-Re model' will therefore be replaced by the terminology 'Viscous Sublayer Model – VSM'.

Developing VSMs for $\varepsilon$-equation based models has been a major challenge. Many such models have been developed over time (e.g. [56]), but they typically suffer from one or more of the following deficiencies:

- Lack of robustness.
- Multiple solutions depending on initial conditions.
- Pseudo-transitional behavior not calibrated against data.
- Excessive wall shear and heat transfer at reattachment/stagnation points/lines.

There are some remedies to this. The first and most widely applied is the usage of a so-called 2-Layer formulation ([57], [58]). In this method, the epsilon equation is not solved through the buffer and sublayer but an algebraic formulation is used instead. The $\varepsilon$-equation is then dominated by a source term which enforces the algebraic relations.

A second approach is to add additional differential equations to the $\varepsilon$-equations based models which account for the near wall damping. These models are typically called 'elliptic-blending' or V2F models [59]. The downside of this approach is the significantly increased complexity due to two additional equations and the associated complex boundary conditions. In addition, such models still allow for pseudo-transitional behavior, meaning an artificially non-calibrated laminar-turbulent transition process, which is undesirable. For these reasons V2F-like models are not perused in Ansys CFD.

One of the strengths of the $\omega$-equation based models is that they do not require additional damping terms. Integration to the wall can be obtained by a simple switch in boundary conditions. These models also avoid pseudo-transition for all practical purposes and do not lead to excessive

wall shear and heat transfer at reattachment/stagnation points/lines. For this reason, $\omega$-equation based models are the preferred option in Ansys CFD.

> **Important: $\varepsilon$-equation based models are much harder to integrate to the wall than $\omega$-based models.**

### 9.3.4. Y$^+$-Insensitive Wall Treatments

Classical VSM require always a fine near wall mesh with $y^+ \sim 1$ or smaller. This cannot be achieved for all walls in complex applications. It is therefore desirable to be able to provide formulations which maintain consistency for a variation in $y^+$. Such models are termed $y^+$-insensitive models (or all-$y^+$ models). When computing a flow on a series of grids with different $y^+$-resolution, such models provide wall shear-stress (and heat transfer) levels which are approximately independent of the $y^+$-value. Note that this statement is only correct in case of a sufficient number of cells inside the boundary layer. Simulations with such a formulation can be seen in Figure 105, where a flat plate zero pressure gradient boundary layer [29] is computed on three different grids. The computed velocity profiles follow closely the fine grid solution. On meshes with $y^+ > 20$, the formulation essentially switches back to a wall function.
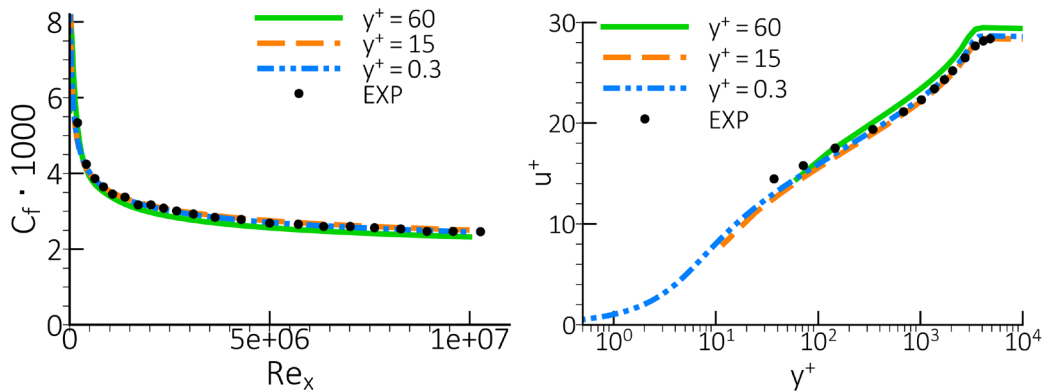


**Figure 105. Comparison of the skin friction coefficient and velocity profiles at Re$_x$ = 8.7·10$^6$ on different meshes for the flat plate boundary layer [29].**

In Ansys Fluent®, $y^+$-insensitive wall formulations are available for the Spalart-Allmaras one-equation model and $k$-$\varepsilon$ models (using a 2-Layer VSM formulation and the ML VSM). In both codes (Ansys Fluent® and Ansys CFX®) all $\omega$-equations based models are based on a $y^+$-insensitive formulation. The details of such formulations are model and numerics dependent and are given in more detail in the Theory Documentation of the corresponding codes.

*Y+-Insensitive Near Wall Treatment for $\omega$-based Models*

Near the wall, the $\omega$-equation reduces to (in the viscous sublayer production and turbulent diffusion can also be neglected):

$$0 = C_{\omega 1} S^2 - C_{\omega 2} \rho \omega^2 + \frac{\partial}{\partial x_j}\left(\left(\mu + \frac{\mu_t}{\sigma_\omega}\right)\frac{\partial \omega}{\partial x_j}\right) \tag{9.58}$$

This equation has the following near-wall solutions for $\omega$ in the viscous sub-layer and the log-layer:

$$\omega_{NW} = \frac{1}{\left(\sqrt{\frac{C_{\omega 2}}{6\nu} y^2} + \sqrt{\frac{1}{\omega_0}}\right)^2} \tag{9.59}$$

$$\omega_{Log} = \frac{1}{\sqrt{C_\mu}} \frac{u_\tau}{\kappa y} \tag{9.60}$$

where $\omega_0$ is the (typically high) value specified for $\omega$ at the wall. This formulation is sufficient to provide proper near wall damping and the correct logarithmic layer. The $\omega$-equations y$^+$-insensitive formulation blends smoothly between these two solutions.

The simple and robust near wall formulation without the need for complex damping functions (or new additional transport equations like in the V2F model) makes the $k$-$\omega$ model the most attractive option as a basis for industrial turbulence models.

### *The k-ε Two-Layer Formulation*

To avoid the complication and robustness limitations of historic VSM (low-Re) $k$-$\varepsilon$ models, but still enable CFD users to integrate these models through the viscous sublayer, the so-called 'two-layer' (2L) formulation was introduced [57], [58]. The 2L formulation is today one of the more widely used turbulence near-wall formulations in industrial codes for the $k$-$\varepsilon$ model. Its principal idea is to avoid the complexities of the $\varepsilon$-equation near the wall entirely and to replace it with an algebraic formulation, using a mixing-length model there. This algebraic formulation is then blended with the $\varepsilon$-equation away from the wall.

In the 2L model the near-wall $\varepsilon$-distribution is computed from an algebraic equation:

$$\varepsilon = \frac{k^{1.5}}{l_\varepsilon} \tag{9.61}$$

where $l_\varepsilon$ is the mixing-length based on wall-distance, y:

$$l_\varepsilon = y C_l^* \left(1 - e^{-Re_y/A_\varepsilon}\right) \quad with \quad Re_y = \frac{y\sqrt{k}}{\nu} \tag{9.62}$$

In addition, the eddy-viscosity is also blended between the standard $k$-$\varepsilon$ formulation and an algebraic mixing length model:

$$\mu_{t,EWT} = \lambda_\varepsilon \mu_t + (1 - \lambda_\varepsilon)\mu_{t,2Layer}$$
$$\mu_{t,2Layer} = \rho C_\mu l_\mu \sqrt{k} \tag{9.63}$$
$$l_\mu = y C_l^* \left(1 - e^{-Re_y/A_\mu}\right)$$

Using the blending function:

$$F_{2Layer} = \lambda_\varepsilon = \frac{1}{2}\left[1 + \tanh\left(\frac{Re_y - Re_y^*}{A}\right)\right], \quad Re_y^* = 200$$
$$A = \frac{\Delta Re_y}{\text{atanh}(0.98)} \qquad \Delta Re_y = 0.1 \cdot Re_y^* \tag{9.64}$$

The blending is required as the distributions resulting from the algebraic formulation and from the transport equation will not match at a pre-specified $Re_y$ location. To prevent discontinuities and convergence problems, a smooth variation is required.

The constants are:

$$C_l^* = \kappa C_\mu^{-3/4}, \quad A_\mu = 70, \quad A_\varepsilon = 2C_l^* \tag{9.65}$$

The turbulent Reynolds number $Re_y$ is also used to blend between the algebraic model and the transport equation for $\varepsilon$. The details of these blending are typically code-dependent and are therefore not provided here. Such blending between algebraic and transport equations can lead to robustness problems and therefore needs to be performed gradually over a significant portion of the inner portion of the boundary layer ($Re_y < 200$).

The 2L-blending can cause problems in low-Re number flows, where the model can be dominated by the algebraic formulation. There is also a considerable Reynolds-number effect for non-equilibrium flows, where the 2L mixing length model part and the $\varepsilon$-equation produce different results, which are then stitched together with the blending function. The relative portion across the boundary layer where the mixing length model is active depends on the $Re$ number of the boundary layer. For low $Re$, a substantial part of the boundary layer will be covered by the algebraic part of the model, whereas for high $Re$, the 2L model is active only in a small near-wall portion (relative to the boundary layer thickness). As both models behave differently for non-equilibrium flows, this mean that the combined model will lean towards a mixing length model for low $Re_\theta$ and towards a $k$-$\varepsilon$ model for high $Re_\theta$.

Another problematic issue results from the observation that the blending function based on $Re_y = \sqrt{k}y/n$ can switch back to 'near-wall mode' even outside the boundary layer in case of low freestream values for $k$, causing non-physical distributions of the turbulence variables outside the boundary layer. By this mechanism, a layer of high turbulence viscosity can be created artificially, as the eddy-viscosity is also switched to the mixing length formulation (with obviously a large mixing length due to the large wall distance). Figure 106 shows a simulation around a NACA 4412 airfoil. The $Re_y$ distribution used inside the blending function is shown in part (a), of the Figure. $Re_y$ is zero at the wall, increases rapidly inside the boundary layer (hard to see in this scale), but then decreases again outside the boundary layer. The effect on the blending function is shown in the middle of Figure 106. The function is $F_{2Layer} = 0$ close to the wall (not seen on this scale) and then switches to $F_{2Layer} = 1$ inside the boundary layer as desired. However, outside the boundary layer, the formulation switches back to the algebraic form ($F_{2Layer} = 0$). This switch-back is problematic, as it also switches the eddy-viscosity back to the alg. formulation, which can be seen in the lower part of Figure 106c, where $EVR = \mu_t/\mu$ is plotted. This ratio reaches relatively high values outside the boundary layer and the switches back to the low freestream values further away, as the function switches back to $F_{2Layer} = 1$.

These examples demonstrate that the 2L model can cause issues due to its switching procedure. This is even more the case for flows with additional complexities like multi-phase flows and/or flows with large changes in physical properties, where the model has shown instabilities due to erratic switching between the mixing length and the transport equation, thereby preventing solver convergence. While the 2L formulation works well for many industrial flows, it is not strong enough to serve as a default turbulence model which needs to work for all combinations of physics.
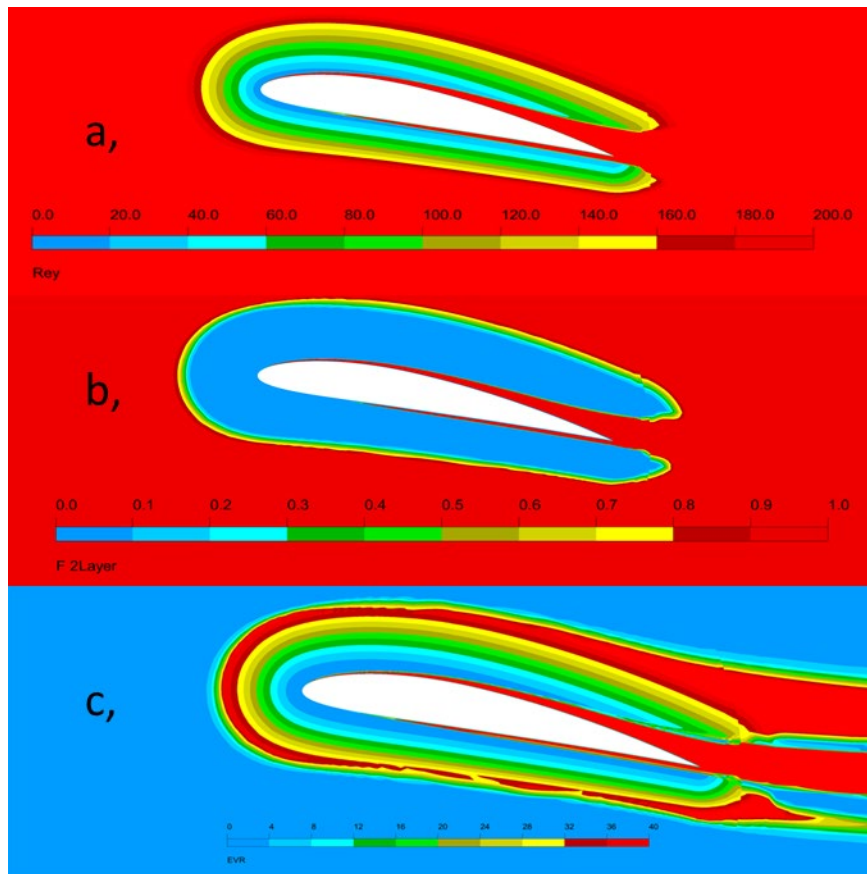
**Figure 106: Contours of the Re$_y$ (Top, a,) and the Blending Function (Middle, b,) and the ratio of eddy-viscosity/molecular viscosity $EVR = \mu_t/\mu$ (Bottom, c,) of the 2L formulation for flow around the NACA-4412 airfoil at AoA = 12º.**

## 9.4. Appendix A: Boundary Layer Parameters

In order to create a high-quality mesh, it is helpful to have some approximate formulas for the development of boundary layers for zero pressure gradient boundary layers. The Boundary Layer develops in streamwise direction ($x$-direction) for a flat plate with origin at x=0. The boundary layer thickness is $\delta$, the freestream velocity is $U$ and the wall shear stress is $\tau_{wall}$. The wall friction coefficient is $C_f = \tau_{wall}/(0.5\rho U^2)$ and $Re_x = \rho Ux/\mu$

### 9.4.1. Laminar Flow:

Wall shear stress:

$$C_f = 0.664 Re_x^{-1/2} \tag{9.66}$$

Boundary Layer thickness:

$$\frac{\delta}{x} = 5.0 Re_x^{-1/2} \tag{9.67}$$

### 9.4.2. Turbulent Flow:

Wall shear stress coefficient:

$$C_f = 0.058 Re_x^{-1/5} \tag{9.68}$$

Boundary Layer thickness:

$$\frac{\delta}{x} = 0.37 Re_x^{-1/5} \tag{9.69}$$

Viscous sublayer thickness – $\Delta y^+$-estimate:

$$\Delta y^+ = \frac{u_\tau \Delta y}{\nu} \quad \rightarrow \quad \Delta y = \frac{\Delta y^+ \nu}{u_\tau} \tag{9.70}$$

$$u_\tau = \sqrt{\frac{\tau_{wall}}{\rho}} = U\sqrt{0.5 C_f} = U\sqrt{0.5 \cdot 0.058 \cdot Re_x^{-1/5}} = 0.17 \cdot U \cdot Re_x^{-1/10} \tag{9.71}$$

$$\Delta y = \frac{\Delta y^+ \nu}{0.17 \cdot U \cdot Re_x^{-1/10}} = 5.8 \cdot \Delta y^+ \frac{\nu}{U} Re_x^{1/10} \tag{9.72}$$

This formula provides the required wall spacing $\Delta y$ to achieve a desired $\Delta y^+$. For $Re_x$ it is prudent to use half the running length of the boundary layer (e.g. half chord of an airfoil). The good news from this equation is that $\Delta y^+$ has only a very weak variation with $Re_x$. It is therefore possible to use a constant near wall grid spacing $\Delta y$ for the entire body. Note that the above $\Delta y^+$ estimate is based on the grid distance between the surface and the first grid node off the wall. The code can internally use another $y^+$ definition – e.g. in a cell-centered code like Ansys Fluent® it would use half of that value.